COMPUTATIONAL MODELING OF FLOW DIVERTING DEVICES IN INTRACRANIAL ANEURYSMS

by

Marcelo A. Raschi

A Dissertation
Submitted to the
Graduate Faculty
of
George Mason University
in Partial Fulfillment of
The Requirements for the Degree
of
Doctor of Philosophy
Computational Sciences and Informatics

Committee:

_____	Dr. Juan R. Cebral, Dissertation Director
_____	Dr. Rainald Löhner, Committee Member
_____	Dr. Fernando Camelli, Committee Member
_____	Dr. Daniel M. Anderson, Committee Member
_____	Dr. Michael Summers, Director, School of Physics, Astronomy, and Computational Sciences
_____	Dr. Timothy L. Born, Associate Dean for Student and Academic Affairs, College of Science
_____	Dr. Peggy Agouris, Interim Dean, College of Science
Date: 8-13-2013	Fall Semester 2013 George Mason University Fairfax, VA

Computational Modeling of Flow Diverting Devices in Intracranial Aneurysms

A dissertation submitted in partial fulfillment of the requirements for the degree of Doctor of Philosophy at George Mason University

By

Marcelo A. Raschi
Master of Science
Universidad Favaloro, 2009
Bachelor of Science
Instituto Balseiro, 2000

Director: Dr. Juan R. Cebral, Professor
Center for Computational Fluid Dynamics
College of Science

Fall Semester 2013
George Mason University
Fairfax, VA

DEDICATION

Dedicated to Paula and Lorenzo.

ACKNOWLEDGMENTS

This work is the result of four and a half years of activity at the Center for Computational Fluid Dynamics at George Mason University under the supervision of Prof. Dr. Juan R. Cebral. To him my deepest gratitude for giving me this opportunity, for his supervision, help, and support in my changing situation during this time.

I would like to thank Dr. Rainald Löhner for the financial support throughout this years and for the help with the implementation of the porous model in FEFLO; to Dr. Fernando Mut for uncountable hours of discussion, *mates*, and invaluable help; to Dr. Fernando Camelli for always being willing to help; to Daniel, Adam and Greg for their help in this last part of the journey.

To the rest of my friends here, for making of this time an unforgettable experience in my life.

I would like to especially thank my partner Paula, for her constant support, help, and encouragement.

TABLE OF CONTENTS

LIST OF TABLES

LIST OF FIGURES

LIST OF ABBREVIATIONS

ACA anterior communicating artery

Acom anterior communicating artery

ADPKD autosomal dominant polycystic kidney disease

AFI aneurysm formation indicator

ASI angular similarity index

BA basilar artery

BF body-fitted

CFD computational fluid dynamics

CTA computed tomography angiography

CT computed tomography

DSA digital subtraction angiography

DUS Doppler ultrasound

EDS Ehlers-Danlos syndrome

EL energy loss coefficient

FD flow diverter

GMRES generalized minimal residuals

GON gradient oscillatory number

IA intracranial aneurysm

IB immersed body

ICA internal carotid artery

ICI inflow concentration index

IMI impingement index

IMM immersed method

LSA low shear stress area

MCA middle cerebral artery

MRA magnetic resonance angiography

MRI magnetic resonance imaging

MSI magnitude similarity index

NO nitrous oxide

OSI oscillatory shear index

P-S patient-specific

PAE peri-aneurysmal environment

PCA posterior cerebral artery

Pcom posterior communicating artery

PED pipeline embolization device

PICA posterior inferior cerebellar artery

PIV particle image velocimetry

PL pressure loss coefficient

PMM porous medium method

PR porous region

SAH subarachnoid hemorrhage

SCI shear concentration Index

STL stereolithographic format

UIA unruptured intracranial aneurysm

VDR viscous dissipation ratio

WSSG wall shear stress gradient

WSS wall shear stress

ABSTRACT

COMPUTATIONAL MODELING OF FLOW DIVERTING DEVICES IN INTRACRANIAL ANEURYSMS

Marcelo A. Raschi, Ph.D.

George Mason University, 2013

Dissertation Director: Dr. Juan R. Cebral

When evaluating unruptured cerebral aneurysms, it is necessary to assess their risk of rupture and to compare them to the risks involved in their treatment. Simulations using the patient-specific (P-S) geometry of the aneurysm may help in a better planning of the treatment and in a consequent reduction of the associated risks.

To have a better understanding of the rupture risks, we first review studies with the suggested hypotheses that connect the aneurysm risk factors and the mechanisms governing the aneurysm evolution. This literature review reveals a progressive wall degradation due to changing hemodynamic loading and biomechanic stress, affected by risk factors, that drives the geometrical evolution of the aneurysm until it stabilizes or ruptures. However, details of these interactions or their relative importance are still not clearly understood.

Second, to understand the influence of uncertainties involved in the P-S computational fluid dynamics (CFD) simulations, we compare the blood flow field in a growing cerebral aneurysm obtained with experimental particle image velocimetry (PIV) and CFD techniques. Despite small differences observed, mainly associated to the inherent limitations of each technique, the information derived is consistent and can be used to study the role of hemodynamics in the natural history of intracranial aneurysms.

The final objective of this work is to develop a methodology to carry on faster than current P-S simulations, allowing for their application to treatment planning and device design. We propose, validate, and implement a methodology for the simulation of flow diverter (FD) devices in intracranial aneurysms by using a porous medium method (PMM), which greatly reduces the computational cost of these simulations. The method relies on parameters from an empirical correlation derived from experimental observations in wire screens, consistent with CFD simulations. The validation of our PMM strategy was carried out by comparing the results of simulations in distinct P-S geometries and FDs, to those obtained under identical conditions by the immersed method immersed method (IMM) currently used. Overall, both quantitative and qualitative results are consistent between IMM and PMM in cases where the local porosity remains roughly uniform throughout the neck, with differences in the reduction of the observables lower than 10%. This PMM strategy is between 2 and 10 times faster than the IMM, which allows for a runtime of hours instead of days, bringing it closer for its application in the clinic.

INTRODUCTION

The management of unruptured intracranial aneurysm (UIA) remains one of the most controversial topics in neurosurgery. Because UIA are common in the population (5 % to 8 %), it is critical to assess whether their risk of rupture outweighs the risks of operative intervention. Our review article [28] suggests connections between risk factors governing prevalence and rupture of intracranial aneurysms.

One of the preferred treatments for intracranial aneurysm (IA) is by diverting the blood flow from the IA using flow diverters (FDs), which are cylindrically-shaped devices with a braided structure, that offer minimal invasivity. Currently, hemodynamic simulations for the prognosis of flow diversion in IA using computational fluid dynamics (CFD) remain circumscribed only to the academic interest because of the high computational cost and time length, which make them impracticable for their use in the clinic.

In this work, we propose, validate and implement a new approach for the simulation of FDs in aneurysms by using a porous medium method (PMM), which greatly reduces the computational cost of these simulations thus bringing these technologies closer to the clinical application.

1.1 ANEURYSM RISK ASSESMENT

UIA occur in 5 % to 8 % of the general population [94]. It has been suggested that some aneurysms bleed shortly after formation and thus are rarely detected as unruptured aneurysms, and that most aneurysms without early rupture remain stable through some healing process [98]. Most people with unruptured aneurysms remain asymptomatic and are usually unaware of their presence [132].

The event of a subarachnoid hemorrhage (SAH) from a ruptured cerebral aneurysm is a devastating condition that carries high mortality, long term disability rates and high socioeconomics costs [138]. Increased detection of UIA, which usually carry low rupture risk, has fueled a decades-long debate of whether IAs need immediate treatment or not. Many studies have focused on identifying risk factors for the formation and rupture of IAs as well as on understanding the basic mechanisms responsible for their initiation, progression and rupture.

1.1.1 *Mechanisms of formation and progression of IAs*

The underlying mechanisms governing aneurysm evolution from formation to rupture are thought to be multifactorial, involving hemodynamic loads, wall biomechanics, mechanobiology, and contacts with the peri-aneurysmal environment (PAE) [101]. It is generally accepted that the rupture of saccular aneurysm is the consequence of the inability of the wall to contain the hemodynamic loads and rupture occurs when wall stress exceeds wall strength. However, the detailed mechanisms that weaken the wall and drive the evolution of the aneurysm towards stabilization or rupture are not fully understood.

It has been argued that aneurysms are acquired degenerative lesions originated by the effect of hemodynamic stresses, since aneurysm formation can be produced experimentally by solely augmenting hemodynamic stresses for instance by increasing collateral flow after occlusion of one or more feeding vessels [112]. Presumably, the initial lesion leads to the exposure of collagen and formation of a fibrin matrix that triggers a repair process that remodels the wall of the aneurysm, modifying the geometry and creating aberrant flow conditions in the lumen. The lesion of the endothelium also initiates the development of a thin thrombus lining on the exposed collagen surface, which grows and further changes the geometry and the flow conditions. During the remodeling process, mural cells migrate to the intima and synthesize new collagen matrix while smooth muscle cells infiltrate the luminal thrombus increasing the strength of the wall and protecting

it from rupture. Under these conditions, the unruptured walls present myointimal hyperplasia and thrombus [42]. Luminal thrombosis is known to cause two separate effects leading to lesions on cell walls. First, luminal thrombosis produces high oxidative stress in the wall, accumulating cytotoxic oxidized lipids which trigger cell death. Secondly, these intracellular lipids lead to macrophage infiltration in the aneurysm producing inflammation. Inflammation and matrix degradation processes induce repair mechanisms, such as mural cells migrating to the intima and synthesizing new collagen that counteract the degradative process. In this stage the aneurysm is stable [43]. When there is a loss of mural cells, the repair mechanisms are interrupted and the aneurysm wall matrix degenerates and becomes too fragile to resist hemodynamic pressure and eventually the aneurysm ruptures [63].

1.1.2 *Proposed aneurysms risk factors*

We reviewed the literature [28] to understand the current knowledge about aneurysm risk factors and the suggested hypotheses that connect the different risk factors with the underlying mechanisms governing the aneurysm natural history. In the following subsections, we try to summarize the most relevant factors. In particular, we will consider the aneurysm location, the PAE, geometry, the vessel wall status, the patient's genetics and clinical factors, and the hemodynamics in more detail later in this section (1.1.3).

Location

Most IAs are located in the anterior circulation. The most common locations for anterior circulation aneurysms are the anterior communicating artery (Acom) followed by the posterior communicating artery (Pcom), the middle cerebral artery (MCA), and the internal carotid artery (ICA) [33]. Differences in the size distribution of ruptured aneurysms according to location have been reported [136], and has been hypothesized by other authors that the critical diameter for rupture is proportional to the average wall thickness. This

suggests that aneurysms at smaller arteries may rupture at smaller sizes since they had initially thinner walls [14]. These observations seem to indicate that rupture risk depends on the location, and that aneurysms at the Acom and Pcom are more prone to rupture than aneurysms at other locations. Several studies and observations [143, 49, 16, 17, 18, 45] seem to suggest that abnormal flow conditions and high wall shear stress (WSS) in particular, play an important role in the development and rupture of Acom aneurysms.

The case of IAs located in the posterior circulation is less frequent (10 % to 20 %) [51, 137], but has been associated with a higher risk of rupture [33, 130] than aneurysms in the anterior circulation. The most common location in the posterior circulation is the tip of the basilar artery (BA), followed by the origin of the posterior inferior cerebellar artery (PICA) [51] and the posterior cerebral artery (PCA). Aneurysms of the PICA are relatively rare, they account for approximately 18 % of all aneurysms in the posterior circulation, but aneurysms in this location have a high rupture rate of approximately 80 % [85].

It has been shown [111] that Acom, Pcom and BA tip aneurysms tend to occur more often in anatomically variant circle of Willis (figure 1).

The evidence may relate to more fragile wall disposition as it is not fully matured, or to altered hemodynamics secondary to the anatomical variation. A CFD model of the circle of Willis constructed from population averaged characteristics showed that high WSS (>300 dyne/cm^2) occurred at locations where aneurysms are frequently seen and in anatomic variations known to have increased risk of aneurysm development. Other authors [36] concluded that the circle of Willis influences the development of intracranial aneurysms, but it is not strongly correlated to rupture.

Peri-Aneurysmal Environment

Contacts between the aneurysm and extra-vascular anatomical structures of the PAE have been suggested as potential factors affecting the rupture risk of intracranial aneurysms. Computer models with idealized geometries have been used to propose that smooth contact constraints provide protective support to the aneurysm dome by decreasing the wall

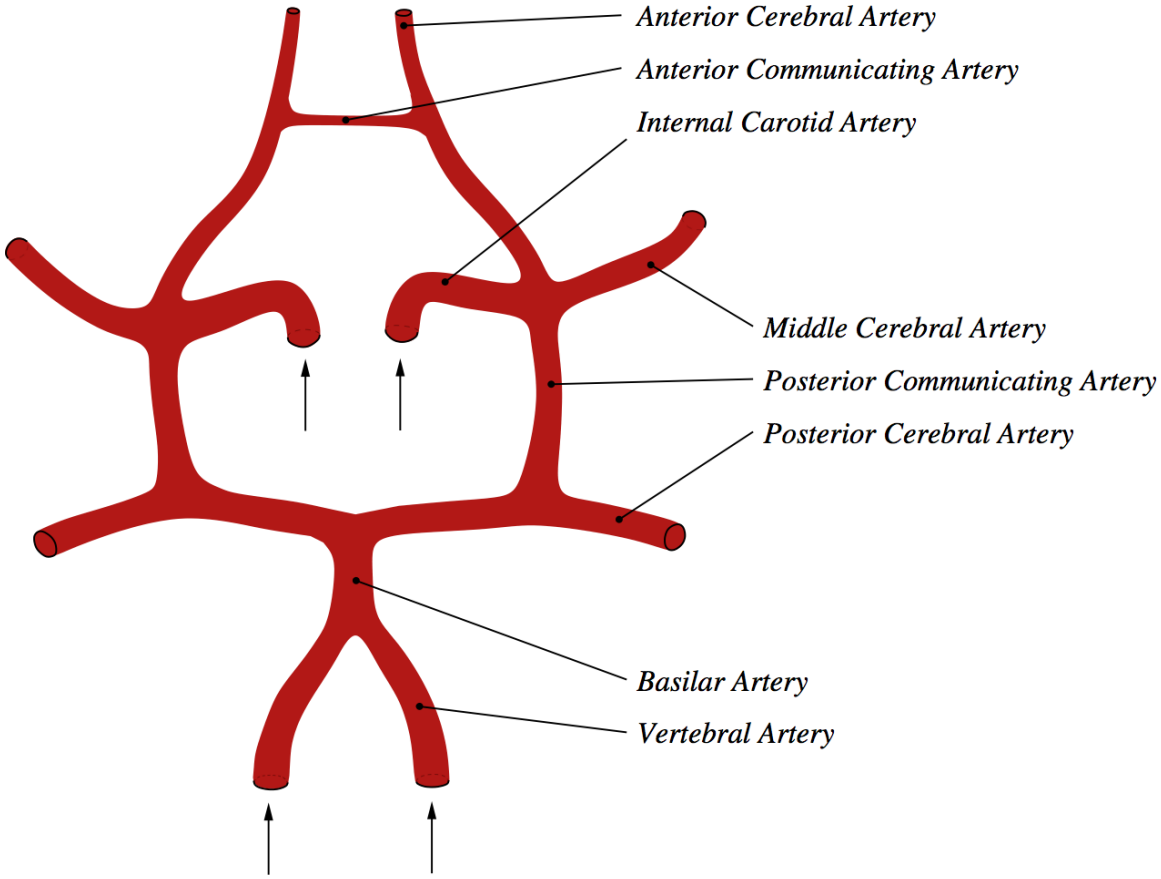

Figure 1: Simplified scheme of the circle of Willis

stresses near the fundus, while increased wall stresses can be created by sharp contacts or near the borders of contact regions where the wall can undergo sharp bends or deformations [100].

The presence of contacts between the aneurysm and surrounding structures such as bone, dura, brain cranial nerves, arteries and veins were identified in magnetic resonance imaging (MRI), computed tomography (CT), and digital subtraction angiography (DSA) images [117]. It was found that the PAE had a significant influence on aneurysmal rupture pattern, whenever the aneurysm was in direct contact with extravascular structures.

A recent case study of a growing aneurysm analyzed with image-based CFD modeling showed that in some cases contacts with structures of the PAE such as bone can significantly affect the shape and geometrical evolution of the aneurysm and can alter the hemodynamic loads as the aneurysm grows [105].

Geometry

There is no general consensus with respect to the effect of size on the risk of rupture. While studies indicate that small aneurysms (<7 mm) located in the anterior circulation are the lowest-risk natural history group [138] and giant aneurysms have a high risk of rupture [32, 89], other studies indicate that size is not the most important determinant of rupture risk [9, 83].

On the other hand, aneurysm shape has been proposed as an important factor for the assessment of aneurysm rupture risk in several studies. For example, aspect ratio [126] and shape descriptors or indices based on geometric moment invariants may be useful in predicting imminent aneurysmal ruptures [75, 129, 67, 88, 97]. Additionally, irregular multilobular appearances [8], non-spherical shapes (oval, oblong and multilobulated) [36], and deviation of the aneurysm neck [3, 82] were found to be associated with rupture. CFD studies from the group of Cebral [15] indicate that assymetric flow patterns, unsteady distribution of pressure, angle dependency with the parent artery and bifurcations can produce higher WSS, common in ruptured aneurysms.

In short, after the aneurysm has formed, complex hemodynamic flow patterns given by shape and geometry are thought to play a role in its continued growth and eventual rupture. Local pathological alterations of hemodynamic forces can injure the vascular lining inducing inflammatory responses that result in vascular smooth muscle cell apoptosis and migration and endo-thelial cell remodeling.

Vascular Wall

Loads on the aneurysm walls and hemodynamic conditions induce mechano-biological changes in the wall structure that tend to weaken and degenerate the wall thus provoking aneurysmal progression towards rupture. The shape of the aneurysm, its material properties, the loading, and its size, are important factors that affect the distribution of stresses and strains within the wall [66].

Determining unambiguously the site of rupture of cerebral aneurysms is challenging. Studies based on anatomical and histological observations reported that most of ruptures involve the dome, followed by the middle part of the aneurysm, and less frequently the neck [80, 135]. From *in-vitro* studies and fluid-structure interaction models using patient-specific (P-S)ific geometries, it is also believed that aneurysms usually rupture at the fundus of the aneurysm [53, 54].

There are contradictory reports in whether the point of aneurysmal rupture is the thinnest part of the aneurysm wall [45]. Another study indicated that the dome of unruptured aneurysms is highly heterogeneous with areas of variable thickness that appear to be related to the process of aneurysm development [60]. It was argued that these inconstant properties affect wall tensile stress and may play a role in aneurysm pathogenesis and focal rupture.

Interestingly, it was also observed that small aneurysms have a larger portion of thin wall than larger aneurysms.

Genetics

Some hereditary disorders that cause vascular abnormalities, such as autosomal dominant polycystic kidney disease (ADPKD) or Ehlers-Danlos syndrome (EDS) Type IV, have been associated with IA or aneurysmal SAH. Aneurysm prevalence in ADPKD has been estimated at approximately 5 times that in the general population[81], but not specially higher risks of growth and rupture [6, 81].

The risk of prevalence or rupture of intracranial aneurysms of patients with a history of one or more other family members suffering from SAH have been shown to depend on the number of affected relatives, increasing for one and particularly two or more relatives in comparison to the risk of sporadic cases [142]. It has been suggested that familial aggregation may relate to genetic factors that determine defects of the arterial wall and interact with shared environmental factors that predispose to a relative weakness of the arterial wall [141]. However, no clear links to genetic determinants for aneurysms have been reported in the literature[72], and the reported associations seem weaker in comparison to other factors. Moreover, based on a large population study of Nordic twins with a follow-up of 6 million person-years, heritability did not seem to be a determining factor for rupture. High incidence of SAH in a familial group has been most likely attributed to shared environmental risk factors (e.g., hypertension and smoking) rather than to a genetic origin [65].

Clinical Factors

Female gender, smoker and ADPKD are the major identified clinical risks factors for intracranial aneurysm formation. In particular, smoking has been shown to increase both, the formation of new aneurysms and the growth rate of preexisting ones [20] Smoking is known to cause inflammation in the arterial walls, which in turns weakens and predisposes the wall for aneurysm formation. Most of the factors related to prevalence of aneurysms seem to relate or affect either the artery wall or the hemodynamic loads [128].

It has been suggested that the increased female prevalence of cerebral aneurysms and SAH peaks in post-menopausal period, when there is a fall in estrogen levels. Changes in estrogen levels may have ramifications on vascular integrity, as it promotes the normal function of vascular wall [57]. It has also been suggested that anatomical and physiological factors such as differences in vessel size and blood flow velocity result in higher hemodynamic forces acting on the vessel wall in females, increasing the risk of prevalence and rupture [69].

1.1.3 *Role of the hemodynamics as a risk factor*

Hemodynamics has been proposed for many years as a fundamental player in the process of aneurysm formation and progression. An early review of the supporting evidence of the theory of congenital etiology of saccular aneurysms concluded that there is no evidence of a congenital, developmental, or inherited weakness of the wall; and that the most plausible explanation is that aneurysms are acquired degenerative lesions caused by hemodynamic stress [112]. The authors explained that the mural atrophy leading to aneurysm development can be produced experimentally by hemodynamics alone. Occlusion of one or more feeding vessels may enhance the possibility of aneurysm formation at arterial bifurcations subjected to augmented hemodynamic stress associated to collateral flow. Hypertension and connective tissue disorders associated with acquired loss of tensile strength of the connective tissues are not essential; they seem to be aggravating rather than causal factors. Another study explains that saccular cerebral aneurysms are induced in rats by ligation of one or both of the common carotid arteries, experimental hypertension, and beta-aminopropionitrile feeding [47]. Combination of ligation of the carotid artery and experimental hypertension induce aneurysms within a few months by increasing hemodynamic stress. Beta-aminopropionitrile makes the arterial wall fragile, increasing the incidence of aneurysmal development. They observed that aneurysms are

strongly related to increased hemodynamic stress, are located on the large arteries at the base of the brain, and some originate from the apex of bifurcations.

Later, a study using 2D CFD simulations of idealized aneurysm models in curved and bifurcating arteries showed increased WSS, pressure and impulse at the apex of bifurcations and outer wall of curved vessels [41]. The authors concluded that in the absence of any underlying disease process aneurysm development is a mechanically mediated event. Another study explains that congenital aneurysms, which are mainly observed at branching sites in the circle of Willis, are developed as a consequence of mechanically-induced degeneration of the wall internal elastic lamina with a genetic predisposition in the form of a wall structure deficiency in frequent familial context [10]. In this same study, high pressure zones were observed in CFD models, especially of terminal aneurysms; and the authors suggest that the greater the pressure, the greater the risk of aneurysm rupture. But, they also raise the question of whether the sites of high wall tension susceptible to rupture coincide with regions of high pressure.

More recently, it has been shown that a combination of high WSS (>1220 $\mathrm{dyne/cm^2}$) and positive wall shear stress gradient (WSSG) (> 5300 $\mathrm{dyne/cm^2/mm}$) produced by bilateral common carotid artery ligation induce aneurysm formation at the terminus of the basilar artery in rabbit models [74]. Subsequently, it has been suggested that some risk factors such as smoking, alcohol and cocaine consumption, are thought to induce aneurysm formation via mechanisms that increase blood pressure and hemodynamic stresses [86]. After the aneurysm has formed, complex hemodynamic flow patterns are thought to play a role in its continued growth and eventual rupture. Local pathological alterations of hemodynamic forces can injure the vascular lining inducing inflammatory responses that result in vascular smooth muscle cell apoptosis and migration and endothelial cell remodeling.

Several CFD based studies have proposed different indices as markers of regions prone to aneurysm formation such as the aneurysm formation indicator (AFI) [72] or the gradient

oscillatory number (GON) [106]. However, it is still not clear if these variables can reliably identify local hemodynamic conditions that lead to aneurysm initiation [103].

Since associations between aneurysm rupture and irregular shapes and in particular the presence of blebs or secondary lobulations have been reported, several studies have investigated possible relationships between local hemodynamics and the formation of blebs in IA. An *in-vitro* laser Doppler velocimeter study in two realistic models of an MCA and a BA tip aneurysm showed non-uniform WSS distribution in the aneurysm walls and regions exposed to relatively high WSS. Blebs of both aneurysms were exposed to high WSS, and unlike previous idealized studies, the inflow zone was not exposed to high WSS [121]. Similarly, high resolution phase contrast magnetic resonance in two realistic *in-vitro* models of BA and MCA bifurcation aneurysms revealed that a bleb region in the BA tip and a dome region in the MCA aneurysm were consistently exposed to higher WSS within a small local area with high spatial variation and little temporal change in comparison to other aneurysmal regions [2]. Another study, using mathematical models of the wall mechanics, proposed the formation of blebs as a likely path to aneurysm rupture [73]. The authors suggested that the formation of daughter aneurysms temporarily decreases the wall tension protecting the aneurysm from imminent rupture, until further growth elevates the tension leading to rupture. Later, a P-S CFD study of the development of small blisters in three aneurysms longitudinally followed suggested that low WSS magnitude (<10 dyne/cm^2) may trigger aneurysm progression and that blister formation is associated with high WSS gradient in the large region of low WSS [109]. In contrast, a CFD study of 30 blebs in 20 aneurysms showed that most blebs occurred at or adjacent to regions previously exposed to the highest WSS and were aligned with the inflow stream [22]. This study also suggested that once blebs form they develop counter circulation vortices and progress to a state of lower WSS.

Numerous studies have compared the hemodynamics of ruptured and unruptured aneurysms. A study of 53 P-S geometries argued that wide-necked aneurysms or those with wide-caliber draining vessels are high flow lesions that tend to rupture at larger sizes,

and that small-necked aneurysms or those with small-caliber draining vessels are low flow lesions that tend to rupture at smaller sizes [48]. Another study based on 62 P-S CFD models observed that concentrated inflow jets, small regions of flow impingement, complex and unstable flow patterns were more frequent in ruptured than unruptured aneurysms [20]. Subsequently, two case studies of aneurysms imaged immediately before they ruptured confirmed that these qualitative characteristics were present in these two aneurysms which were obviously at high risk of rupture [21, 102]. Later studies based on 210 CFD models confirmed these trends [24], and defined quantitative indices such as maximal WSS, the inflow concentration index (ICI), shear concentration Index (SCI), and viscous dissipation ratio (VDR) that were found to be higher (except for VDR which was lower) in ruptured than in unruptured aneurysms [23].

Another study [55] defined a flow impingement index (IMI) and showed that the maximum WSS increased with the IMI but the area of high WSS (defined as the region where WSS >0.5 max WSS) is not proportional to the size of impingement. Additionally, this study showed that there is a time delay between the flow impingement and the peak flow in the parent artery, which depends on the aneurysm size and heart rate [55].

In a recent study of one MCA aneurysm, non-laminar flow behavior was observed, and it was concluded that turbulence can be present in IA, causing increased WSS magnitude, increased frequency at which the WSS vector changes direction, and local pressure fluctuations; however it is unknown how these effects would alter cell remodeling and affect the wall [127].

CFD studies of Acom aneurysms [18], ophthalmic artery aneurysms [30], and terminal aneurysms [15] showed that ruptured aneurysms had on average higher WSS than unruptured aneurysms. In contrast, other studies found that ruptured aneurysms were under lower WSS [107] and had larger areas under low WSS than unruptured aneurysms [58, 128]. In another study, multivariate logistic regression analysis of morphological (size ratio, undulation index, ellipticity index, non-sphericity index) and hemodynamic parameters (average WSS, maximal WSS, low WSS area, average oscillatory shear index (OSI), number of

vortices, relative residence time) in 119 P-S CFD models identified WSS, size ratio and OSI as independent discriminants of aneurysm rupture status [141]. It has recently been argued that apparent discrepancies in CFD findings [61] arise from simplistic univariate analysis that can be resolved with multivariate analysis [139] and multi-population multicenter data [19, 95].

Finally, studying aneurysm growth is important because aneurysm rupture has been significantly associated with aneurysm growth during follow up [31, 59]. A few studies have compared the hemodynamics of growing and stable aneurysms longitudinally followed. One study compared a growing aneurysm to a stable aneurysm and observed abnormally low WSS (<10 $\mathrm{dyne/cm^2}$) in the region where the aneurysm grew [57]. Similarly, another study analyzed seven growing aneurysms and concluded that aneurysmal growth occurs at regions of abnormally low WSS [11] (<7 $\mathrm{dyne/cm^2}$). Another study considered 9 growing aneurysms and 16 stable ones and observed that complex, unstable flow patterns and concentrated inflows were more common in growing aneurysms, and that growing aneurysms had lower viscous dissipation ratios, higher maximum WSS, lower minimum WSS, larger areas under low WSS, and larger OSI [104]. Another CFD study of two growing tandem aneurysms of the PICA showed that the proximal multilobular aneurysm had high flow and physiological levels of WSS (4.5 $\mathrm{dyne/cm^2}$ to 12 $\mathrm{dyne/cm^2}$) in the region of growth, whereas the distal rounded aneurysm had low flow and low WSS (0.2 $\mathrm{dyne/cm^2}$ to 4.5 $\mathrm{dyne/cm^2}$) in the growing sac [118]. This study suggested that the growing region of an aneurysm could be exposed to either high WSS at the inflow zone or to low WSS and high OSI in the aneurysm sac.

Other studies compared the hemodynamics in stable aneurysms and in aneurysm that ruptured during the observation period. One such study compared 6 ruptured aneurysm to 26 stable aneurysms and found that the so called energy loss coefficient (EL) was higher in the ruptured group, but WSS was similar between the two groups [90]. Additionally, flow visualizations suggested that although the mean average inflow speed of ruptured aneurysms was 2 times higher than that of the stable aneurysms, the flow inside rup-

tured aneurysms appeared to undergo longer resident tracks, with stronger impact on the aneurysm wall. On the contrary, the flow inside stable aneurysms passed smoothly through the aneurysms. A second study analyzed 50 ICA aneurysms (6 ruptured during observation) and 50 MCA aneurysms (7 ruptured during observation) and concluded that a pressure loss coefficient (PL) was smaller in the aneurysms that ruptured for both locations, minimum WSS was lower for ruptured aneurysms in the ICA but not in the MCA, and average WSS, maximum WSS, OSI and EL were not significantly different between the two groups [120].

1.1.4 *Interaction between IAs risk factors*

Figure 2 summarizes the data and ideas presented in the literature reviewed in [28].

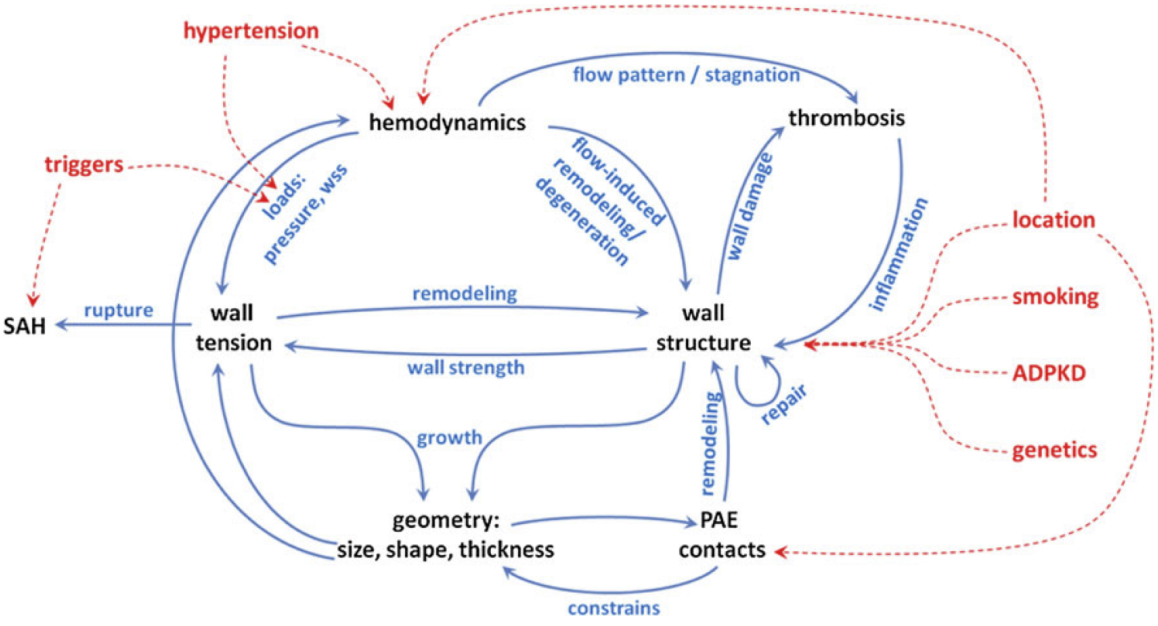

Figure 2: IA risks factors and their interactions.

Briefly, several factors induce biological processes in the wall that result in its progressive degeneration, remodeling, weakening and repair. The wall structure and hemodynamic loads determine the wall tension or stress which drives the geometric progression of the aneurysm. In turn, the aneurysm geometry, its size and shape, affects the flow pattern within the aneurysm sac. The hemodynamic environment together with the status of the aneurysm wall induce wall remodeling processes as well as thrombus formation and subsequent inflammation processes that affect the wall structure, thus closing the cycle. The PAE plays an important role when the aneurysm enters in contact with extravascular structures that constrain its shape thus influencing wall stresses and subsequent wall remodeling.

Other risk factors seem to indirectly influence this evolution cycle by either altering the hemodynamic loads or affecting the wall structure and cellular composition. Aneurysm location seems to be an important factor that influences the hemodynamics (e.g. through anatomic variants of the circle of Willis, arterial bifurcations), it also influences the wall structure (e.g. wall thickness at different locations, possible structural deficiencies at bifurcations), and determines whether the PAE is constraining or protective. Genetics and clinical factors seem to predispose the wall for aneurysm development or aggravate its chances of progression and rupture. Finally, rupture appears to occur when wall stress exceeds wall strength, typically precipitated by a trigger factor that suddenly increases the hemodynamic load (pressure).

Several studies have related hemodynamic and geometric variables to aneurysm formation, growth and rupture. However, to date, the results do not seem conclusive and in some cases seem to be in conflict. In our opinion, there are three main reasons:

1. the mechanisms of aneurysm development are multi-factorial, therefore finding a single variable that determines if an aneurysm will rupture may be difficult

2. there may be competing mechanisms simultaneously at play during the evolution of the aneurysms, for instance wall degeneration associated to abnormal nitrous

oxide (NO) production in response to high WSS, or wall degradation associated to inflammation from thrombus formation in regions of low WSS

3. the intrinsic limitations of the studies that have been carried out may prevent their direct comparison, generalization and interpretation.

Many studies have established correlations between geometric or hemodynamic variables and clinical events such as growth or rupture. The results of these studies have to be carefully interpreted. First, although correlation does not imply causation [61], understanding the causes of aneurysm development and progression may help us understand the observed correlations. Therefore, correlation studies are important to constrain theories of aneurysm evolution, since these theories should be able to explain observations such as the ones summarized in this review. Secondly, univariate statistical analysis identifies variables related to rupture, for example, while multivariate analysis retains independent variables with the strongest association to rupture and eliminates other dependent variables with weaker correlation to rupture. For instance, if max WSS and the low shear stress area (LSA) are not independent and one of them, say LSA, has a slight stronger correlation to rupture, it will be retained by the statistical model. However, this does not necessarily imply that the underlying mechanism is purely related to low WSS effects, it could actually be related to max WSS effects, or a combination of both. Therefore, it is important not only to identify variables connected to rupture (or other clinical events), but also to understand their inter-dependence.

The resolution of these apparent conflicts and identification of the mechanisms leading to wall degeneration and aneurysm progression will likely require multi-center studies based on a common approach and data selection criteria, uniform data analysis and modeling protocols, standardized variable definitions, and multiple populations [19, 95, 115]. Using longitudinal data of UIA, usually comprising small low risk aneurysms, is important to identify which of these aneurysms are likely to grow and subsequently rupture, and thus recommend their preventive treatment. On the other hand, the use of cross-sectional data (at a single time point) of ruptured and unruptured aneurysms is impor-

tant to identify larger aneurysms that perhaps should be conservatively observed, thus preventing unnecessary interventions. Large multi-center samples are important to obtain statistically significant results valid across populations. Finally, the combination of clinical, imaging, epidemiological, biomechanical and biologic data is important to test hypotheses about the underlying mechanisms governing the natural history of cerebral aneurysms.

1.2 TREATMENT OF INTRACRANIAL ANEURYSMS

Surgical clipping and endovascular treatment as coil embolization and flow diversion are the most common methods for treating intracranial aneurysms. Endovascular treatment has become the method of choice for many cases, as the craniotomy associated to clip litigation impose considerably more physiological stress in the patient. In the procedure of an endovascular treatment, a microcatheter is injected in the thigh and guided up to the location of the aneurysm. With the help of this microcatheter, the detachable coils are introduced into the lumen of the aneurysm. In most situations, several coils are used to clog the aneurysm. This arrangement is supposed to prevent high velocity blood flow inside the aneurysm.

Though commonly applied, clipping and coiling, however, present limitations in the cases of giant aneurysms, aneurysms with wide necks, or aneurysms affecting a significant portion of the parent vessel. In the situations where the neck of the aneurysm is not clearly defined, it is not possible to differentiate the aneurysm from the artery, and the clip or the coils can block the artery. As a workaround when inserting a coil in a aneurysm with wide neck, the interventionist can place a stent in the artery to cover the neck and to prevent the coil to occlude the parent artery.

Currently there is considerable interest in the use of flow diverting devices to treat cerebral aneurysms. The aim of these techniques is to reconstruct the parent artery by deviating the blood flow away from the aneurysm, thus creating a hemodynamic environ-

ment inside the aneurysm that is favorable for thrombosis and occlusion of the aneurysm. Figure 3 shows a scheme of the different endovascular treatment options.

(a) (b) (c)

Figure 3: Methods for endovacular treatments of aneurysm. (a) Coils, (b) coils supported by stents in cases of aneurysm with wide necks, and (c) flow diverting devices.

Assessment of the technical success of the intervention with a flow diversion device is difficult at the time of the procedure. When coiling an aneurysm, the interventionalist typically adds coils until no contrast fluid is seen entering the aneurysm, then the procedure is considered a technical success. Conversely, when a flow diverting stent is deployed across the neck of an aneurysm, there is almost always contrast entering the aneurysm even though the intra-aneurysmal flow pattern may already be adequate for thrombosis and successful occlusion of the aneurysm. Therefore, during the procedure, it is difficult for the physician to know whether the effect of the flow diverting stent will be enough or whether he/she needs to either deploy an additional stent or select a stent with lower porosity.

1.2.1 *Modeling of P-S hemodynamics*

Modeling blood flow through these endovascular devices in IA is crucial for improving their design, and to personalize and optimize endovascular stenting procedures in the treatment of aneurysms. Personalized simulations have demonstrated to be a fast, reliable

and inexpensive way of modeling blood flow inside these aneurysms. Studies using these models have the potential to replicate the exact anatomy of specific patients in order to connect specific hemodynamic factors to clinical events. Moreover, P-S CFD models before and after deployment of flow diverting devices can help physicians better plan their endovascular interventions using these devices.

A methodology has been previously developed [27] in the Center for Computational Fluid Dynamics at George Mason University, to conduct P-S studies including endovascular devices. It includes image-processing and segmentation algorithms, unstructured 3D grid generation, a finite element solver for Navier-Stokes equations, rheological models and visualization techniques. One of the applications of this methodology is the study of the alterations in the local hemodynamics of the vessel due to the introduction of a FD, a phenomenon which is yet not fully understood. Numerical simulation are well suited for the assessment of the complex nature of aneurismal flow in this case.

Nevertheless, this methodology for simulating the effects of endovascular devices currently presents important practical difficulties for clinical use. These simulations should be carried out in a few minutes on a typical workstation available in the angiography suite by trained but not necessarily expert modelers, but the computational time for these type of simulations is currently in the order of days. The memory requirements of a typical mesh of an aneurysm are such that the simulation can be run in a personal computer in a reasonable amount of time. However, the presence of a FD in the simulation can increase the simulation cost at least ten-fold and thus needs to be run in a supercomputer. The computational cost arises because endovascular devices present a rather dense and fine strut network, increasing the complexity and the size of the meshing.

Here, we present an alternative strategy to running a costly simulation of an aneurysm with a FD that significantly reduces the computational cost. In the present work, we discuss and validate the modeling of the FD as a porous medium. The advantages of this approach reside both in its simple implementation and the gain in computational time.

1.3 CFD SIMULATIONS OF P-S HEMODYNAMICS

1.3.1 *Reference works on techniques for P-S simulations*

The process of simulation of P-S hemodynamics from medical images can be divided into two major stages: anatomical modeling and blood flow modeling. These main stages involve multiple steps, and the complete set of sequential modeling stages is called a computational modeling pipeline [20]. The pipeline includes image acquisition, methods for image processing, segmentation techniques, stent deployment, grid generation and numerical simulations. Cerebral aneurysms are a particularly challenging problem due to the high degree of geometric complexity and the large number of steps involved in the modeling pipeline.

This methodology is not only applied to the study of a variety of vascular diseases [56, 29, 113], but also provides the possibility of studying the alterations to the flow pattern before and after an actual endovascular intervention. This type of study allows the clinician to plan the best treatment for a particular patient [124], and also gives valuable information for improving the design of these diverting devices.

When considering endovascular devices in the model, in addition to the difficulties of constructing the computational model of the artery and aneurysm, there is the challenge of creating the model of the device for this complex P-S geometry. In this case, it is necessary to design a method to deploy a given stent into a P-S vascular model. In Ref [78], this deployment is done in four steps which include 1) the extraction of the centerline of the parent vessel, 2) an initial cylindrical host surface generation, 3) the adaptation of this surface to the vessel wall, and 4) mapping a stent design on the generated surface. Additional challenge lies in the construction of acceptable computational grids inside the vessel and around the device. One of the traditional approaches is using body fitted grids, where the external mesh faces match up with the surface of the domain. This method, however, has the complications that the surface of the computational domain must be given by a

watertight assembly of analytical or discrete patches. For complex geometries and complex endovascular devices, it can be tedious and prone to errors [131, 35]. A different approach to obtaining a grid for these models is using an adaptive embedded-grids technique [4], which avoids the complication of body fitted grids and simplifies tremendously the meshing process [5]. In this technique, the grid is adaptively refined in the vicinity of the surface of the endovascular device, and the elements close to the immersed device surface are treated with the proper flow boundary conditions.

All these advances in medical imaging and vessel segmentation/reconstruction algorithms and techniques have led to increasingly widespread use of image-based CFD modeling of P-S cerebral aneurysm hemodynamics [25, 13, 116, 44, 1], not only for the study of the local hemodynamics, but also to infer the effects of endovascular therapy on it [113, 48, 108, 57]. Results from different research groups carrying out simulations of reproducible benchmark problems has been compared in the *Virtual Intracranial Stenting Challenge 2007* [91]. The aim was to establish the reproducibility of state-of-the-art simulation techniques in subject-specific stented models of IAs. The comparison shows that the results obtained by the different research groups are consistent, despite the diversity of grid generation and CFD technologies used.

1.3.2 *P-S CFD and its validation with experimental measurements*

CFD simulation has been previously validated for hemodynamics using several techniques, including analytical solutions [114] and *in vivo* comparison with flow velocity measurements obtained with phase-contrast MRI and Doppler ultrasound (DUS) [12]. Idealized CFD models are helpful to understand the hemodynamic characteristics in generic anatomical configurations, and idealized *in vitro* experimental studies have also been used often in the validation of CFD techniques. However, P-S models, which are necessary to relate the observed hemodynamic variables to the clinical events, have not been exhaustively validated against independent experimental measurements. To date, *in vitro* studies of

P-S cerebral aneurysm geometries have been limited to qualitatively CFD-particle image velocimetry (PIV) 2D comparison of flow fields, considering only the in-plane velocity component and scaled-up models that provide optical access [40]. Further validation of P-S models is necessary to improve the confidence in CFD simulations.

1.3.3 *The PMM as an alternative approach for P-S CFD*

The use of PMM is an alternative strategy for the modeling of FD which we explore in this work. A comparison between this approach and a simulation with a real stent geometry has been reported in a recent paper [7], showing a good similarity in flow pattern and magnitude. However, this work only considered only one type of stent design. It is largely unknown how to specify porosity parameters in the case of different FD designs, or how to account for the variation of the local stent porosity in its deployed state, which may be significantly different to the reference porosity, because of stent over-sizing and foreshortening. Besides stent porosity, there are other factors that affect the blood flow pattern, including strut design, and mesh hole shape. In Ref. [64], researchers report that changes in the performance of stents can be predicted from the hydraulic resistance of their flat mesh screens.

The limits of applicability of the PMM approach remain to be clarified as well as the required mesh resolution around the FD surface, both of which are the among the purposes of this work.

1.4 ORGANIZATION OF THIS WORK

The computational modeling pipeline described in the previous sections has proven to be a powerful tool to study the role of the hemodynamics forces in the stages of general cerebral aneurysms. The aim of this work is to solve the practical difficulties for the clinical

use of these tools in assessing the real risk of rupture and the effect of an intervention in P-S cases.

We study the differences between the results of the CFD simulations when compared against experimental measurements of realistic three-dimensional geometries (chapter 2). We use data sets from PIV measurements of three anatomically-realistic models corresponding to three stages of a growing cerebral aneurysm and evaluate quantitatively the degree of similarity of both three-dimensional velocity fields in the ranges studied.

In chapter 3, first we show that the geometric characteristics of a FD can be associated to a porous medium. Second, considering the FD as a flat wire screen, we use an empirical correlation for the pressure loss in flat wire screens to characterize the FD. We determine that the behavior of the FD can be predicted by the porous models in the Re interval of interest, by comparing the results of simulations using the PMM method to results obtained by several other methods.

Finally, we apply the PMM to a different combination of P-S geometries and FD (chapter 4), and compare qualitatively and quantitatively the results with the ones obtained using the immersed method (IMM) method. We discuss the results and their dependence to the porosity.

In chapter 5 we summarize the conclusions of this work.

VALIDITY OF CFD FOR P-S MODELS

Hemodynamics is thought to be a fundamental factor in the formation, progression and rupture of cerebral aneurysms [101] and its understanding is important to improve their rupture risk assessment and treatment. In this chapter we analyze the blood flow field in a growing cerebral aneurysm using experimental PIV and CFD techniques. This chapter includes the results presented in our peer-reviewed publication [93].

Three P-S models were constructed from longitudinal 3D computed tomography angiography (CTA) images acquired at one-year intervals. Physical silicone models were constructed from the CTA images using rapid prototyping techniques and pulsatile flow fields were measured with PIV. Corresponding CFD models were created and run under matching flow conditions. Both flow fields were aligned, interpolated, and compared qualitatively by inspection and quantitatively by defining similarity measures between the PIV and CFD vector fields. Results showed that both flow fields were in good agreement. Specifically, both techniques provided consistent representations of the main intra-aneurysmal flow structures, and their change during the geometric evolution of the aneurysm. Despite differences observed mainly in the near wall region and the inherent limitations of each technique, the information derived is consistent and can be used to study the role of hemodynamics in the natural history of intracranial aneurysms.

2.1 UNDERSTANDING EVOLUTION OF IA BY THE STUDY OF LONGITUDINALLY FOLLOWED CASES

Most previous studies of the hemodynamics of cerebral aneurysms have been limited to aneurysms imaged only once [20, 107, 128]. However, in order to improve our knowledge of the mechanisms governing the evolution of cerebral aneurysms it has become necessary

to analyze aneurysms that have been longitudinally followed during their natural evolution [11]. Only a few studies of the P-S hemodynamics in growing cerebral aneurysms longitudinally followed with 3D imaging have been carried out. This is a challenging task because typically most aneurysms are preventively treated and only a few which are considered to carry a low rupture risk are conservatively observed. In one of such studies, Jou et al. [57] analyzed a growing and a stable fusiform BA aneurysm that was followed for two years with MRI. They reported abnormally low WSS values in the area of aneurysmal growth and that the flow patterns did not change during the observation period. Similarly, Boussel et al. [11] analyzed seven growing cerebral aneurysms also longitudinally followed with magnetic resonance angiography (MRA), and again concluded that aneurysm growth occurs at regions of abnormally low WSS. Tateshima et al. [122] studied with PIV the flow dynamics in a growing middle cerebral aneurysm harboring a bleb. They observed little change in the flow fields before and after growth. They also observed flow separation at the margins of the bleb and a decrease in the flow and WSS within the expanding bleb. In most previous studies of cerebral aneurysms, the flow dynamics has been analyzed using both experimental [122, 123, 76] and computational [107, 113, 20] modeling. Several approximations and assumptions are made with each technique and each approach has its own set of limitations. Thus, the motivation of this study is twofold. The primary objective is to investigate whether experimental and computational models derived from longitudinal 3D medical images would produce consistent descriptions of the hemodynamics in cerebral aneurysms and its variations during the aneurysm progression. The second objective is to describe the blood flow fields observed during the evolution of a growing aneurysm. Note that the goal is not to reproduce exactly the experimental results with numerical models, but rather to investigate whether experimental and computational models constructed from the same images and under similar but not exactly matching assumptions and boundary conditions would yield consistent descriptions of the blood flow fields. Validation studies comparing CFD and PIV using P-S cerebral aneurysm geometries have been previously carried out [40]. This work extends those pre-

vious studies by considering a growing aneurysm and allowing for some freedom in the choice of approximations and assumptions typically made with each modeling strategy.

2.2 GENERATING *in vitro* AND COMPUTATIONAL P-S MODELS

2.2.1 *Clinical and image data*

An intracranial aneurysm with documented growth was selected from a database of unruptured, untreated cerebral aneurysms longitudinally followed with non-invasive 3D imaging [122]. Aneurysms in this database are classified as growing if their size changes by at least 0.5 mm in any direction, as determined by experienced neuroradiologists. The selected patient was a 51 years old male with a 6.5 mm aneurysm located in the Acom. Typically, aneurysms in this location receive blood from two sources: the A1 segments of the left and right anterior communicating artery (ACA). However, in this particular patient, the aneurysm is only fed from the left A1, the contralateral (right) A1 is missing (hypoplastic or aplastic). This patient has three A2 segments of the ACA, one irrigating the left hemisphere and two the right hemisphere. All these three A2 segments are supplied by the single left A1 segment. This aneurysm was imaged at one year intervals for four years between 2004 and 2008 using CTA. The CTA images consisted in 330 to 360 slices with 512 pixels $\times$ 512 pixels, an in plane resolution of 0.39 mm and a slice thickness of 0.5 mm. Because the aneurysm exhibited growth during the follow-up period, it was subsequently treated endovascularly with coils. Figure 4 shows volume renderings of the three longitudinal CTA images used in this study, corresponding to the initial exam and follow-up observations at 8 and 27 months. Arrows in this figure point to the regions of the aneurysm observed to enlarge. The volumes of the aneurysm region defined by a surface passing through the neck at each examination time were 0.33 cm^3, 0.32 cm^3, and 0.49 cm^3.

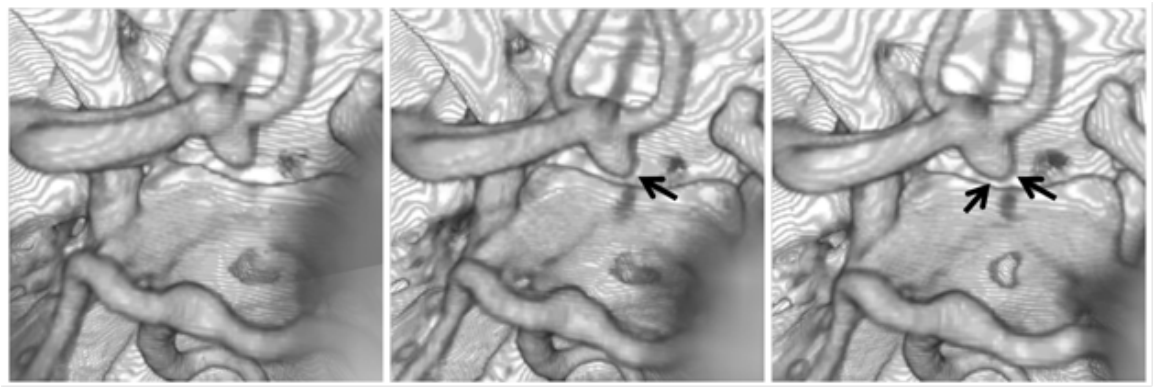

Figure 4: Volume-rendered longitudinal CTA images at three time points during the evolution of a growing IA it the ACA. Arrows point to the enlarging regions.

2.2.2 In vitro *models*

The aneurysm and connected arteries were manually segmented from the CTA images corresponding to each examination during the observation period. The resulting surfaces were smoothed to remove any stair-stepping artifacts and saved in stereolithographic format (STL). The three vascular models (named M1, M2 and M3) and their superposition are shown in figure 5. The STL surfaces were scaled 3:1 with respect to the *in vivo* anatomical dimensions and used to build corresponding silicon models using rapid prototyping techniques and a 3D printer (R-Tec Corporation, Japan). An example is shown in figure 6. These models were placed in a pulsatile flow loop and the velocity field was measured using PIV. The silicon models were considered rigid since the distance from the inner wall to the external flat wall of the block was thick enough to neglect its distention. The PIV system comprised a laser sheet for the visualization of 1 mm thick plane of the flow field, trigged at intervals of 150 µs, and a CCD camera with a resolution of 1376 pixels $\times$ 1040 pixels. The camera and laser oscillator were fixed on a commercial stage controller (Sigma Koki Co., Japan) to allow the positioning and rotation of the camera and

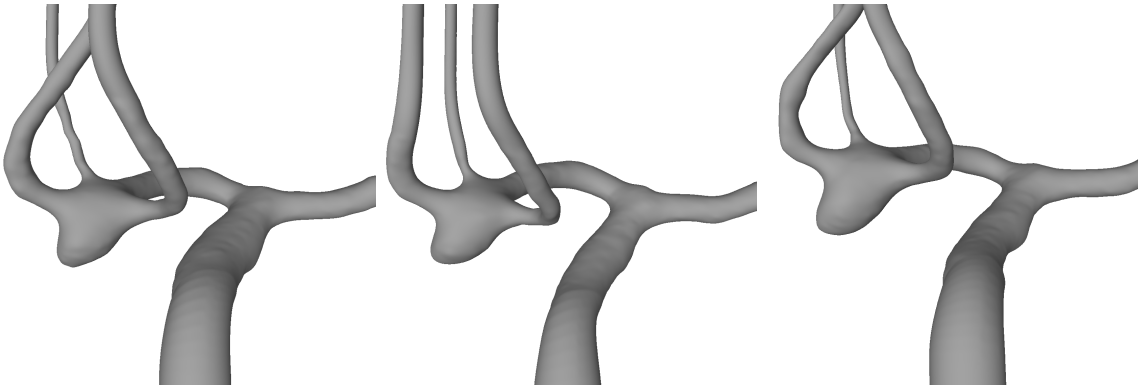

(a) model M1 (b) model M2 (c) model M3

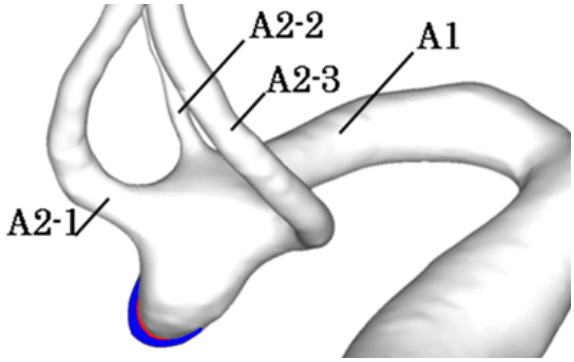

(d)

Figure 5: (a-c) Geometrical models of a growing IA at three time points during its evolution, reconstructed from longitudinal CTA images and used to construct corresponding PIV and CFD models. (Straight extensions added to inflows and outflows are not shown in the images.) (d) Superposition of the vascular models showing the regions of aneurysm enlargement (white: model M1, red: model M2, blue: model M3).

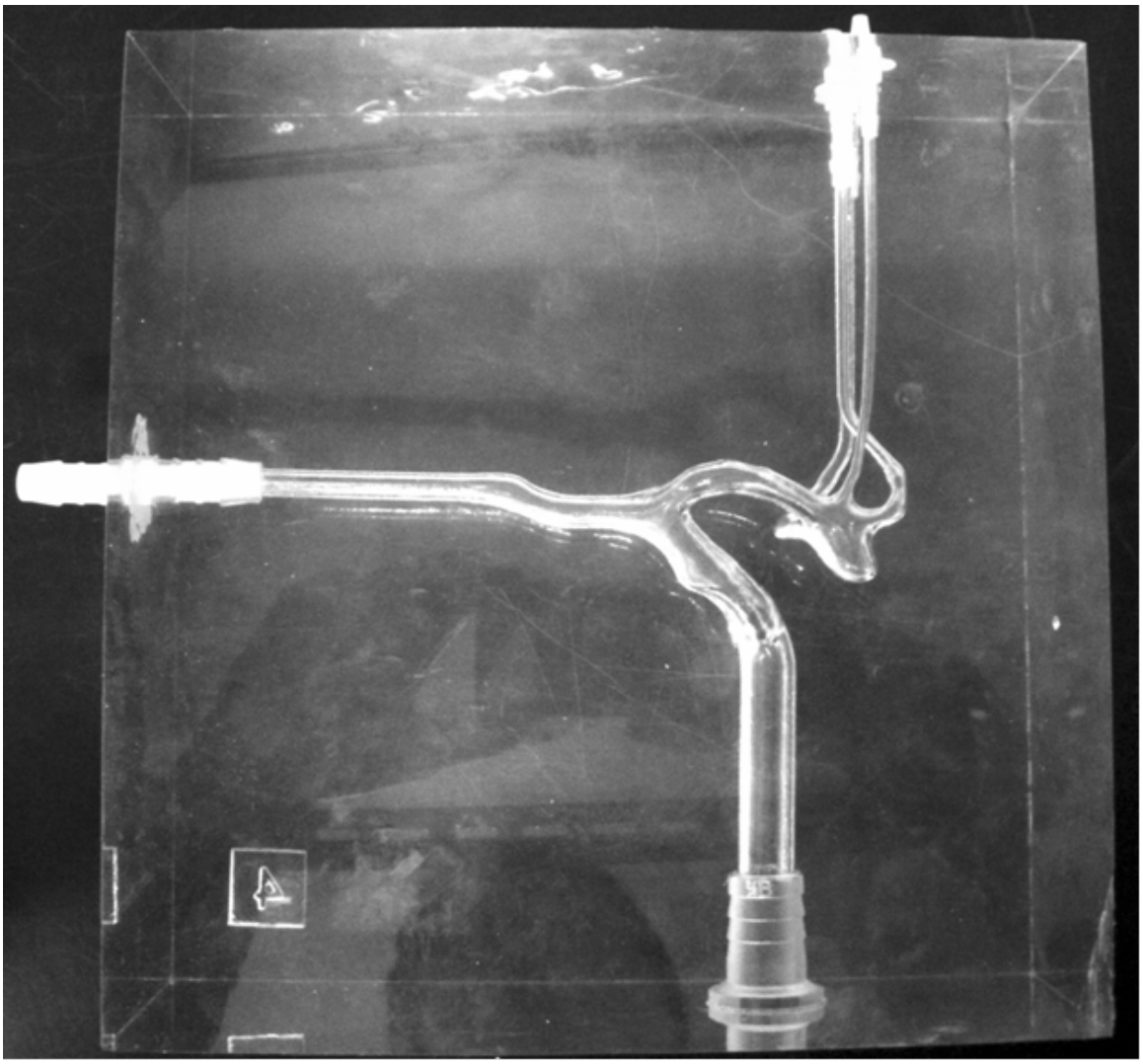

Figure 6: Silicone model of the aneurysm in the last CTA examination.

laser together. The working fluid used was a mixture of glycerin and water. To eliminate optical distortions, the refraction index of the working fluid was matched to that of the silicon resin by continuously varying the content of glycerin while checking the distortion of a pattern observed through the model. A solution of 58 % glycerin by weight gave the best match to the silicon refraction index of 1.409. The viscosity and density of this working fluid were $\mu = 0.0082\,\mathrm{Pa\,s}$ and $\rho = 1140\,\mathrm{kg/m^3}$, respectively. The PIV system was calibrated using images acquired in the PIV system and the STL data. With a slight change of the refraction index of the working fluid, the outline from the silicone inner wall on a measuring plane could be acquired on the PIV image. Counting the pixels on the image (e.g., the radius of the parent artery), the number of pixels was converted to a length (mm) based on the STL data on the same plane. The velocity vector field was calculated from the double-frame acquired images based on the path of the particles. The pulsatile flow conditions were derived from *in vivo* ultrasound measurements of flow velocities in ACAs of normal subjects [50]. The inflow waveform was generated by adding a pulsatile flow to a steady flow. The pulsatile flow was produced by a pulse generator, which consisted of a numerically positioning-control servomotor (VLBS-A11012; Toei Electric, Tokyo, Japan) and a bellows pump (WB-0075629; Eagle Industry, Tokyo, Japan). In order to trigger the PIV system to collect images at the same point in the cardiac cycle, a douser was fixed at the edge of the turn table on the pulse generator. This douser passed a photointerrupter at the start point of each pulsatile cycle, producing a signal which was digitized by a G-program written in Labview software (National Instruments, Co.) in order to transmit the start point to the PIV system and trigger the laser pulse and the camera at the same time via a synchronizer. The PIV data were averaged through 30 cycles. During the PIV experiments, the flow in the A1 segment of the *in vitro* model was measured with ultrasound (figure 7), and the inflow waveform was controlled to mimic the waveform shape and to match the Reynolds and Womersley numbers of the *in vivo* measurements. The Reynolds number based on the ACA diameter varied in the range of 450 to 800 and the Womersley number was 2.7. The flow in the outflow branches was set proportional to

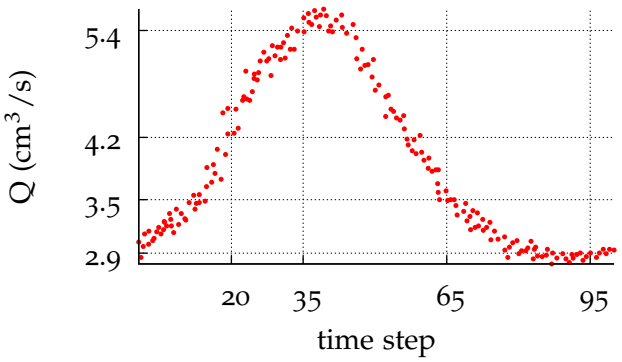

Figure 7: Pulsatile flow waveform measured at the A1 segment of the PIV model, and used to derive flow boundary conditions for the CFD model. The marks horizontal axis indicate the PIV measurements during the cycle.

the corresponding vessel areas. Straight vessel segments were added at the model inlets and outlets to minimize boundary effects and allow for flow development. Because this PIV system cannot measure three-dimensional flow fields, the in-plane components of the flow velocity were measured on two sets of orthogonal planes separated by 1.0 mm at four instants of time during the cardiac cycle. The sets consisted in 19 planes perpendicular to the x-direction and 15 planes perpendicular to the y-direction. Each plane had a resolution of 43 points $\times$ 32 points, and the separation between points was 0.82 mm in each direction for the first set and 0.78 mm for the second set.

An estimation of the error or uncertainty of the PIV velocity measurements was obtained by comparing the z-velocity component, which was measured twice, once in the set of planes normal to x and again in the set of planes normal to y. Each measurement is the average over the 30 cardiac cycles. The absolute difference between the z-velocity of each measurement was calculated and averaged over the region of interest. The difference varies during the cardiac cycle between 4 % and 10 % of the peak systolic velocity. More details about the experimental setup and PIV measurements can be found in [76].

2.2.3 *Computational models*

The CFD models of the aneurysm at each stage of its evolution were created from the corresponding STL surfaces. The computational models were built with a 1:1 scale with respect to the *in vivo* geometry. Unstructured grids composed of tetrahedral elements were generated using an advancing front technique and a minimum resolution of 0.02 cm [71, 27]. The resulting grids contained approximately 1.92×10^6, 1.77×10^6, and 1.84×10^6 elements, respectively. Blood flow was mathematically modeled using the unsteady 3D Navier-Stokes equations for an incompressible Newtonian fluid. The governing equations were advanced in time using a fully implicit scheme [25] that recasts the original equations as a steady-state problem in pseudo-time (θ) at each time-step (n):

$$u^{\xi}_{,\theta} + u^{\xi} \cdot \nabla u^{\xi} + \nabla p^{\xi} = \nabla \eta \nabla u^{\xi} - \frac{u^{\xi} - u^{n}}{\xi \Delta t} \tag{1}$$

and

$$\nabla \cdot u^{\xi} = 0, \tag{2}$$

where u is the velocity, p the pressure, ξ the kinematic viscosity, u^n denotes the velocity at the previous timestep and $u^{\xi} = (1 - \xi)u^n + \xi u^{n+1}$. These equations are solved using a pressure-projection method where the spatial discretization is carried out using an edge-based upwind finite element method [71]. The discretized momentum equation is solved using a generalized minimal residuals (GMRES) method and the discretized pressure Poisson equation is solved using an efficient deflated preconditioned conjugate gradients method [79]. The flow waveform measured in the A1 segment of the PIV model (figure 7) was scaled to get matching Reynolds and Womersley numbers for the CFD model. The flow rate at the CFD inlet boundary in the ICA and the outflow through the MCA were adjusted to match the scaled waveform at the A1 segment as closely as possible. A fully developed Womersley velocity profile was imposed at the model inlet. Traction-free boundary conditions were prescribed at the outlets and no-slip boundary conditions

on the vessel walls. The pulsatile simulations were carried out using 100 timesteps per cardiac cycle, for a total of two cardiac cycles. Results are presented for the second cycle.

2.2.4 *Post-processing*

The two sets of orthogonal PIV measurements of in plane flow velocities were used to recover a 3D velocity field at each instant during the cardiac cycle and for all the aneurysm geometries. Both sets of planes were interpolated and combined into a new data set. The combined volume was limited to the intersection of both sets, as it was necessary to have information of all three velocity directions. The resulting grid consisted of approximately 20 000 points. The velocity vector field was linearly interpolated to each point and the z-component (measured in both sets) was averaged between the two original sets. This new 3D PIV dataset included points within the fluid volume and points in the external space. Therefore, this dataset was masked to identify the points that belong to the fluid volume (i.e. with a non-zero velocity). Because the construction process of the *in vitro* model does not preserve the coordinate reference frame of the original CTA image data, it was necessary to align the 3D PIV and CFD dataset. This alignment was carried out manually until the models visually matched as closely as possible. Once aligned, the 3D PIV velocity data was interpolated to the CFD mesh points for comparison. Finally, in order to compare the flow fields of dynamically similar models (i.e. with same Reynolds and Womersley numbers but different scales) it was necessary to make the velocity fields non-dimensional. This was done by using the corresponding peak systole velocity magnitudes as the velocity scales. Subsequent flow visualizations and quantitative comparisons were carried out using the dimensionless velocity fields.

2.2.5 *Flow visualization*

The instantaneous intra-aneurysmal flow patterns were visualized using streamlines color coded according to the local velocity magnitude. In order to depict the overall flow structure, a total of 100 streamlines were initiated at randomly selected locations within the aneurysm volume and traced in the forward and backward velocity directions. The flow structure was also visualized using a vortex coreline detection algorithm. Vortex corelines are defined in this work by the locus of points which share two of the following properties [96, 84]: 1) the velocity and acceleration vectors are parallel, and 2) the instantaneous streamline curvature is zero. Mathematically, these conditions can be expressed in the form of an eigenvalue equation

$$\mathcal{U} \cdot u = \lambda u, \tag{3}$$

that is satisfied by points in the computational domain where the velocity vector is an eigenvector of the velocity gradient tensor $\mathcal{U}$. Corelines are computed algorithmically in the computational domain using the eigenvector method of Sujudi and Haimes [119]. For each tetrahedral element, the following steps are applied:

- Compute and diagonalize the Jacobian matrix for the host element.
- Verify that the eigenvalue spectrum consists of one real eigenvalue and a pair of complex conjugate eigenvalues. If this condition is not satisfied, skip to the next element.
- Form a reduced velocity vector w at each node in the element by subtracting the components of the velocity that point along the eigenvector associated with the real eigenvalue ξ_R. The reduced velocity can then be expressed as $w = u - (u \cdot \xi_R)\xi_R$.
- For each face on the element, use linear interpolation to determine if there is a point on that face where the reduced velocity is zero. If two faces are found to have a zero point, the element is marked to contain a coreline segment.

2.2.6 *Comparison indices*

In order to quantitatively compare the CFD and PIV velocity fields, two simple indices for measuring their similarity were defined inspired in the measures described in [68]. The first measure, called the angular similarity index (ASI), is defined as the cosine of the angle subtended by the CFD and PIV velocity vectors at a given point in space:

$$\mathrm{ASI} \equiv \frac{u_{\mathrm{CFD}} \cdot u_{\mathrm{PIV}}}{|u_{\mathrm{CFD}}||u_{\mathrm{PIV}}|} \tag{4}$$

This index varies in the range [-1, 1], being 1 the highest angular similarity. The second measure, denoted magnitude similarity index (MSI), is based on the absolute difference between normalized velocities, and is defined as:

$$\mathrm{MSI} \equiv 1 - |\frac{|u_{\mathrm{CFD}}|}{\max(|u_{\mathrm{CFD}}|)} - \frac{|u_{\mathrm{PIV}}|}{\max(|u_{\mathrm{PIV}}|)}| \tag{5}$$

This index varies in the range $[0, 1]$, being 1 the highest magnitude similarity. Finally, corresponding global similarity measures were then obtained from the point-to-point similarity indices as the volume integral of angular and magnitude similarities over the region of interest divided by the aneurysm volume.

2.3 COMPARISON BETWEEN CFD SOLUTION AND PIV MEASUREMENTS

In the previous section, realistic *in vitro* and computational hemodynamics models at three time points during the natural evolution of a growing intracranial aneurysm were constructed using the P-S geometry derived from longitudinal CTA images and pulsatile flow conditions. In this section, these models were used to compare the CFD and PIV flow fields, and to describe the intra-aneurysmal hemodynamics and its change during the aneurysm progression.

2.3.1 *Flow description and qualitative comparison*

Visualizations of the intra-aneurysmal flow patterns are presented in figure 8. Each panel of this figure (left, center and right) shows the CFD (left column) and PIV (right column) flow fields at the four instants of time during the cardiac cycle (rows), using instantaneous streamlines colored with the local velocity magnitude.

It can be seen that the CFD and PIV flow fields are in good qualitative agreement and that both techniques yield a consistent description of the intra-aneurysmal hemodynamics for all geometries and all times during the cardiac circle. Specifically, these visualizations show that a thin layer of blood enters the aneurysm at the distal part of the orifice, impacts against the distal part of the aneurysm body, recirculates within the aneurysm sac and swirls into the three daughter branches (A2's), although the most proximal A2 branch (A2-2) receives most of its flow from the proximal parent vessel and exhibits much less swirling. The overall flow structure persists during the cardiac cycle and the main recirculation region expands and contracts as the flow accelerates and decelerates from the systolic to the diastolic phase. As the aneurysm grows, the main recirculation region becomes more elongated towards the aneurysm dome and changes slightly the position and orientation of its axis of rotation.

Although the CFD and PIV techniques yield consistent flow patterns, there are differences between the corresponding flow fields that can be observed in figure 8. First, in general the velocity magnitudes are higher in the CFD models than in the corresponding PIV models. Secondly, the PIV streamlines stop inside the aneurysm, near the wall. Thirdly, the PIV velocity magnitude is noticeably smaller close to the wall in the flow impingement region. In particular, the PIV velocity magnitude along streamlines seems to decrease as the streamline approaches the wall at the impingement location and then recovers its original values after the impingement zone.

In order to analyze the similarities and differences of the CFD and PIV flow patterns and their variability during the cardiac cycle and during aneurysmal evolution, vortex

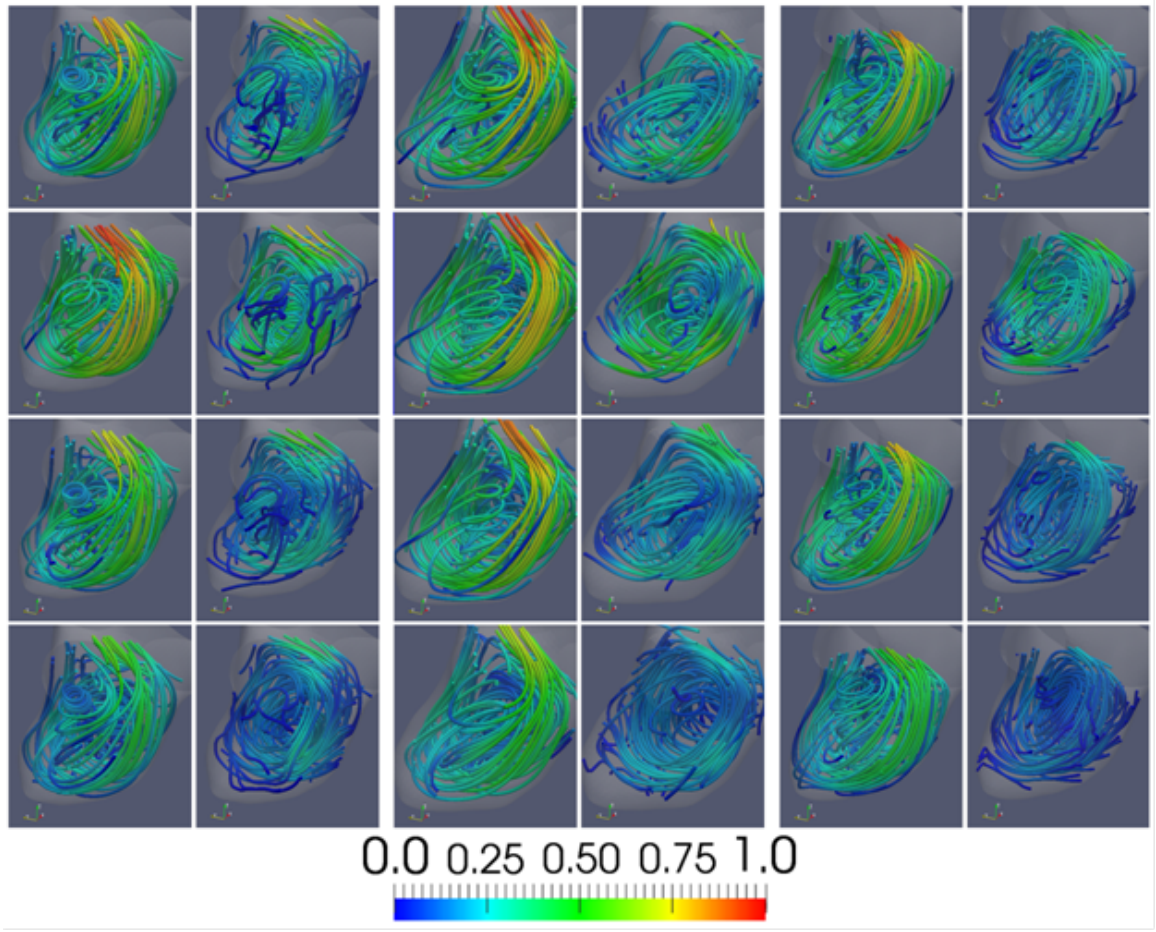

Figure 8: Visualization of aneurysmal flow pattern using streamlines. The panels from left to right show the flow pattern at the three time points during the evolution of the aneurysm (corresponding to models M1, M2, and M3 of figure 5). The left column of each panel shows the CFD flow field, while the right column the PIV flow field. The four rows show the flow fields at four instants of time during the cardiac cycle (time 1, 2, 3 and 4 of figure 7).

corelines were computed and visualized. Figure 9 presents the CFD and PIV vortex corelines detected in the CFD (black) and PIV (red) flow fields for each of the aneurysm geometries (columns) and time instants during the cardiac cycle (rows). Again, these visualizations show that the CFD and PIV techniques yield consistent descriptions of the intra-aneurysmal flow structures.

Essentially, the flow swirls around one main vortex coreline aligned with the outflow vessels (A2 branches) and bend towards the dome of the aneurysm. For each aneurysmal geometry, the main structure of the flow does not change substantially during the cardiac cycle, although some variability in the shape and location of the vortex corelines can be observed. It can be seen that the CFD and PIV vortex corelines tend to coincide. The largest differences are observed at end diastole, where the PIV lines have smaller curvatures and penetrate less towards the aneurysm dome than the CFD lines. This difference in turn results in a larger variability of the PIV flow structures during the cardiac cycle than the CFD data. The differences observed between the vortex corelines detected in the CFD and PIV flow fields are consistent with the differences in the velocity magnitudes observed in the streamline visualizations presented in figure 8. For instance, the CFD lines are seen to penetrate deeper towards the aneurysm dome, consistent with higher velocities observed in the CFD flow field. As the aneurysm progresses, changes in the flow structure can also be observed. The aneurysm geometry expands mainly in the distal and right side of the wall (left on figure 9). As the aneurysm elongates, the vortex corelines increase their curvatures and elongate accordingly (see changes from the left to the middle column in figure 9). As the aneurysm continues to expand (from the middle column to the right column of figure 9), the corelines recover a smoother shape but now penetrate less towards the dome; this is consistent with the previously described elongation of the main flow recirculation region observed in figure 8. These changes in the aneurysm flow structure during its evolution are consistently observed in both the CFD and PIV data.

Visualizations of the CFD and PIV velocity fields at peak systole (time 2) on four selected cut planes (P1-P4) are presented in figure 10 for models M1 and M3. These visualizations

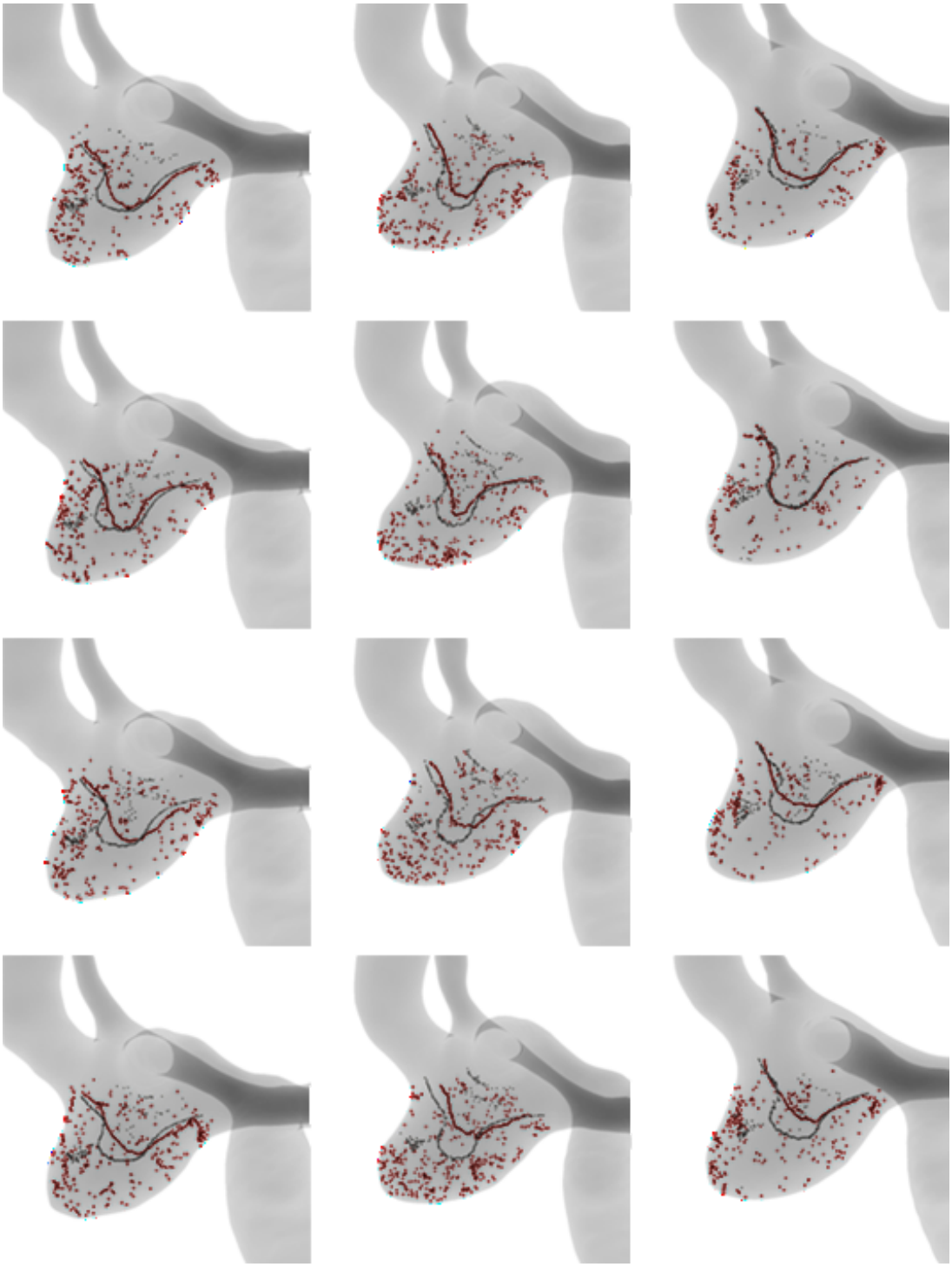

Figure 9: CFD (black) and PIV (red) comparison of aneurysmal vortex corelines. From left to right: models M1, M2 and M3 of figure 5); from top to bottom times 1, 2, 3, and 4 of the cardiac cycle (figure 7).

show cuts of the main vortex structure within the aneurysm volume. It can be seen that the CFD and PIV techniques provide consistent descriptions of the velocity field. The major differences between the CFD and PIV velocity fields are observed near the walls. For instance on plane P1 (left most column of figure 10) which is close to the aneurysm side wall, as well as near the flow impaction zone at the distal aneurysm wall. As the aneurysm progresses from geometry M1 to M3, it can be seen that the core of the main vortical structure has enlarged. Additionally, these visualizations show that before enlargement (model M1) the flow is attached to the wall at the dome, but as the aneurysm grows (model M3) a region of slow flow develops at the location of geometric progression and the flow seems to separate from the wall (see the bottom part of the aneurysm in planes P2 and P3 of figure 10). These features are consistently observed in the CFD and the PIV flow fields.

2.3.2 *Quantitative comparison*

The CFD and PIV flow fields were quantitatively compared using the ASI and MSI described before. As explained before, the PIV data was interpolated to the CFD grid points and the similarity measures were then computed on the CFD grid. At the vessel wall, where the velocity is zero, the ASI yields a zero similarity, while the MSI yields a value of one. Furthermore, the PIV technique is known to suffer from larger measurement errors close to the walls. Thus, in order to study the influence of near wall errors, grid points close to the wall at progressively increasing distances to the wall were discarded and the similarities were re-calculated. In other words, the total similarity was computed as the integral of the similarity over the aneurysm region discarding a thin layer close to the wall. The thickness of this layer was varied from zero (thus including the entire aneurysm volume) to $1.5\,p_{PIV}$, where p_{PIV} represents the in-plane pixel size of the PIV measurements (0.78 mm). The results are presented in figure 11. This figure shows the total ASI and MSI computed for each geometrical model at the four time instants during the cardiac cycle. The dif-

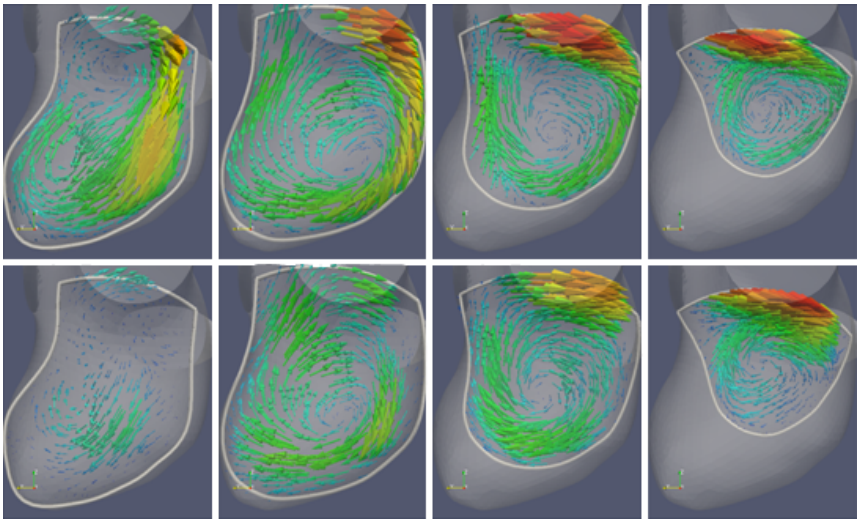

(a) model M1

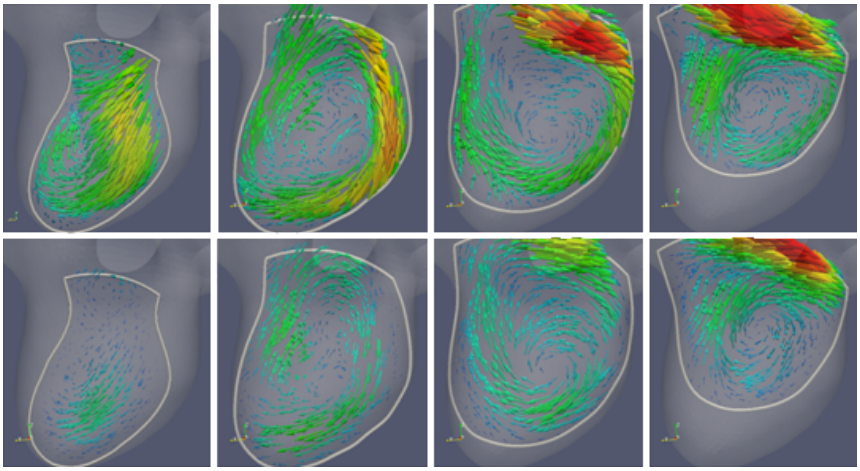

(b) model M3

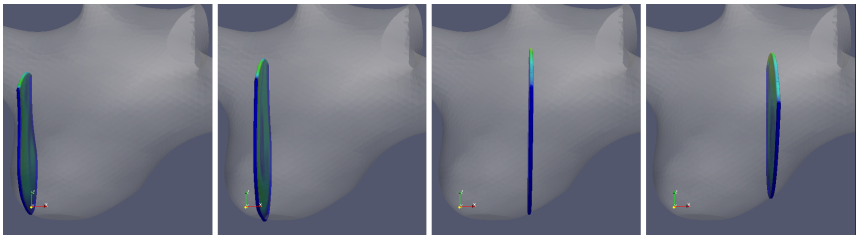

(c) Location of cut-planes P1 to P4 in aneurysm

Figure 10: Visualization of velocity vectors at peak systole for models (a) M1 and (b) M3. Top row of each panel shows CFD fields, and bottom row PIV fields. Each column corresponds to a cut-plane located as shown in (c).

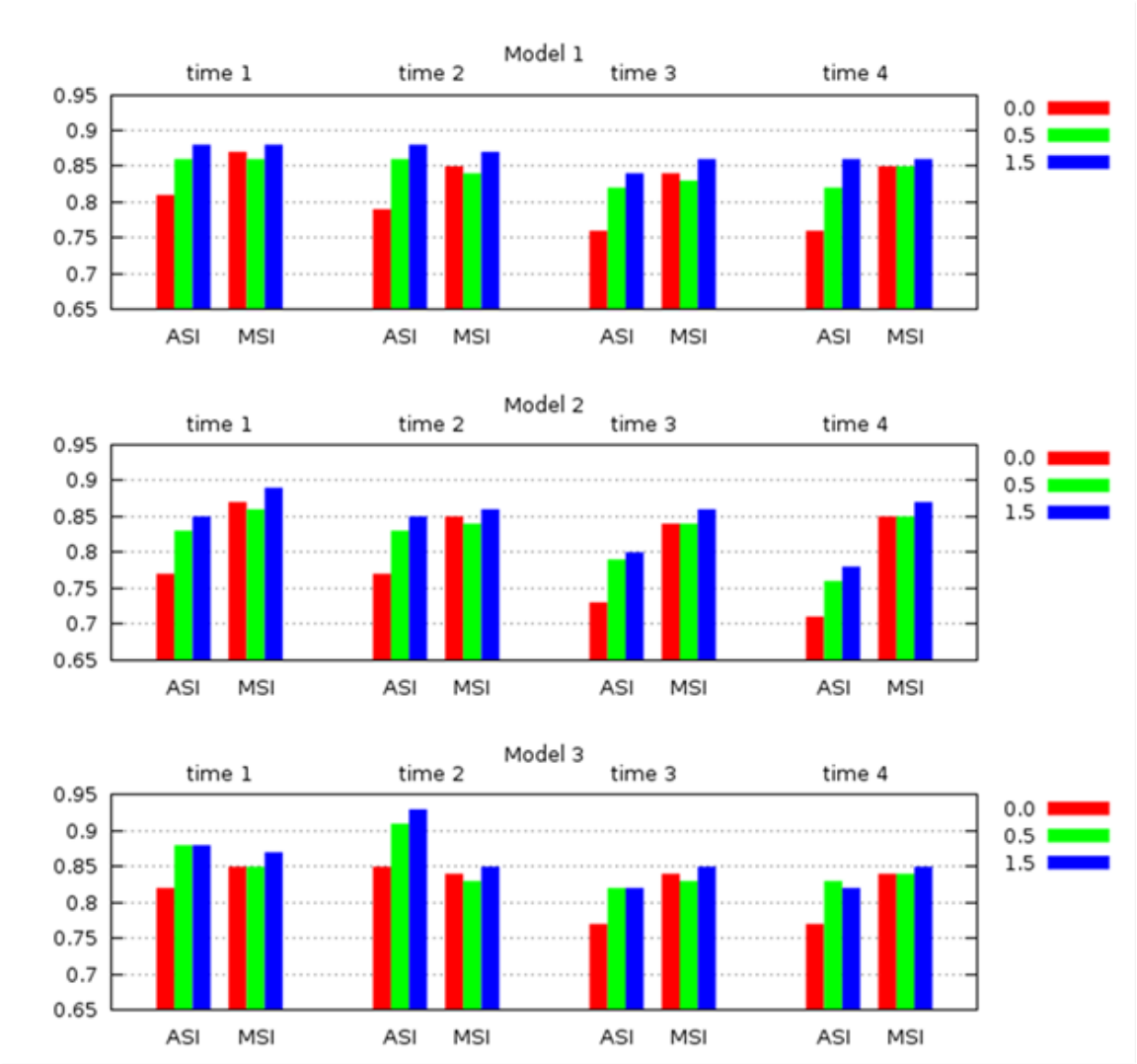

Figure 11: Total ASI and MSI between the CFD and PIV flow fields, for each of the three model geometries and at each of the four instants of time during the cardiac cycle. Values are plotted after discarding points in a layer near the vascular wall of thickness corresponding to 0, 0.5 and 1.5 PIV pixels.

ferent bars indicate the values obtained after excluding a layer of $0.0\,p_{PIV}$ (red), $0.5\,p_{PIV}$ (green) and $1.5\,p_{PIV}$ (blue) from the aneurysm wall. Other intermediate values were computed ($0.25\,p_{PIV}$ and $1.0\,p_{PIV}$) but are not displayed in this figure as they do not add extra information. These results indicate that the CFD and PIV have a quantitative agreement above 75% for all models and all times, except for the ASI of model M2 at times 3 and 4 which only reaches 70%. If a layer along the aneurysm wall of thickness equal to a half of the PIV measurement pixel size ($0.5\,p_{PIV}$) is excluded, the total similarity is above 80%, and if the layer thickness is increased to $1.5\,p_{PIV}$, then the overall similarity is above 85%. These results suggest that the CFD and PIV flow fields are in good quantitative agreement, especially in the interior of the aneurysm volume.

In order to illustrate the differences between the CFD and PIV flow fields, the ASI and MSI measures plotted on the four selected cut-planes are presented in figure 12 for models M1 (top panel) and M3 (bottom panel). Overall, these visualizations show good quantitative agreement between the two fields. The largest differences or lower similarities are observed near the wall. In particular, PIV seems to under-resolve the flow structure in the region where the thin inflow stream impacts the aneurysm wall, where the PIV inflow stream seems to disappear right before the impaction against the wall and to re-appear after the impingement region. Additionally, low ASI are observed in regions of low flow velocity.

2.3.3 *Sources of error and uncertainties*

The CFD and PIV results were found to be in good qualitative as well as quantitative agreement for all time instants during the cardiac cycle and for all stages of the evolution of the aneurysm. However, differences in the corresponding flow fields were observed. There are a number of sources of error and uncertainties that are briefly discussed in what follows. First, higher velocity magnitudes were observed in the CFD flow fields. This is likely due to an imperfect match of the non-dimensional parameters characterizing the flow, namely

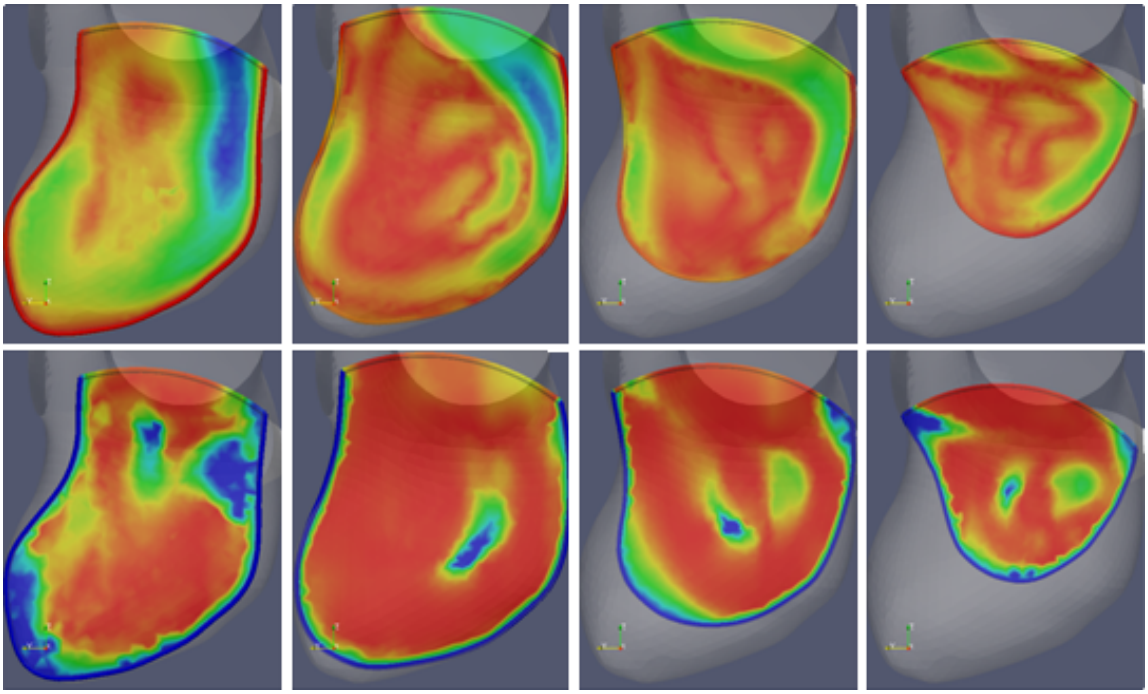

(a) model M1

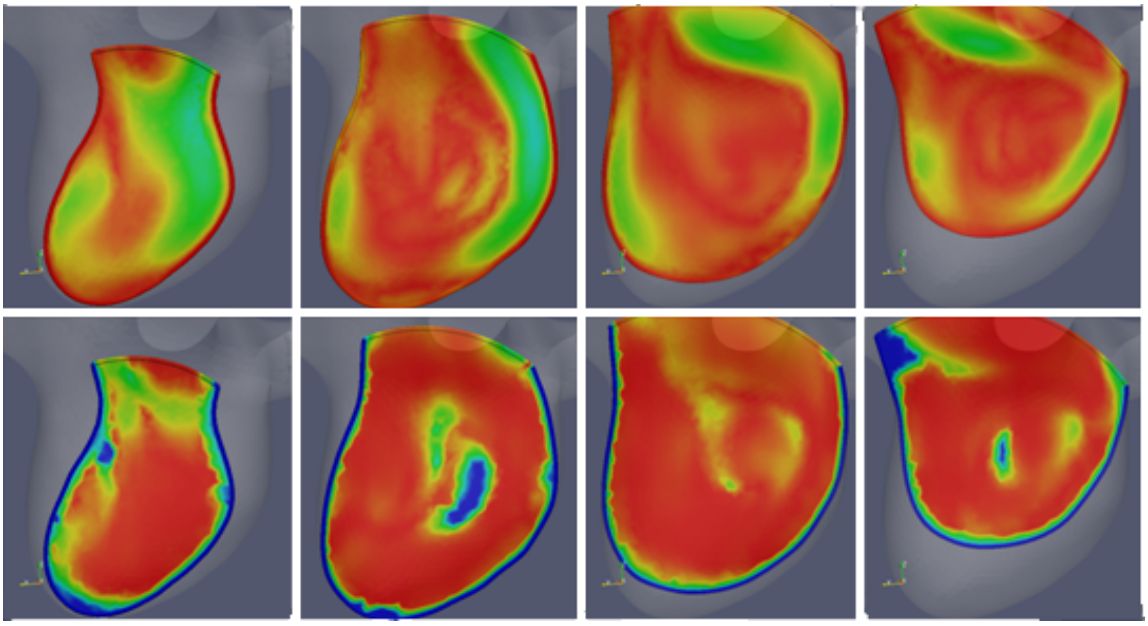

(b) model M3

Figure 12: Visualization of the local similarities between CFD and PIV flow fields for models (a) M1 and (b) M3, at peak systole. Top row of each panel shows MSI, and bottom row ASI. Each column corresponds to a cut-plane located as in figure 10c.

the Reynolds number and the Womersley number. The Reynolds number was computed from ultrasound velocity measurements obtained at the A1 branch proximal to the aneurysm in the *in vitro* model. In order to match the experimental Reynolds number, the inflow boundary conditions in the CFD model were adjusted to obtain similar maximal velocity values at roughly the same location as the ultrasound measurements. However, the exact location of these measurements was not known, thus this introduces uncertainty in the flow conditions which likely results in non-matching velocity magnitudes. Secondly, some streamlines computed using the PIV velocity fields stopped inside the aneurysm volume. This implies a non-zero divergence of the PIV velocity field. In order to estimate the error introduced by this effect, the divergence of the normalized PIV velocity field was computed. The error in the velocity introduced by a non-zero divergence was then estimated by calculating the absolute value of the divergence averaged over the volume of the region of interest. This mean divergence induces an average variation in the velocity over a pixel volume of up to about 0.41 %. However, these errors were larger close to the walls where they reached values of approximately up to 12 % to 40 % during the cardiac cycle. The PIV measurements obtained on sets of orthogonal planes were combined into a 3D vector field by simple interpolation. The experimental data was not manipulated or filtered to obtain a divergence-free field. Thus, the observed behavior of streamlines is most likely due to measurement and interpolation errors. Thirdly, differences between the CFD and PIV fields were observed close to the aneurysm wall, in particular at the location of the impingement of the thin inflow stream against the aneurysm wall.

Probably, these differences arise because of measurement errors of the PIV technique that are expected near the walls [92]. These findings are similar to those described by Ford et al. [40]. In particular, they observed stronger flow and higher velocities in the CFD than in the PIV models. They also reported that the PIV measurements did not capture details of the flow fields in the near wall region, and observed disagreements between the CFD and PIV fields in a few regions in the interior of the aneurysm volume away from the walls.

Finally, differences in the experimental and computational modeling assumptions could also have introduced discrepancies in the flow fields. Both the PIV and CFD models were constructed starting from the same STL data in order to discard differences due to different segmentations which have been previously studied [133]. However, the final physical *in vitro* model constructed from the STL data may have geometric differences with the original STL data that can influence the flow results. Additionally, traction free boundary conditions were used at the outflows of the CFD models. This is a common approximation in many CFD models where it can reasonably be assumed that the distal vascular beds of the corresponding vessels (A2's in this case) have comparable resistances to flow. However, in the PIV experiments the outflow rates were modulated with the vessel area.

This difference in the modeling assumptions may introduce differences between the CFD and PIV flow fields. The differences in the CFD and PIV fields in turn affect the ASI and MSI measurements. These similarities are also affected by any misalignment of the CFD and PIV models or slight differences in the location of the corresponding flow structures. Furthermore, the ASI is prone to produce large differences in regions of slow flow, as has been illustrated in 10 (right panel, center of plane-cut). Finally, it was observed that the largest differences between the CFD and PIV results occur during the diastolic phase. This observation also suggests that if this assertion could be generalized, then hemodynamic variables based on systolic values defined for assessing risk of growth or rupture would probably have less dispersion and variability than variables based on diastolic values.

2.4 DISCUSSION AND CONCLUSIONS FROM THE COMPARISON

The results of the current study indicate that image-based CFD and PIV models yield consistent representations of the blood flow patterns in growing intracranial aneurysms, and their change during the natural evolution of the aneurysms. In particular, it was found that in the aneurysm considered, although the intra-aneurysmal flow pattern did exhibit some changes during aneurysmal progression these changes were not dramatic. This im-

plies that the geometrical deformation of this aneurysm is small enough not to cause substantial changes in the structure of the intra-aneurysmal flow pattern, suggesting also a relatively slow aneurysmal progression. This observation is consistent with previous studies describing the hemodynamics in other growing cerebral aneurysms using CFD techniques in which the flow patterns were seen to persist (not change significantly) during the evolution of the aneurysms [11, 57]. However, some interesting observations at the location of aneurysm progression were made, consistently in both the CFD and PIV flow fields. Specifically, it was observed that as the aneurysm grew, a region of slow flow develops at the location where the wall expands, and that the flow in this region seems to separate from the wall. This observation is consistent with previous results related to bleb formation which suggested that as blebs form new counter current recirculation regions with slow flow are formed within the blebs, and that the blebs progress to states of lower WSS [22]. Further investigations of the relationship between hemodynamics and aneurysm progression, including more aneurysms and analysis of the WSS fields are needed in order to further understand the mechanisms of aneurysm evolution.

Image-based CFD and *in vitro* PIV models based on P-S geometries of a growing cerebral aneurysm were in good qualitative and quantitative agreement despite different assumptions and approximations made with each approach. The main differences between the two methods were found in regions close to the wall, in regions of slow flow and during the diastolic phase. Despite these differences, the representations of the intra-aneurysmal hemodynamic patterns provided by each technique were remarkably similar. The two techniques provided consistent descriptions of the intra-aneurysmal flow patterns and their variability during the cardiac cycle and during the natural evolution of the aneurysm. This implies that both approaches can be used to study the role of hemodynamics in the mechanisms governing the pathogenesis, growth and rupture of intracranial aneurysms. However, each approach has its own limitations, which must be carefully considered when interpreting the results produced by each technique.

FLOW DIVERTER MODELED AS A POROUS MEDIUM

There are numerous types of porous media and a broad range of applications for them. Accordingly, there are many models describing fluid flow through porous media. Heat transfer, acoustic microscopy, drying of edibles, and contaminant transport are, among many others, examples of areas where models of porous media can be applied. By introducing a novel way of modeling flow diversion, our goal is to incorporate flow diversion models as a new area of application for porous media.

In this work, our approach to the computational simulation of FD is to utilize a PMM that recreates the pressure drop in an equivalent FD, considered as a flat wire screen. In order to use the PMM approach, first we need to confirm that this method is able to replicate the fluid dynamic behavior of the flow through the FD.

In this chapter, first we show that the geometric characteristics of a FD can be associated to a porous medium (3.2). Second, we demonstrate that the FD can be considered as a flat wire screen (3.3), therefore we can use an empirical correlation (3.3.1) to obtain its pressure drop. From comparing the empirical correlation for the pressure drop with the equation for the porous medium (3.3.2), it can be deduced that FD have a behavior predicted by the porous models in the Reynolds number interval of interest.

Last, we implement (3.4) the PMM and validate our results by showing that the pressure drop obtained with PMM is comparable to the results obtained with IMM, experiments and previous simulations found in the literature (3.4.5).

3.1 GEOMETRY OF A FD

Throughout this work we focus on braided FD devices of uniform wire thickness, such as the commercial devices pipeline embolization device (PED) or Silk, with shared basic

design characteristics. A PED-like device is a self-expandable, cylindrically-shaped device with braided structure. The first generation of the device is comprised of 32 strands made of stainless steel and platinum alloy. Its second generation comprises 48 strands of made of chromium cobalt and platinum. The strands are braided and heat-treated in the expanded configuration with a diameter of 2.5 mm to 5 mm.

On release from the delivery system and when properly positioned at the desired location in the vessel, the implant expands to cover 30 % to 35 % of the neck of the aneurysm. Figure 13 shows a PED deployed in a 3.5 mm diameter model. The plastic artery model has an orifice of approximately 4 mm in length representing the neck of an aneurysm, fitting approximately 66 cells of the stent.

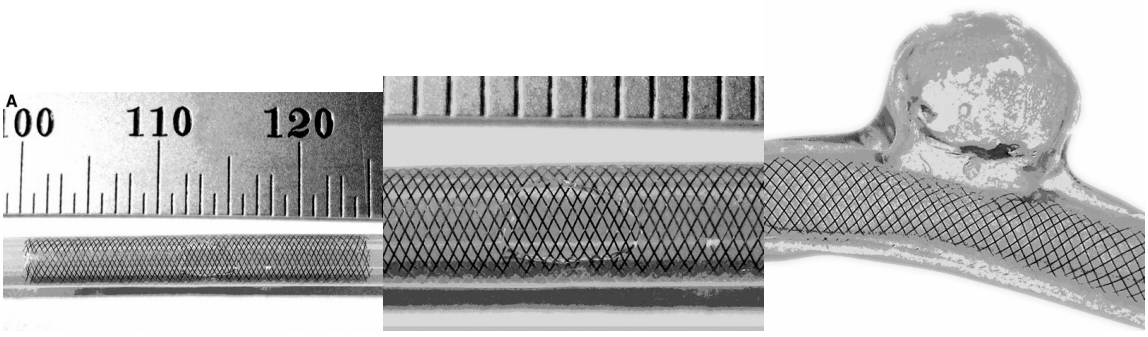

(a) (b) (c)

Figure 13: Photographs of a PED deployed in a plastic model aneurysm. (a) PED deployed in a 3.5 mm diameter plastic model artery. (b) Magnification at the site of the orifice of a model artery showing the coverage of the orifice by the device struts. (c) Lateral view of the PED deployed across the neck of a model aneurysm. Images from [62].

The PED is formed intertwining helical strands with a twill weave (figure 14a), each half in clockwise or counter-clockwise direction. This arrangement defines a cylinder composed of curved cells, which we approximated by rhombuses in this work. The parameters that define the rhombic cell of our model, as shown in figure 14b, are the braiding angle

α, the thickness t of the wire, and L_x, the length of the diagonal perpendicular to the axis of the stent. The length of the diagonal is computed indirectly as a reference FD perimeter divided by the number n_c of cells in the perimeter, $L_x = P_{ref}/n_c = \pi D_{ref}/n_c$ being D_{ref} and n_c parameters of the FD. The number of repeated cells n_c in the perimeter is, in turn, equal to half the number of strands.

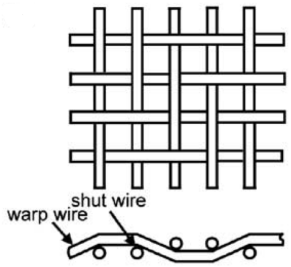

(a) Twill weaving of the strands

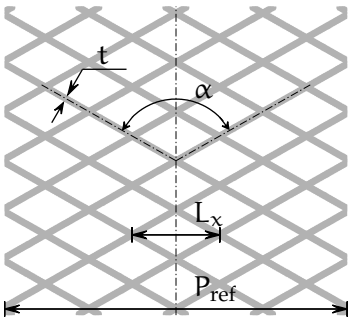

(b) Parameters defining the cell

Figure 14: Geometry of the PED

3.1.1 *Metrics of the FD*

Porosity is a key concept in the theory of wire screens. The orthogonal or cross-sectional porosity β is defined as the ratio of the orthogonally projected open area (A_{open}) of the screen cell to the total cross-sectional area (A_{total}),

$$\beta = \frac{A_{open}}{A_{total}}. \tag{6}$$

A variation of this concept is the volumetric porosity θ. It is defined as the ratio of the connected void volume V_{void} to the total volume V_{total} occupied by the cell of the wire screen,

$$\theta = \frac{V_{void}}{V_{total}}. \tag{7}$$

Another parameter used to characterize the openness of a screen is the *hydraulic diameter*. The hydraulic diameter d_h is a commonly used term when flow in noncircular tubes and channels are calculated. Using this term, it is possible to calculate the parameters for a flow, assuming a round tube. It is defined as four times the ratio of the connected void volume V_{void} to the wetted surface area A_w,

$$d_h = \frac{4V_{void}}{A_w}. \tag{8}$$

Pore density is also used for defining the porous medium. It is defined as the number of pores per unit of area (n/A). It can also be expressed as the inverse of the cross-sectional area of the cell $1/A_c$

The previous metrics are based on the same geometrical properties of the screen and every one of them can be expressed as a function of the others. Researchers studying flow through meshes tend to use volumetric porosity values and Reynolds number based on the hydraulic diameter, while researchers studying FDs tend to characterize them using cross-section porosity and the pore density. However, any combination of these parameters is present in the literature.

Porosity is the most common metric used to quantify the coverage of a device implanted in an artery. Stents, aimed at rigid support of the artery wall, are usually characterized by a high porosity and a low pore density. On the other hand, a low porosity and a high pore density are design goals for FD, which are more flexible and intended for occluding aneurysms with minimal alteration of the parent artery shape.

Given a prescribed treatment for an aneurysm with a low porosity stent, there is a compromise by which the porosity has to be low enough to reduce the inflow to the aneurysm without hindering the flow to perforating arteries.

Furthermore, a high pore density has advantages from the biological perspective, as many cellular processes, like thrombosis, are activated by contact with the FD. FDs also act as a matrix or scaffold that promotes endothelization and parent artery reconstruction.

Porosity alone is not enough to define a flow diverter: it is possible to have two devices with similar porosity and different pore density, which differ in their effect on the flow. Figure 15 shows two endovacular devices of comparable porosity (approximately 80% and 70%) and a different pore density.

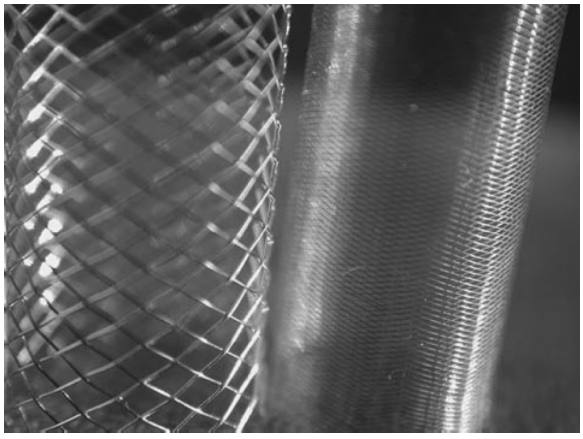

Figure 15: Endovascular devices of comparable porosity and different pore density. Coronary stent, porosity $\approx$ 80% (left) and a flow diverter for IA, porosity $\approx$ 70% (right)

3.2 FLOW DIVERTER AS A POROUS MATERIAL

Our approach to model the wall of a FD is to utilize a porous medium model that recreates its pressure drop. We could consider various classical models for porous media that reproduce at different degree of detail the experimental observations with increasing complexity. The parameters of the porous model can be expressed as a function of the physical properties of the fluid, the geometrical characteristics of the mesh that the model represents, and the fluid dynamic measurements (either simulated or experimental). As a porous material model considers the medium to be homogeneous, we study the validity of the homogeneity assumption for the wall of the FD.

3.2.1 *Porosity models*

Flow in porous media can be divided into four regimes based on their phenomenological behavior: pre-Darcy flow, Darcy flow, Forchheimer flow and turbulent flow. The transitions between these regimes are smooth, which means that it is difficult to determine the regime of the flow in the transition zones. Pre-Darcy flow is governed by molecular effects, and thus is dependent on the individual flow parameters. There is no generally accepted theory for describing this flow regime. Darcy flow, on the other hand, is described by Darcy's law, which is an expression of the conservation of momentum. In the Forchheimer regime, inertial effects have an influence on the flow and a term representing these effects is added to Darcy's equation. In the fully turbulent flow, viscous forces are ignored and the flow is described by statistical methods.

In the following subsections, we briefly present the classical models for porous media, and define basic concepts used in this work.

3.2.1.1 *Darcy's law*

Darcy's law, believed to originate from the work [34], basically states that the flow rate of a fluid in a porous material is proportional to the pressure gradient. For a steady, parallel flow in the x-direction and a filtration velocity u, it may be written in its one-dimensional form as

$$\mu u = \kappa \frac{dp}{dx}, \tag{9}$$

with p being the pressure in the porous medium, κ the permeability coefficient, and μ the dynamic viscosity coefficient.

For a generalization of the equation 9 to three dimensions, we need to denote the velocity in the porous medium as u_i, and we obtain a component i of the pressure gradient in each component of the velocity, as

$$0 = \frac{\partial p}{\partial x_i} - \frac{\mu}{\kappa} u_i, \tag{10}$$

here assuming κ to be the same for each direction.

Darcy's law is valid as long as the Reynolds number Re based on a characteristic grain diameter δ,

$$\mathrm{Re} = \frac{\rho u \delta}{\mu}, \tag{11}$$

is sufficiently low, and the porous medium is fixed and saturated. If the fluid can be considered as incompressible, it is necessary to couple equation 10 with the incompressibility condition

$$\frac{\partial u_i}{\partial x_i} = 0. \tag{12}$$

The Reynolds number for Darcy's flow is assumed to be in the order of $\mathrm{Re} = 10$ as a critical value. Above that critical value, the flow changes its regime and the linearity of the Darcy's model is not longer valid.

There exists also a lower limit of applicability of the Darcy's law. It is due to the fact that factors causing the flow (gravity force or pressure gradient) should be large enough

to overcome adhesion forces [99]. As follows from the ranges of values found in literature, there is no agreement in this respect.

3.2.1.2 *Forchheimer's law*

When Re increases over a certain level, the pressure gradient becomes higher than what is predicted by Darcy's law. Forchheimer [39] linked this issue to kinetic effects and suggested to modify the linear Darcy's law by adding an additive term proportional to ρu^2, representing the kinetic energy. The nonlinear generalization of equations 9 and 10 become

$$0 = \frac{dp}{dx} - \frac{\mu}{\kappa}u - C\rho u^2 \tag{13}$$

and

$$0 = \frac{\partial p}{\partial x_i} - \frac{\mu}{\kappa}u_i - C\rho u_i|u|, \tag{14}$$

where C is the Forchheimer's coefficient. For incompressible flow, we couple the previous equations with equation 12.

There is no general agreement on the nature of the coefficient C for different porous media; in particular, whether it characterizes the medium appropriately. There is a large variety of approaches for computing Forchheimer's coefficient for different porous media, either empirically or depending on the characteristics of the porous medium. Despite the variety, most relationships found in literature can be described with the general formula

$$C = C_1 \kappa^{C_2} \theta^{C_3} \tau^{C_4}, \tag{15}$$

where C_1 to C_4 are constants, θ is the volumetric porosity as in equation 7, and τ is the tortuosity. Tortuosity is defined as the square of the ratio between the direct distance between two points on the flow path of the fluid in a porous medium, and the actual length of the path. Formula 15 is also known as Power-Law model.

Sobiesky et al. [110] review the different models for computing Forchheimer coefficient proposed in the literature, which result in a wide variety of values of the constants for

the Power-Law model. Table 1 reproduces several of these values from which the inconsistency across these models can be inferred.

Table 1: Different formula constants for Power-Law model (equation 15), as reviewed in [110]. Formula number corresponds to the same in the original work. $C_4 = 0$ for all the formulas listed, as formulas involving tortuosity are usually defined for specific flow conditions and it is difficult to asses generality.

FORMULA	C_1	C_2	C_3
2	4.80×10^{12}	1.1760	0.000
3	6.15×10^{10}	1.5500	0.000
4	2.73×10^{10}	1.1045	0.000
5	2.33×10^{10}	1.2000	0.000
6	1.47×10^{7}	0.5500	0.000
8	1.07×10^{12}	1.8800	0.449
9	2.49×10^{11}	1.7900	0.537
10	1.15×10^{6}	1.0000	−1.000
11	1.82×10^{8}	1.2500	−0.750
12	5.50×10^{9}	1.2500	−0.750
13	5.00×10^{-3}	0.5000	−5.500
14	1.15×10^{4}	1.0000	−1.000
15	1.43×10^{-1}	1.0000	−1.500

The identification of a specific transition regime between Darcy and non-Darcy flow models is a subject of current research. It is generally assumed that the upper limit of

Darcy's law coincides with the lower limit of applicability range for the Forchheimer's law. The upper limit of the Forchheimer's law is due to the onset of turbulence. Following [46], it is close to $Re \approx 80$. Above $Re \approx 120$, the flow is fully turbulent and must be described with different laws.

3.2.1.3 *Anisotropic Darcy model*

When the medium is not isotropic, the change in pressure with the velocity depends on the direction of the flow, and the models discussed previously are not longer accurate. There are many examples of porous media with strong anisotropic characteristics. To represent this behavior, the models need to be modified accordingly. Particularly, the permeability constant κ in equation 10 needs to be replaced by a permeability tensor $\mathcal{K}_{ij}$. The modified Darcy equation can be written as

$$\mathcal{K}_{ij}\frac{\partial p}{\partial x_j} = \mu u_i. \tag{16}$$

The precise form for $\mathcal{K}_{ij}$ depends on the structure of the underlying solid matrix in the porous medium. As a specific example, when the permeability differs for each of the three directions, the tensor $\mathcal{K}$ is expressed as

$$\mathcal{K} = \begin{pmatrix} \kappa_1 & 0 & 0 \\ 0 & \kappa_2 & 0 \\ 0 & 0 & \kappa_3 \end{pmatrix} \tag{17}$$

For more complex cases, permeability cannot be represented as a diagonal matrix, and this severely complicates the analysis and the numerical calculations.

3.2.2 *Approximation of FD wall to an homogeneous medium*

Modeling of the FD wall as a homogeneous porous material implies that the FD is also represented as homogeneous material. In real cases, when the cells are in contact with

the neck of the aneurysm, the pressure drop is produced not only by the flow traversing the cell, but also by the contact with the wall of the neck of the aneurysm. When the area of the cell is small compared to the orifice of the neck, more whole cells fit in the orifice. The ratio of the area covered by whole cells to the total area increases, leading to a best approximation of the assumption of homogeneity.

We ran a series of simulations to estimate the number of cells necessary to comply with the assumption of homogeneous material according to the procedure as follows. First, we considered a circular cylinder with a diameter of 0.1 cm, and we placed a flat wire mesh in the cross section of the cylinder, at the middle of its axis. Second, an unstructured volumetric mesh was generated and it was adaptively refined around the wires with 6 levels of refinement, obtaining base elements sizes from 2×10^{-2} cm to 3.125×10^{-4} cm around the wires. Figure 16 shows the mesh of the boundary of the domain and in the cross-sectional plane of the wires. Slip condition was prescribed to the wall of the domain, and a non-slip condition to the surface of the wire. Uniform velocity profile was imposed at the inlet. We imposed traction-free boundary condition and set the pressure to $p = 0$ at the outlet. The value of pressure drop was directly read at the inlet.

In successive simulations, we increased the diameter of the cylinder, so as to include more whole cells in the inner section. Figure 17 shows the cells included in each simulation. We kept the pore density and the Reynolds number constant during the series and computed the pressure drop across the screen for each run.

To compare these values, we computed the relative difference in the pressure drop for the homogeneous medium, obtained with the geometrical model and boundary conditions detailed in later in section 3.4.3.

In figure 18 we compare the relative differences in pressure drop for two cases of identical pore density but different porosity value. From the results of this study (figure 18) we determined that in a cross-section of area equivalent to the area of 24 cells, the border effect of the domain is reduced enough so that the wire screen can be considered as an homogeneous medium within an error of 2%. This value is equivalent to a pore density of

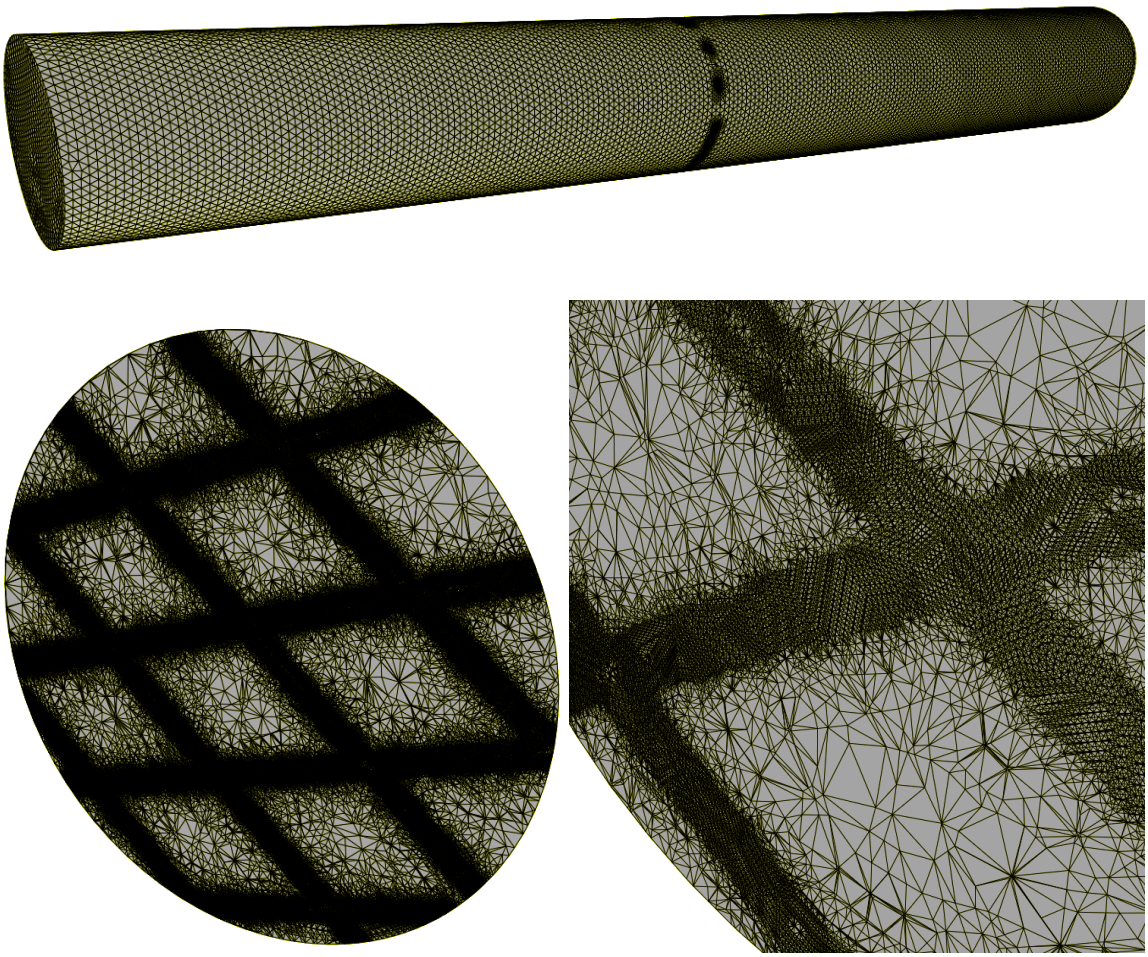

Figure 16: Meshes of the boundary and the cross-sectional area of the domain corresponding to 12-cell case.

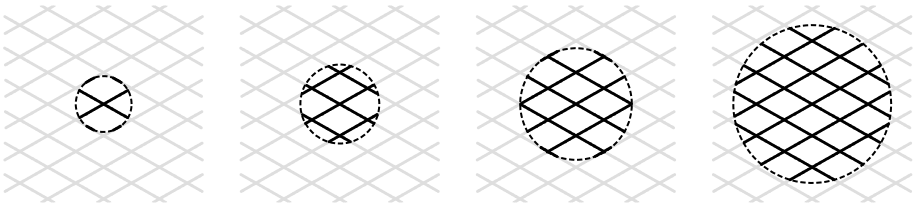

Figure 17: Successive cylindrical domains to study the influence of the border in the pressure drop. The cross section area of the domain is equivalent to the area of approximately 3, 6, 12, and 24 cells.

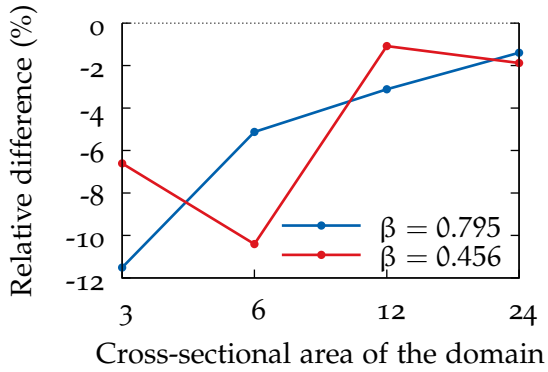

Figure 18: Relative difference between the pressure drop of the homogeneous medium and the cases of circular cross-sectional domain area equivalent to 3, 6, 12, and 24 cells, for two different porosity values β.

approximately 200 $1/cm^2$, a number that is easily exceeded by typical neck sizes and FD, where the quantity of pores is in the order of the thousands. Therefore, we can assume that all the cases studied in this work can be represented by an homogeneous medium.

3.3 FLOW DIVERTER AS A FLAT WIRE SCREEN

To evaluate the effects of the FD in the flow across its section, we associated the wall of the FD to an infinitely large flat screen. Fluid flow through screens is present in a number of technical areas, and several experimental studies have been carried out in the past to model and correlate the characteristics of general purpose screens. In this section we use an experimental correlation to validate our simulations of the wire screen that represents the FD. In the following section, we also used this experimental correlation to define the parameters for our porous model of the FD.

3.3.1 *Pressure drop through a wire mesh*

A screen may be thought of as any distributed resistance that effects a reduction in pressure and, for higher Reynolds numbers, a change in flow direction. The use of wire screens is customary in many fields including filtering, mining and mineral processing, porous beds. One of the most common purposes of wire screens is to improve uniformity in duct flow due to their capacity to reduce turbulent length scales and intensity. Several experimental studies have been carried out earlier to generate these flow characteristics for general purpose screens. The approaches found in the literature for modeling the pressure drop through a wire mesh range from mathematical models to empirical models based only on measurements.

The flow resistance of a porous medium is generally characterized by three different regimes: a region of low Reynolds number where the pressure drop Δp through the screen is proportional to $1/Re$, a region of high Reynolds number where Δp is independent of Re, and an intermediate region of transition between the previous two. Even though there are several models proposed during the years, most of them are focused on moderately high Reynolds numbers and high Mach numbers. Furthermore, their predictions are usually not satisfactory [87].

For the specific case of incompressible flow (Mach = 0), there has been numerous attempts to obtain models that correlate, in a single relation, both the pressure drop and the Reynolds number. As in the case of compressible flow, most of the measurements and the models lie in the range of the moderately high Reynolds numbers.

The performance of a wire screen for a flow in a duct is usually measured in terms of the irreversible pressure drop, defined as:

$$\Delta p = \frac{1}{2} K \rho u^2, \tag{18}$$

being K a pressure drop multiplier or *pressure loss coefficient*, ρ the fluid density and u the approach flow velocity upstream of the screen.

From steady flow correlation at low and intermediate Re, the equation for K generally takes the form [87, 134]

$$K = \frac{a_1}{Re} + a_2. \tag{19}$$

In [125], the authors compared different pressure drop correlations and pointed out that the pressure drop caused by the flow through an array of wires is mainly affected by two mechanisms: the resistance form (a2) and the surface friction (a1). This means that the correlation form shown in equation 18 implies creeping-viscous-dominated Darcy flow for low Re, where a_1/Re dominates, smoothly transitioning to turbulence-like flow at high Re, where a_2 dominates.

The pressure drop across a clean unclogged, thin, plain, square-type circular metal wire screen can be calculated using the irreversible pressure drop multiplier obtained from the correlation by Idelchik [52] for the low-Re regime:

$$K = \frac{22}{Re_h} + 1.3\,(1-\beta) + \left(\frac{1}{\beta} - 1\right)^2 \qquad \text{for } Re_h < 50, \tag{20}$$

where the characteristic length for Re is the hydraulic diameter d_h:

$$Re_h = \frac{\rho u d_h}{\mu}. \tag{21}$$

The reported validity range of equation 20 is for $Re_h < 50$. Even though most of the cases of FD in aneurysm we study fall within this range, for cases with $Re_h > 50$ we compare their Δp with the correlation for the intermediate Re region, also reported by Idelchik [52]:

$$K = k'_{Re_h}\left(1.3\,(1-\beta) + \left(\frac{1}{\beta} - 1\right)^2\right) \qquad \text{for } 50 < Re_h < 1000 \tag{22}$$

The multiplier k'_{Re_h} in equation 22 depends on Re_h. Its data points from reference [52] and a fitting exponential curve are shown in figure 19.

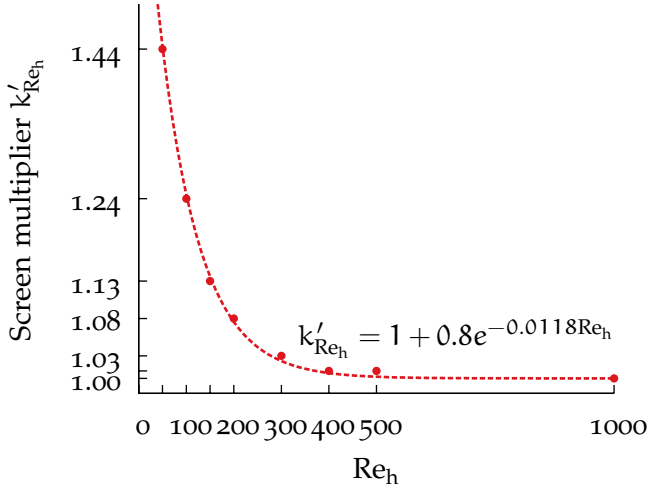

Figure 19: Screen multiplier k'_{Re_h} in equation 22

3.3.2 *Wire screens follow Forchheimer's law*

The description of the flow through a wire screen, as implied by the correlations for Δp, coincides with the observations of the flow through a porous medium, as described previously in section 3.2.1.

We can see this relationship by combining the expression for Δp (equation 18) with the general form of correlation for K (equation 19) we obtain

$$\Delta p = \frac{1}{2}\left(\frac{a_1}{Re} + a_2\right)\rho u^2. \tag{23}$$

Replacing with $Re = \frac{\rho u d}{\mu}$ for a general characteristic length d, we obtain

$$\Delta p = \frac{a_1 \mu}{2d}u + \frac{1}{2}a_2 \rho u^2. \tag{24}$$

We find that from the formula for the experimental correlation of K for low Re_h (equation 20) we can recover Forchheimer's law (equation 13), i. e. a quadratic dependence of Δp with velocity u for wire screens, in their validity intervals of Re.

This is also noted in [38], where the authors conclude that even though there is no direct proof in the literature, from the analysis of the available data in the literature, Forchheimer relation effectively can be applied to wire screens.

3.4 IMPLEMENTATION OF THE PMM

As presented previously, the influence of the inertial effects in the range of geometrical characteristics and the Reynolds numbers involved in the FDs represented by this work, cannot be neglected in the implementation of a PMM.

We updated the Darcy model originally incorporated in the in-house solver FEFLO (a description of the schemes used in the simulations can be found in section 2.2.3) with the inertial term of the Forchheimer law. The implementation of PMM adds a source of mass forces term S to the right hand side of the momentum balance equation. The source term is expressed as

$$S = Du + Fu^2, \tag{25}$$

and has functional form of the Forchheimer's law, with the local velocity u in the linear and quadratic terms. The porosity parameters D and F are constant on the the region where applied. This source also represent Darcy's law by setting $F = 0$.

The definition of a porous region (PR) can be done in two ways. One option is using a body-fitted (BF) definition, in which the porous properties are associated to a region originally defined in the geometrical description of the domain. This approach is not as flexible as usually required for the general geometry of an aneurysm. For this reason, we added the option to define a PR by using an immersed body (IB), which is used to label the elements that belong to the PR. The implications of each method are discussed and compared in more detail later on this section (subsection 3.4.6).

Finally, the value for the parameters D and F have to be passed to the solver. The value of the parameters can be determined

1. by an empirical model of the parameters based on fundamental characterizations of the porous medium,
2. from the results of simulations or experiments for a particular case, or
3. from correlation curves, usually obtained from series of experiments and covering a range of flow conditions.

As shown in section 3.2.1.2, the empirical approach for the Forchheimer coefficient C offers inconsistent results with the different formulas found in the literature, which "makes any interpretation impossible" and represents the "lack of agreement about the character of Forchheimer coefficient" [110]. The computation of the porous parameters by the other two methods are obtained by approximating the source S to the pressure gradient ∇p, which is computed as discussed in the following sections.

3.4.1 *Porous parameters computed from simulations*

The Δp vs. u relationship for a flow through a wire screen can be represented (sec 3.3.2) by a quadratic curve $\Delta p = Bu + Au^2$. That curve is obtained by measuring or simulating the pressure drop Δp for a series of velocities u. The coefficients A and B are calculated from the quadratic curve that fits the measurement points.

Combining A and B with the Forchheimer model (equation 13), and considering

$$\Delta p \approx \frac{dp}{dx}\Delta L, \tag{26}$$

being ΔL the width of the porous region where Δp occurs, we obtain the values for the permeability

$$\kappa = \frac{\mu_0 \Delta L}{B}, \tag{27}$$

and the Forchheimer coefficient

$$C = \frac{A}{\rho_0 \Delta L}, \tag{28}$$

where the subindex $_0$ refers to the properties of the fluid during the measurements or simulations.

In this way, the parameters of the porous model can be expressed as function of the physical properties of the fluid, the geometrical characteristics of the mesh that the model represents, and from the fluid dynamic measurements.

Plugging the approximations of κ and C (equations 27 and 28) back in 13, we obtain the expression for the pressure gradient

$$\frac{dp}{dx} = \frac{\mu}{\mu_0}\frac{B}{\Delta L}u + \frac{\rho}{\rho_0}\frac{A}{\Delta L}u^2, \tag{29}$$

associating the source term in the solver, $S = Du + Fu^2$, to the pressure gradient, the parameters for porous model are computed as

$$D = \frac{\mu}{\mu_0}\frac{B}{\Delta L}, \tag{30}$$

$$F = \frac{\rho}{\rho_0}\frac{A}{\Delta L}. \tag{31}$$

3.4.2 *Porous parameters computed from experimental correlations*

From the correlation for Δp considered in this work (equation 20), we obtain the values for the general coefficients

$$a_1 = 22, \tag{32}$$

$$a_2 = 1.3\,(1-\beta) + \left(\frac{1}{\beta} - 1\right)^2, \tag{33}$$

and use the hydraulic diameter d_h as the characteristic length for the Reynolds number. We replace these values in the expression for Δp as a function of the coefficients of the empirical correlation (equation 24)

$$\Delta p = \frac{a_1\mu}{2d}u + \frac{a_2\rho}{2}u^2.$$

Assuming

$$\frac{\Delta p}{\Delta L} \approx \frac{dp}{dx},$$

we obtain the expression of the Forchheimer's law based on the empirical correlation for Δp:

$$\frac{dp}{dx} = \frac{11\mu}{d_h \Delta L} u + \frac{\rho}{2\Delta L}\left(1.3\,(1-\beta) + \left(\frac{1}{\beta} - 1\right)^2\right) u^2. \tag{34}$$

By comparison with the source term in the solver, $S = Du + Fu^2$, the parameters for the model are

$$D = \frac{11\mu}{d_h \Delta L}, \tag{35}$$

$$F = \frac{\rho}{2\Delta L}\left(1.3\,(1-\beta) + \left(\frac{1}{\beta} - 1\right)^2\right). \tag{36}$$

3.4.3 *Simulation of flat wire screen using IMM*

We simulated flow through the FD mesh and computed the pressure loss coefficients for different Re, in order to later compare the K values with the empirical formula for K.

We used the parameters of the Screen W used by [64] in their study, which has a geometry similar to the PED design considered in this work. We compared our results to their CFD solutions for consistency.

The simulated screen corresponds to a PED FD with a diameter $D = 5\,\text{mm}$, 16 wires, a braiding angle $\alpha = 116°$ and a wire diameter $t = 100\,\mu\text{m}$. It presents a porosity $\beta = 0.817$ and an hydraulic diameter $d_h = 5.96 \times 10^{-4}\,\text{m}$.

The computational domain consist in a long rectangular cylinder. The geometrical model representing the wires of one cell was placed on the cross-section at the middle of the cylinder axis. An unstructured volumetric grid was generated by using an advancing front method and a base element size of $0.02\,\text{cm}$. The mesh was adaptively refined around the screen wire by using an unstructured grid IMMs with 4 levels of mesh adaptation. Uniform velocity profile was prescribed as boundary conditions at the inlet, pressure boundary condition with $p = 0$ was prescribed at the outlet, symmetry boundary condi-

tions were applied at the domain wall, and a non-slip condition at the surface of the wire. We run simulations with Re values from 1 to 100.

In figure 20 we show the arrangement of the domain and the screen wires at the middle of the cylinder, and the discretization of the boundary and in the cross-sectional plane of the wires. [1] We also show pressure and velocity distribution for the case Re = 6.85.

The whole set of results, as well as a comparison with previous results found in the literature and the experimental correlation is shown in figure 22 in section 3.4.5. We find that the results are in agreement with both, the experimental results and the simulations by other authors. In the same figure, we also compare the results of the same case simulated using PMM, as discussed in section 3.4.4.

3.4.4 *Simulation of flat wire screen using PMM*

For testing the PMM, we computed the pressure drop of the same wire screen described and simulated in section 3.4.3 using the IMM method.

The computational domain is a long cylinder, with an PR as a cylindrical sector of thickness 0.02 cm at the middle of the axis. It was defined using the BF definition. The element size varies from 0.02 cm outside of the PR to 0.005 cm (equivalent to two levels of mesh adaptation) inside of the region. The boundary conditions used are the same as in the IMM simulation, i. e. uniform velocity profile at the inlet and $p = 0$ prescribed at the outlet.

For the computation of the parameters of the model, we used the analytical expression derived in section 3.4.2 (equation 35 and 36), that considers the correlation of K represented in equation 20. The input values were $\beta = 0.817$, $d_h = 5.69 \times 10^{-2}$ cm, $\mu = 0.033$ Poise, $\rho = 1\,gr/cm^3$ and $\Delta L = 0.02$ cm. The coefficients for the PMM are $D = 339.23$ and $F = 7.20$ (expressed in cgs units).

1 Symmetry is exploited in the simulation but not in the figure for visualization purposes.

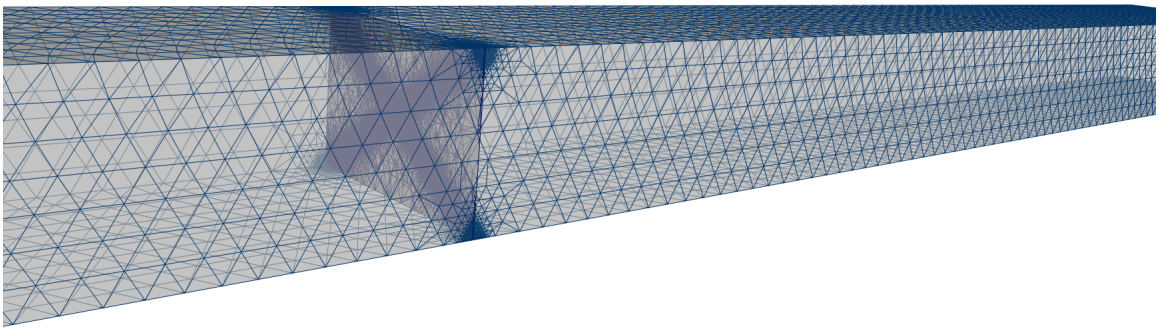

(a) Unstructured grid of boundary and cross-section plane of the wire

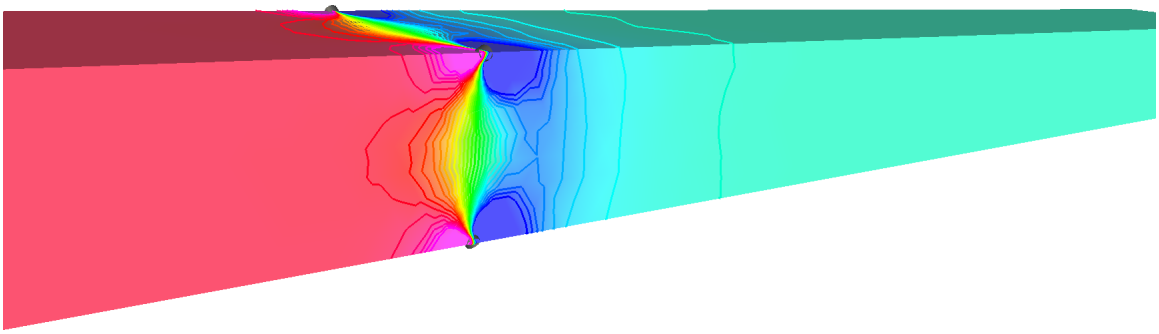

(b) Pressure distribution ($-100\,\mathrm{dyne/cm^2}$ to $300\,\mathrm{dyne/cm^2}$)

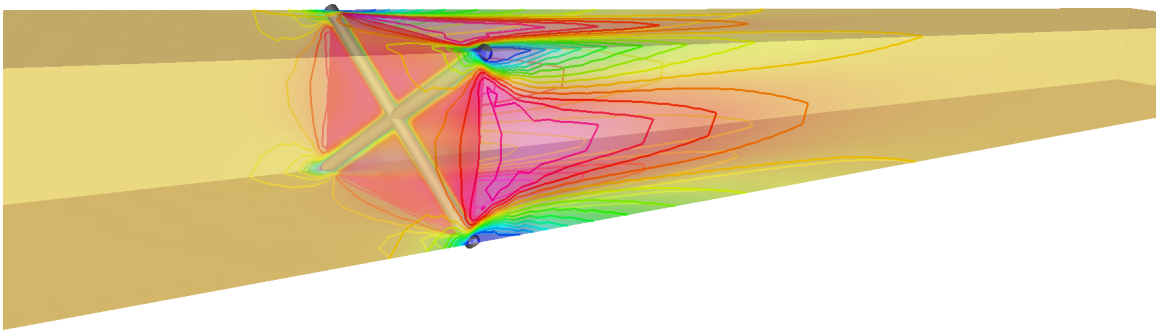

(c) Velocity ($0\,34\mathrm{cm/s}$)

Figure 20: Boundary grid and solution for the simulation of a screen cell using the IMM method, for the simulation corresponding to Re = 6.85

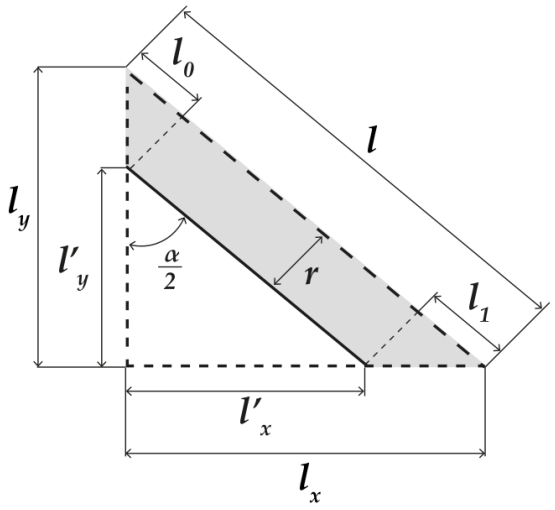

Figure 21: Scheme of a PED cell

The values of β and d_h are computed using the geometric magnitudes shown in the scheme of the PED cell in figure 21 and calculated as:

$$l_x = \frac{L_x}{2} = \frac{P}{2n_c} \tag{37}$$

$$l_y = \frac{lx}{\tan\frac{\alpha}{2}} \tag{38}$$

$$l'_x = l_x - \frac{r}{\cos\frac{\alpha}{2}} \tag{39}$$

$$l'_y = l_y - \frac{r}{\sin\frac{\alpha}{2}} \tag{40}$$

$$l = \sqrt{l_x^2 + l_y^2} \tag{41}$$

$$l_0 = r\cot\frac{\alpha}{2} \tag{42}$$

$$l_1 = r\tan\frac{\alpha}{2} \tag{43}$$

being $r = t/2$. t, α, L_x, n_c, and P_{ref} are defined in section 3.1. The porosity β and the hydraulic diameter d_h are computed as

$$\beta = \frac{A_{open}}{A_{total}} = \frac{l'_x l'_y}{l_x l_y} \tag{44}$$

$$d_h = \frac{4V_{void}}{A_w} \tag{45}$$

V_{void} and A_w can be approximated by

$$V_{void} = l_x l_y r - \frac{\pi r^2}{2}\left(l + \frac{1}{2}l_0 + \frac{1}{2}l_1\right). \tag{46}$$

and

$$A_w = \pi r\left(l + \frac{1}{2}l_0 + \frac{1}{2}l_1\right) \tag{47}$$

.

As a comparison, we also computed D and F based on the coefficients A and B obtained from the IMM simulations. We fitted a quadratic curve using LSM from the values of Δp and u and computed the porosity coefficient as explained in section 3.4.1. Using this method, the values obtained were $D = 351.52$ and $F = 9.95$, which are very close to the values obtained using the previous method.

The results fit the values of K obtained by the empirical correlation and the computational simulations. The pressure loss coefficients obtained are shown and compared in figure 22 in the next section (3.4.5).

3.4.5 *Comparison of the pressure loss of the wire screen using IMM and PMM*

The figure 22 compares values of K from the experimental correlation described in section 3.3.1), the results from the IMM simulation (section 3.4.3), the results from the PMM simulation (section 3.4.4) with parameters computed from the empirical correlation, and the CFD simulation by Kim et al [64], for different values of Re_h.

The second scale on the top axis shows the equivalent values of the Reynolds number Re based on the wire diameter t, in comparison with the Reynolds number Re_h based

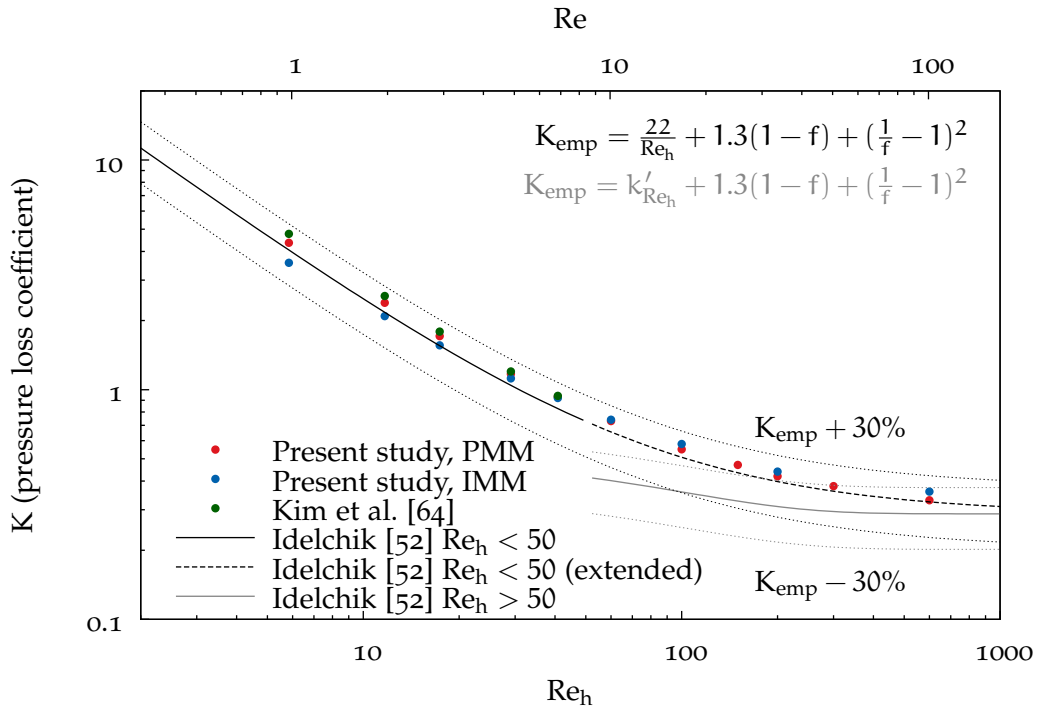

Figure 22: Comparison of PMM results with experimental and other simulations data

on the hydraulic diameter d_h used by the empirical correlation. We added curves (dotted lines) representing an upper and a lower bound of ±30% of the empirical curve, as an estimation of the variability of the experimental data. [2]

The plot shows that the results for the simulations present a general consistency between the different methods, and that are well fitted by the experimental correlation for low Re (equation 20). The dashed line represents this correlation for low values of Re, extended to the intermediate Re region. The empirical correlation also seems to fit well the results of the simulations beyond its reported validity region ($Re_h < 50$).

2 As we do not count with information about the deviation of the original experimental measurements, we take the typical value of ±30% usually found in similar works of empirical correlations for wire screens [140], granular beds [37] and foam matrixes [70].

The empirical correlation for intermediate Re values (equation 22) for the interval of $50 < \mathrm{Re_h} < 1000$, on the other hand, does not represent well the results for the simulation, particularly in the transition region from the low-Re regime, $50 < \mathrm{Re_h} < 200$. In fact, although both correlations come from the same source [52], they barely overlap with each other at $\mathrm{Re_h} = 50$, when considering the dispersion boundaries of 30%.

Considering our studies of FD in aneurysms, with typical physiological values, we estimate that the highest Re (based in wire diameter) usually is around Re = 20, hardly exceeding 60, but still falling in the transition zone between low and intermediate Re. We find that this range is well represented by the empirical curve in equation 20, even though some of the results lie outside its reported validity interval.

The typical values of pore density for FDs in this Re range vary from approximately $750\,1/\mathrm{cm}^2$ to $3500\,1/\mathrm{cm}^2$, which is above the limit of $200\,1/\mathrm{cm}^2$ estimated in section 3.2.2 for representing FDs as a porous medium.

There may be devices with a low pore density, e. g. coronary stents, within this range. For these cases, when using PMM the border effect becomes an increasing source of uncertainty as the pore density decreases. However, these devices are out of the scope of this work.

The fact that we can represent our interval of interest with only one correlation simplifies the implementation of the porous model, as there is no need to change the formulas for the computation of the parameters depending on the Reynolds number.

3.4.6 *Definition of PR*

The definition of the PR, i. e. the region whose elements are attributed properties of porous material, can be done in two ways.

The first option is a body-fitted (BF) approach, in which the porous properties are associated to the elements that belong to a region originally defined in the geometrical description of the domain. This approach has the advantage that it uses the same de-

scription of the geometry used by the grid generator, and the faces of the elements are generated on the interface of the PR, fitting the boundary of region.

The second option is a immersed body (IB) approach. A body that represents the PR is immersed in the domain, and is used for selecting the elements in contact with it. The body is represented by the volume defined by an arbitrary surface and a distance e to each side of this surface. Using the IB definition, the faces of the elements belonging to the PR are not necessarily parallel to the defined PR boundary, instead they define a different effective interface formed by the connected external faces of the elements in the PR.

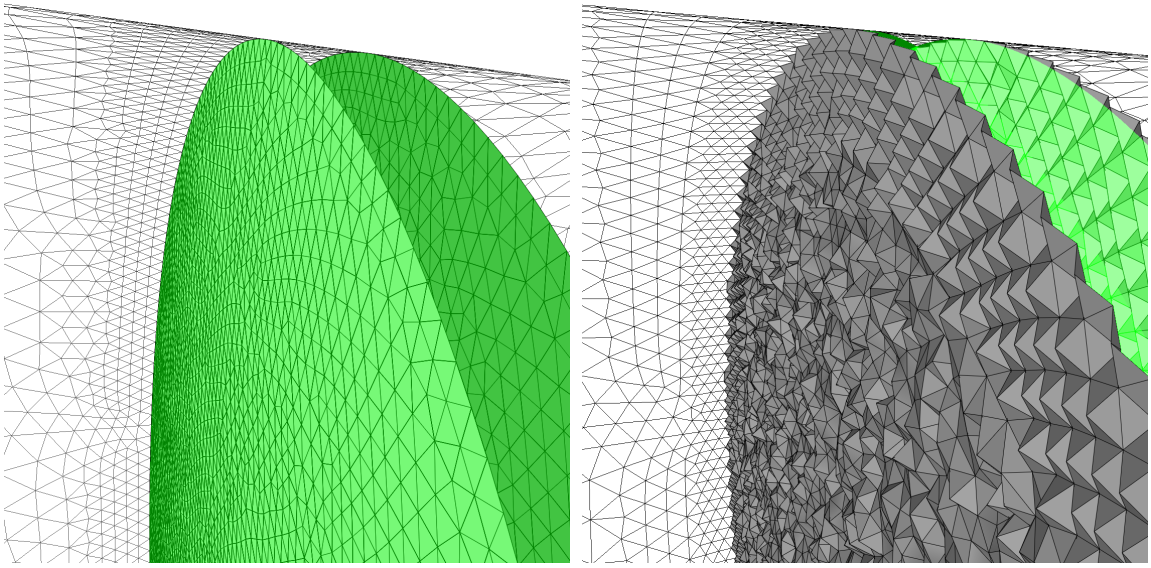

(a) BF definition (b) IB definition

Figure 23: Interface between the regions, obtained using BF and IB definitions, formed by the faces of the elements of the PR. In the case of IB, the interface approximates, but not necessarily coincides, with required boundary (green plane).

Figure 23 shows the interface between regions using both definitions. Because the numerical scheme of each method is different, the results of a simulation that considers a certain region vary according to the method used.

The advantage of the IB definition is that it is a very flexible method for defining a region, and refining the grid is only constrained to precision requirements.

In contrast, the definition of the geometry of the PR with the BF approach requires a watertight assembly of analytical and/or discrete surface patches to describe the interface of the PR. The creation of such a watertight geometrical model can be challenging even for simple vascular geometries, with no guarantees that the mesh generator is able to mesh the domain. This is the main reason that motivated the implementation of the IB approach for its use with the PMM in the solver.

We observe that in general, when using the IB approach there is an overprediction of the pressure drop over the expected results. The exact value of this difference depends on the specific conditions of the simulation. Currently, the only viable choice to define a PR in the geometry of an aneurysm is to use the IB approach, and to characterize the difference in the results using test runs with working conditions similar to the aneurysm simulation. From these test runs we obtain two different set of coefficients A and B of the quadratic curves Δp vs. u. By using the expression of the parameters D and F as a function of A and B (equations 30 and 31), we are able to relate the porous parameters obtained by each PR definition.

Using the specific values for our cases as an example, we found in previous tests that good specification values for the PR in our aneurysm simulations are a width $2e = 0.02\,\text{cm}$ and an element size of $5 \times 10^{-3}\,\text{cm}$. With those conditions applied to test runs, we find that using the IB approach there is an overprediction of Δp, that translates into an increase for D and F of $25 \pm 3\%$ and $16 \pm 3\%$, respectively, over their values originally computed. Based on those values, we used a corrected version of the parameters of $D_{corr} = 0.75D$ and $F_{corr} = 0.86F$, to compensate for the expected difference in the results.

The methodology to compute the parameters for PMM from the experimental correlation of K can be summarized in the following five steps. The examples and deductions in this work are based on a PED-like flow diverter; however, these steps are extensible to other device designs.

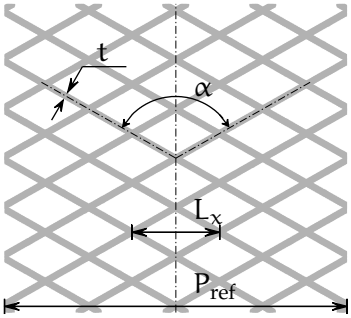

1) Define a set of geometrical parameters that define the cell, i. e. the braiding angle α, the wire width t, and the length L_x of the cell.

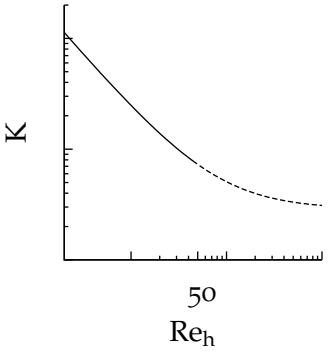

2) Select of the empirical correlation (equation 19) that represent the device design.

$$K = \frac{a_1}{Re} + a_2$$

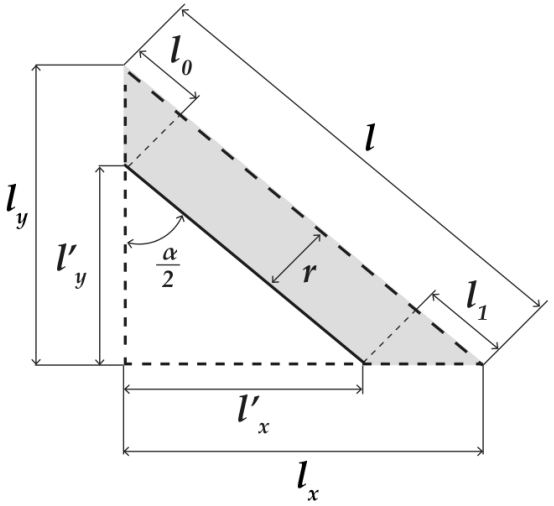

3) β and d_h are computed from the parameters of the cell, equations 37 - 43, 46, 47.

$$\beta = \frac{A_{open}}{A_{total}} = \frac{l'_x l'_y}{l_x l_y}$$

$$d_h = \frac{4V_{void}}{A_w}$$

$$D = \frac{a_1 \mu}{2 d_h \Delta L}$$

$$F = \frac{a_2 \rho}{2 \Delta L}$$

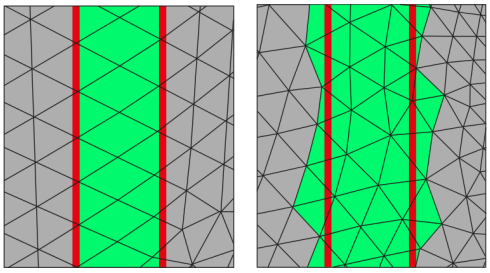

4) Parameters D and F for the porous model $S = Du + Fu^2$, obtained from equations 35 and 36.

5) Compensate for the expected difference in the results by defining the PR by IB instead of BF.

$$D_{corr} = c_D D$$

$$F_{corr} = c_F F$$

In the case of not counting with an experimental correlation that represents the design of interest, the workflow for obtaining the parameters of the porous model is as follows:

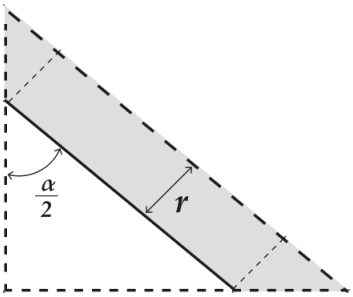

1) Model and simulate the cell of the design of interest.

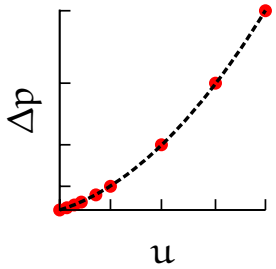

2) Obtaine the curve Δp vs. u and compute its parameters A and B.

$$D = \frac{\mu}{\mu_0} \frac{B}{\Delta L}$$

$$F = \frac{\rho}{\rho_0} \frac{A}{\Delta L}$$

3) Compute parameters D and F for the porous model $S = Du + Fu^2$ from equations 30 and 31.

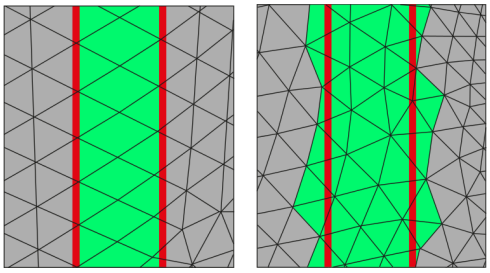

4) Compensate for the expected difference in the results by defining the PR by IB instead of BF.

$$D_{corr} = c_D D$$

$$F_{corr} = c_F F$$

FD AS POROUS MEDIUM IN P-S ANEURYSMS

In this chapter, we apply the PMM method, explained in the previous chapter, to simulate different cases of FD in P-S aneurysm models. First, we describe the methodology (4.1) used to generate a suitable computational model (4.2) for the PMM simulations. In section 4.3 we show the results of the simulation of six FD and three different P-S aneurysm models, at different instants of the cardiac cycle. We compare the PMM results with the results of equivalent simulations using IMM [77].

4.1 METHODOLOGY

The methodology for obtaining the PR for the simulation of P-S aneurysm by using PMM can be divided into three stages:

1. deployment of the FD in the vessel wall
2. generation of the surface for the PR, and
3. refining the mesh around the PR, as needed.

4.1.1 *FD deployment in the vessel wall*

The deployment of the FD is done in four steps which include 1) the extraction of the centerline of the parent vessel, 2) an initial cylindrical host surface generation, 3) the adaptation of this surface to the vessel wall, and 4) optionally, mapping a stent design on the generated surface [78].

The skeleton of the parent vessel is extracted from the vascular model using a previously developed algorithm [26]. A cylindrical support surface is then generated along this

skeleton. Assuming this surface is elastic, it is deformed under the influence of internal smoothing forces and external attractive forces to the vessel wall. This deformation process is interactively stopped when most of the points on the cylindrical surface are on the vessel wall.

Once the final cylindrical surface is obtained, it is possible to get the mean value of the diameter in the neck of the aneurysm, which is necessary in order to later compute the porosity parameters. An optional step is to map a the FD design onto it the cylindrical surface, as explained in [5]. This last step is only necessary in order to compute the variation of the porosity of the FD due to the effect of curvature and foreshortening.

4.1.2 *Generation of the PR*

The generation of the PR requires a cylindrical surface that realistically represents a deployed FD, as explained in the previous subsection 4.1.1). The following step is the generation of the patches that are used for the definition of the PR using the IB approach (section 3.4.6).

The aim of this procedure (represented in figure 24) is to remove from the cylindrical surface the regions that are in contact with the wall. If not removed, this volume will create a porous lining in the artery, reducing its effective diameter, effect that is not observed in the IMM simulations.

The cylindrical surface (figure 24a) is expanded by moving the points of its surface a small distance in the direction of the normal of its elements (figure 24b). Once it is expanded, the intersection between the cylinder and the domain grid is computed (figure 24c, 24d). The resulting patches are then contracted the same distance used for the expansion of the cylinder (figure 24e).

The patches should cover the main regions, which usually include: the neck region, the entrance to perforating arteries, and any bleb in the artery big enough for fluid to flow between the walls of the FD and the artery. The distance used to expand and contract the

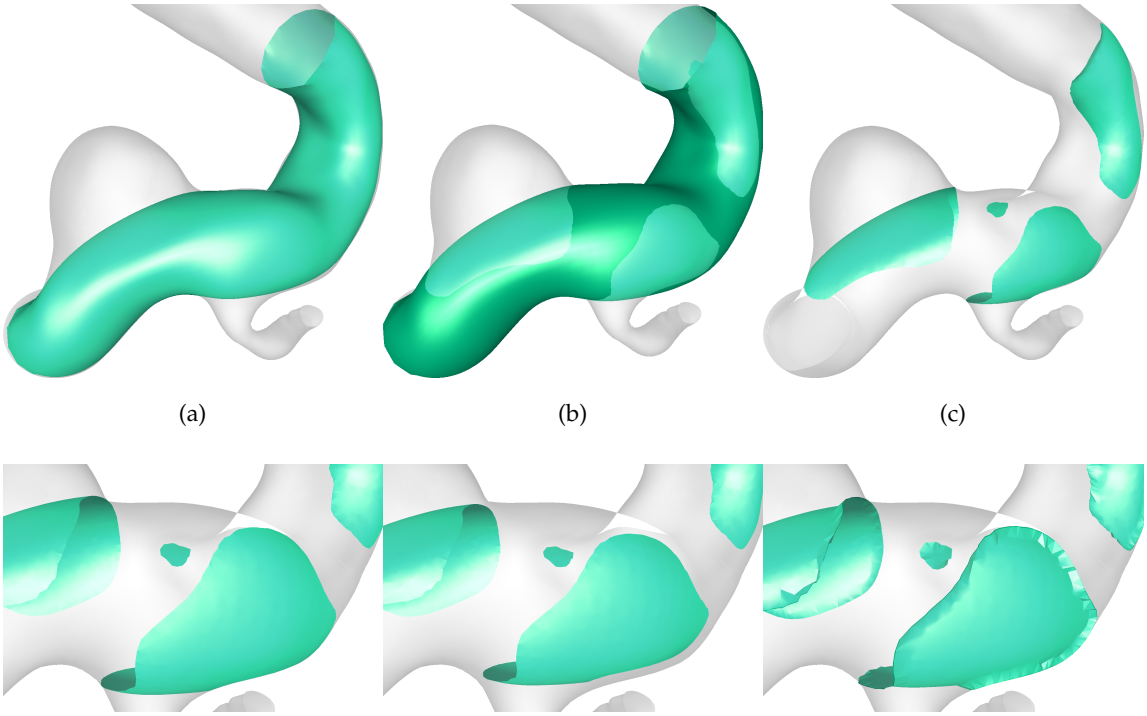

(a) (b) (c)

(d) (e) (f)

Figure 24: Obtaining the patches that define the PR: (a) The cylindrical surface is deployed inside the vessel until it encounters the wall of the artery. (b) The surface is expanded until the region in contact with the wall becomes external to the domain. (c, d) The intersecting region between the surface and the domain is computed, optimized and (e) contracted. Finally, (f) the edge is moved to meet the boundary of the domain in order to close the gap resulting from the previous step.

patches has to be chosen as the minimal distance that allows a clean cut to the cylindrical surface. In this example, the moving distance is 0.015 cm.

At this point, it may be necessary a step of optimization of the elements of the surfaces, as the intersection algorithm does not guarantee well-shaped surface elements.

Because the cut was done in an expanded configuration, there will be a gap between the surface edge and the wall of the domain. This gap has to closed to avoid any flow through it. We close this gap by moving the points of the edge in the direction perpendicular to the closest element of the domain boundary (figure 24f).

4.1.3 *Refining the mesh*

The patches obtained in the previous step can be used to define smaller elements in their surrounding region, where the porosity computations will be done. The patches are used as refinement surfaces in an adaptively refinement step or as background size sources for the mesh generator. We add the patches as background size sources to any previously existing source in the original geometry description.

Using the background sources, we differentiate three regions for the size of the elements: a) a refined elements region that covers the PR, b) a transition region, where the size of the elements changes linearly from the refined region to the base region, c) base region, which covers the rest of the model, and where the elements have the original basal size.

The choice of the value for those parameters is subject to the constrain of getting the thinnest PR that contains enough elements to provide a good representation of the Δp, while keeping the global number of elements of the domain as low as possible. To find the optimal values that satisfy those constrains, we carry out a series of test runs in cylinders first and in aneurysm geometries later.

No optimal values were found to fit all cases. Instead, we could determine criteria for these values. Because we are trying to emulate the behavior of a porous "interface" with

a porous volume, the PR can not be much thicker than the size of a basal element, to avoid perturbation in the flow pattern. On the other hand, the solver requires on the order of four elements to apply a given pressure drop inside the PR, for which two levels of refinement are necessary. It is possible to achieve similar level of precision with only one level of refinement at the cost of an increase of the PR width. However, the savings in elements does not often compensate the drawbacks of a thicker region.

In this work the width of the transition region is half the width of the refined region. We believe that the variation of its width can affect the overpressure effect associated to IB method for the definition of the PR, by smoothing the PR interface. Further studies are needed on how the size of the transition region can affect the precision.

For the resizing of the elements, the criteria mentioned above prescribe the use background sources instead of adaptive refinement, for which the size of the source remains as a parameter to regulate the size of mesh at the expense of precision.

For the simulation in this work we chose a set of conservative parameters which lead to good precision (discussed later in 4.3) and obtain mesh sizes that could be reduced in some cases. We set the width of the refined region equal to 2 times the thickness of the PR. The size of the elements in this region is kept constant in 0.005 cm, equivalent to two levels of mesh refinement. The transition region has also a width of 0.02 cm at each side of the refined region.

Finally, we recreate the domain mesh with the new refinement. In figure 25 we show the original and the final grid after regenerating it using the patches as background sources.

4.2 COMPUTATIONAL MODEL OF FDS AND ANEURYSMS

We compare the results of our simulation using the PMM approach with the results reported by Mut et al. [77]. In their study, they select three cerebral aneurysms with wide necks representative of aneurysms that may be considered for treatment with FD devices, and study the change in the hemodynamic variables after implanting FDs of increasing

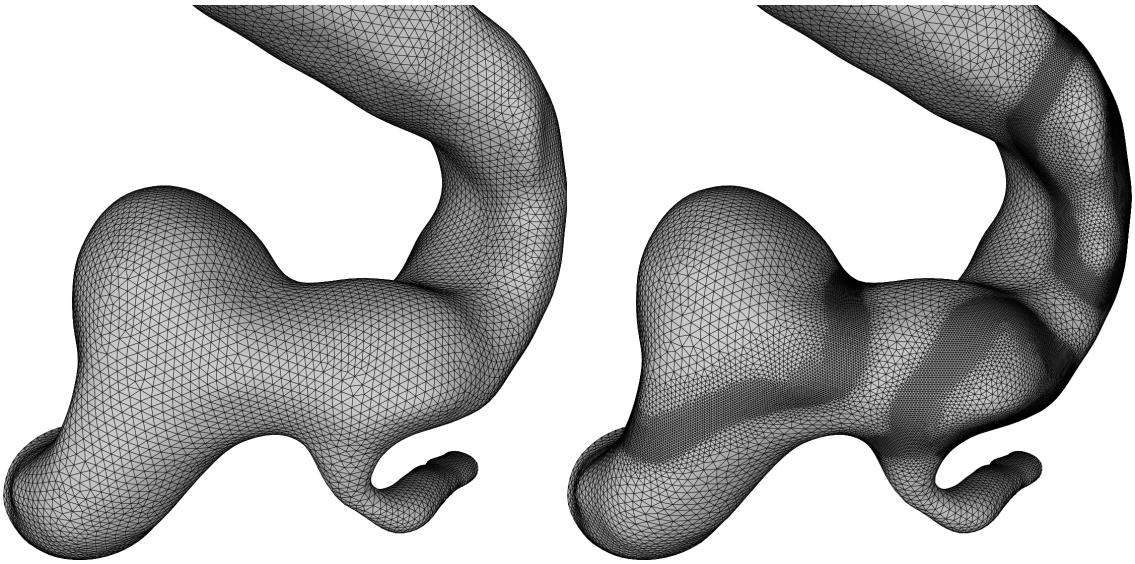

(a) (b)

Figure 25: (a) Original grid used for the simulation of the flow before the insertion of the FD. (b) Grid generated using the elements of the surface for the porous region as background sources.

diameter. For the comparison in this study, we select the same vascular models, computational parameters, and characteristic of the implanted FD.

Vascular models

The geometry of the three P-S wide neck aneurysm with representative characteristics that were selected is shown in figure 26. The curvature in the region of the neck presents different characteristics for each model. In the case of aneurysm 1, the curvature of the parent artery is not very pronounced. On the other hand, aneurysms 2 and 3 present a high curvature in the neck. In the case of the aneurysm 3, however, the neck is not clearly defined, as it takes most of the parent vessel.

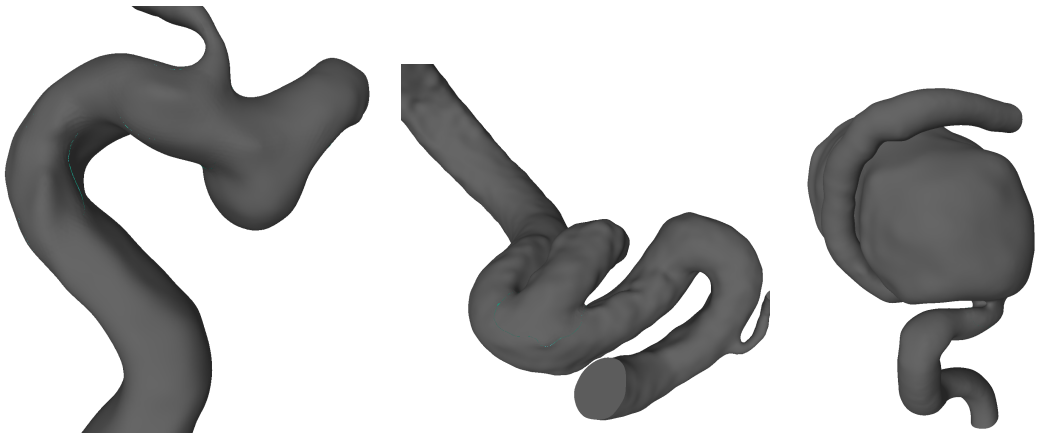

(a) Aneurysm 1 (b) Aneurysm 2 (c) Aneurysm 3

Figure 26: Geometry of the vascular models considered

The mesh of each aneurysm 1-3 is unstructured, composed of tetrahedral elements of a base size 0.02 cm. The number of elements of the original mesh is approximately 5.7×10^5, 1.8×10^6, and 1.9×10^6, respectively for aneurysm 1, 2, and 3.

The meshes were regenerated using the patches shown in figure 27 as background sources, to obtain smaller elements (up to 0.005 cm, equivalent to a two-level refinement)

in the region close to the cylinder wall. The thickness of the refinement and transition regions (4.1.3) are 0.03 cm and 0.015 cm. After the refinement, the number of elements

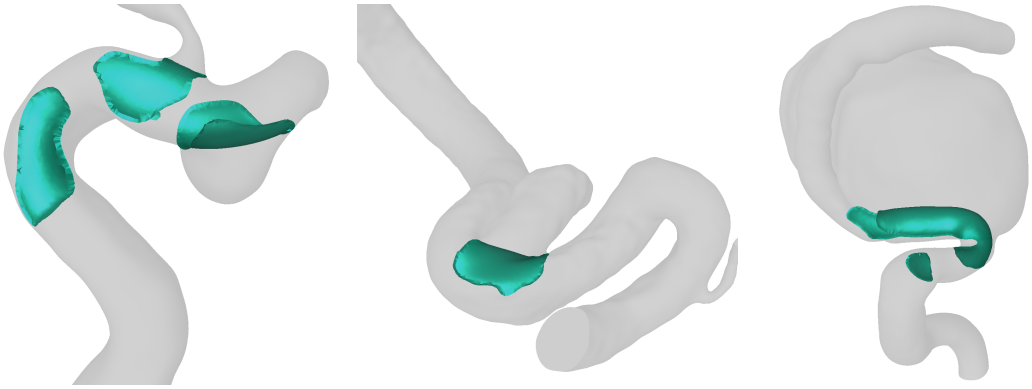

(a) Aneurysm 1 (b) Aneurysm 2 (c) Aneurysm 3

Figure 27: Patches for porous region

increased to 2.7×10^6, 2.7×10^6, and 7.0×10^6, respectively.

Device models

The FD modeled corresponds to a PED design of 48 strands with a diameter of 48 µm. The geometrical properties of the FD depends on the effective diameter, and this value varies along the artery. To compute the effective diameter, we calculated the mean diameter of the deployed cylindrical surface (obtained as explained in section 4.1.1) in the region of the neck. From the value of the effective diameter D_{eff} and the number of cells n_c, we determine the braiding angle α between strands, the porosity β, and the hydraulic diameter d_h of each FD.

The PR is defined using the patches shown in figure 27 and a thickness of 0.02 cm. The porosity parameters are computed using equations 35 and 36 (deducted from and empirical correlation) and corrected for overestimation of taking $D_{corr} = 0.75D$ and $F_{corr} =$

0.86F (section 3.4.6). The corrected values of the parameters used and the geometrical properties for each FD are shown in table 2.

Table 2: Geometric properties and porosity parameters of the FD

FD	D_{eff} (cm)	α	β	d_h (cm)	D (cgs)	F (cgs)
A	0.35	150°	0.354	4.66×10^{-3}	3977.41	76.14
B	0.35	115°	0.648	1.26×10^{-2}	1472.52	12.42
C	0.35	97°	0.709	1.62×10^{-2}	1147.39	8.80
D	0.43	135°	0.604	1.06×10^{-2}	1732.58	15.95
E	0.43	112°	0.718	1.69×10^{-2}	1092.67	8.38
F	0.43	98°	0.757	2.03×10^{-2}	905.95	6.69

Hemodynamic models

The hemodynamic model conveys the specification that follow: The value of density is $\rho = 1.0\,gr/cm^3$ and viscosity $\mu = 0.04$ Poise. The inflow curve used as boundary condition at the inlet in all the cases is shown in figure 28, with a mean flow of $3\,cm^3/s$ and a peak flow of $5.4\,cm^3/s$. Pulsatile CFD simulation were performed for 2 cycles, and the results are presented for the second cycle.

The details of the schemes used in the solver are explained in section 2.2.3

4.3 RESULTS

Visualizations of the results obtained for each of the 3 aneurysms are presented in figures 32, 33, and 34 (aneurysm 1), figures 29, 30, and 31 (aneurysm 2), and figures 35, 36,

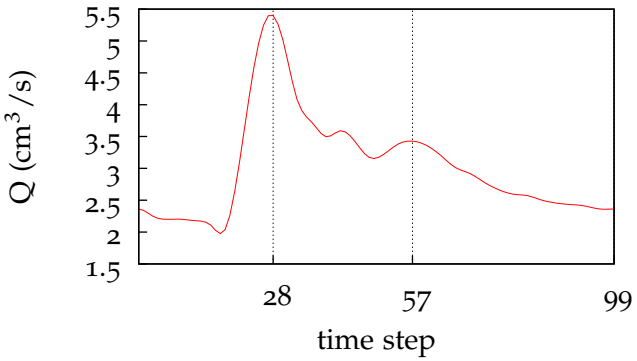

Figure 28: Inflow curve. The time steps 28, 57, and 99 are used to compare the solutions between the immersed and porous medium methods.

and 37 (aneurysm 3). Columns in these figures correspond to the times 28, 57, and 99 of the 100 time steps of the cardiac cycle shown in figure 28. The top row of each figure (subfigure a) corresponds to the case before the FD insertion (Pre). The following subfigures (b, c, and d) correspond to a different FD each, where the upper row of each subfigure shows the results for a IMM simulation, and the results obtained using the porous method are shown in the lower row. The case name is codified with the combination aneurysm-device used in each case (i. e. case 1A corresponds to aneurysm 1 with the device A). The geometry of each stent used in the IMM cases is also shown.

For each set of figures, the first figure shows the corresponding intra-aneurysmal flow patterns by using streamlines color-coded with the velocity magnitude; the second figure shows isovelocity surfaces depicting the blood streams flowing into the aneurysms; the third figure shows the corresponding WSS distributions, in all cases for each of the devices considered.

These visualizations illustrate the hemodynamic alterations produced by the implantation of FD of varying porosities, obtained with the IMM and the PMM.

We see in all the cases, that the FD effectively blocks and disrupts the inflow jets, resulting in reduced aneurysmal inflow. In addition, the flow velocity inside the aneurysm sac is substantially reduced after implanting the devices, and the flow structures become simpler and smoother showing fewer vortex structures, more parallel streamlines, less swirling, and reduced WSS on the aneurysm sac. All these alterations tend to create a hemodynamic environment that is more favorable for thrombosis and aneurysm occlusion. This behavior is predicted well by PMM in aneurysm 1 and 2. However, the flow structures obtained for aneurysms 3 present more differences among each method than in the cases with the other aneurysms.

These results are better analyzed and compared quantitatively as shown in the next section.

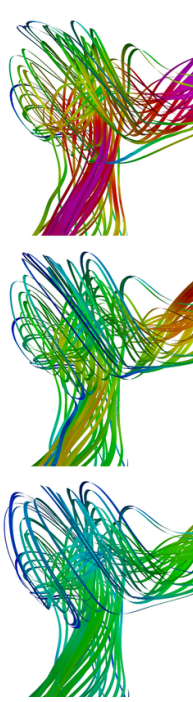

(a) Pre

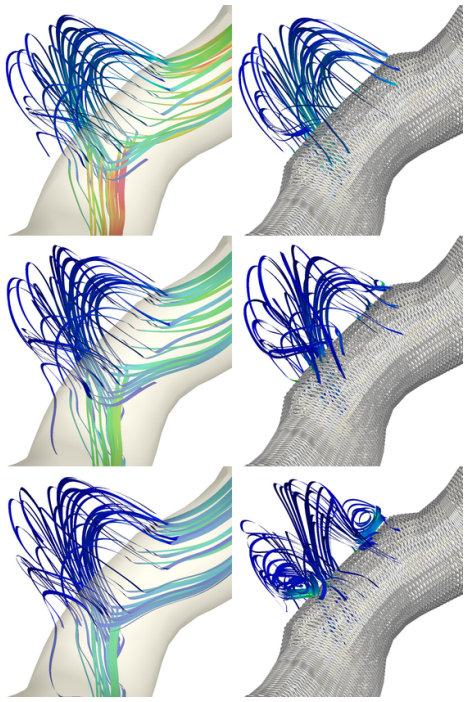

(b) Aneurysm 1, device A; (l) PMM, (r) IMM

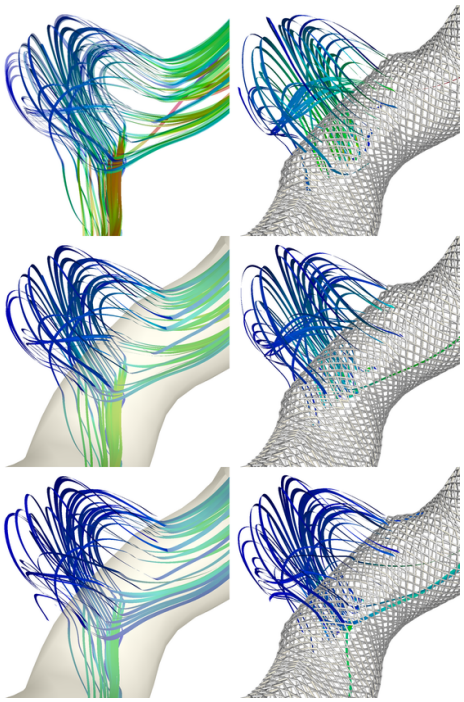

(c) Aneurysm 1, device B; (l) PMM, (r) IMM

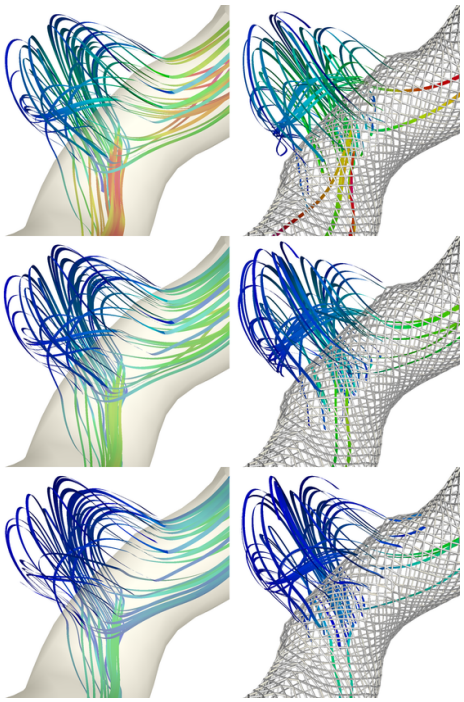

(d) Aneurysm 1, device C; (l) PMM, (r) IMM

Figure 29: Streamlines. Velocity: 0 cm/s to 100 cm/s. Rows top to bottom: times 28, 57, 99

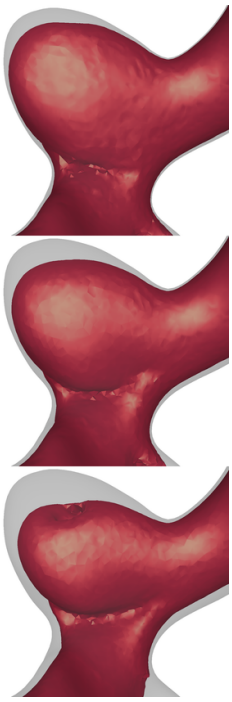

(a) Pre

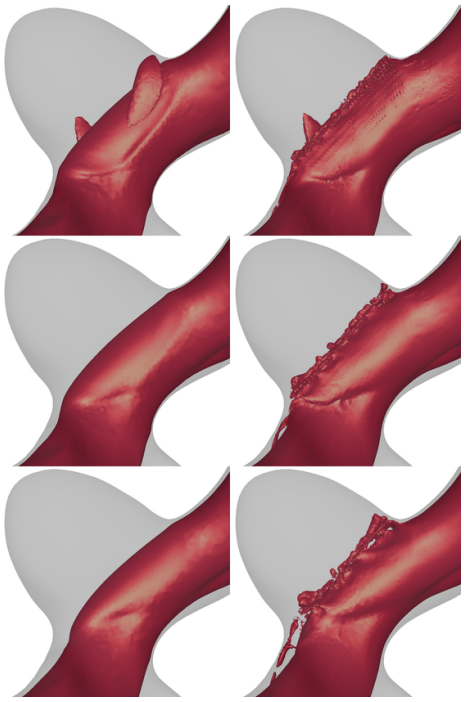

(b) Aneurysm 1, device A; (l) PMM, (r) IMM

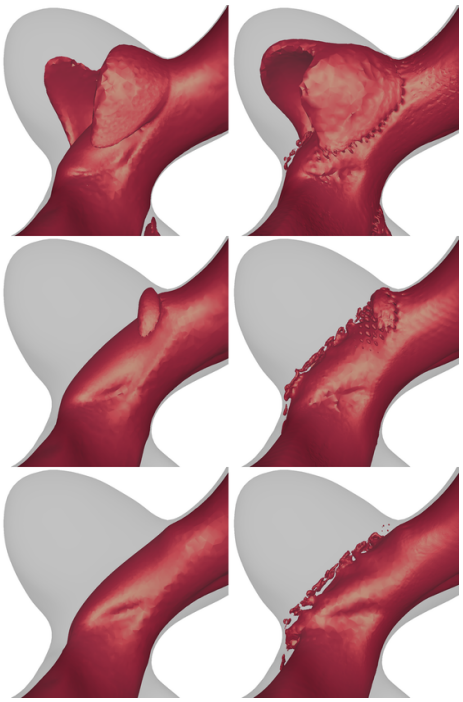

(c) Aneurysm 1, device B; (l) PMM, (r) IMM

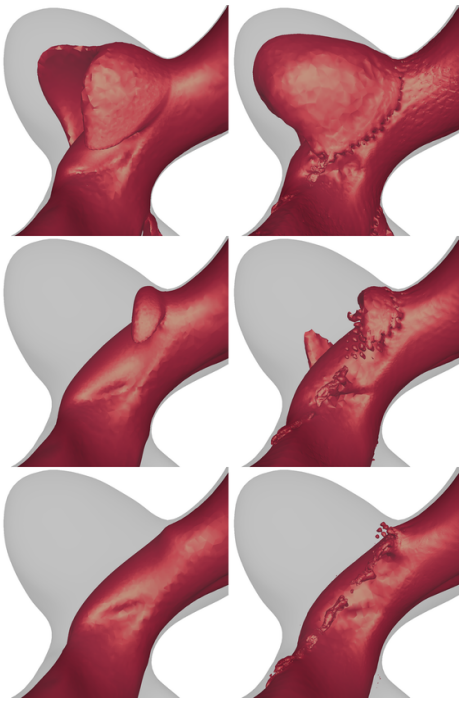

(d) Aneurysm 1, device C; (l) PMM, (r) IMM

Figure 30: Isosurface. Velocity: 20 cm/s. Rows top to bottom: times 28, 57, 99

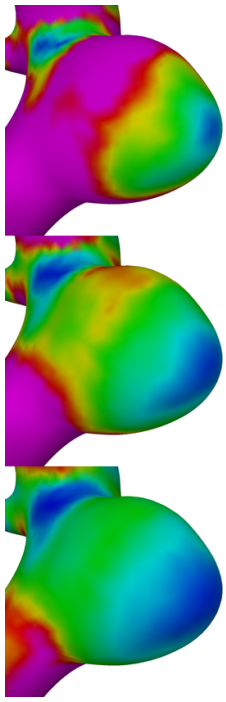

(a) Pre

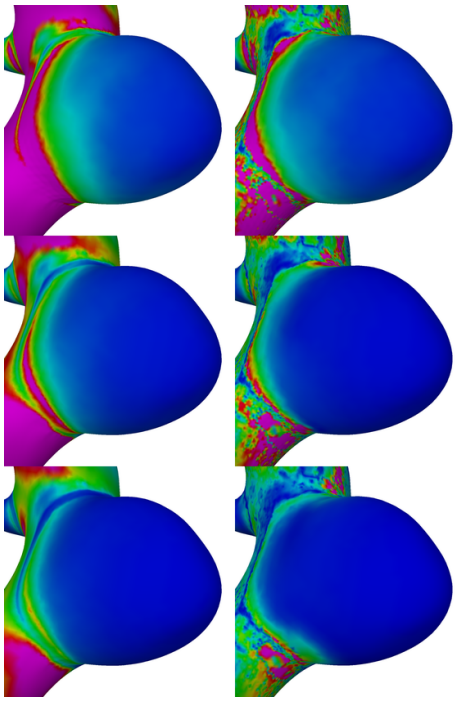

(b) Aneurysm 1, device A; (l) PMM, (r) IMM

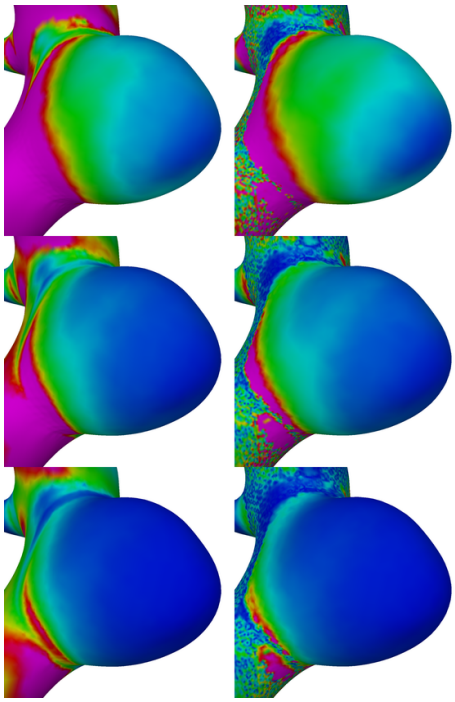

(c) Aneurysm 1, device B; (l) PMM, (r) IMM

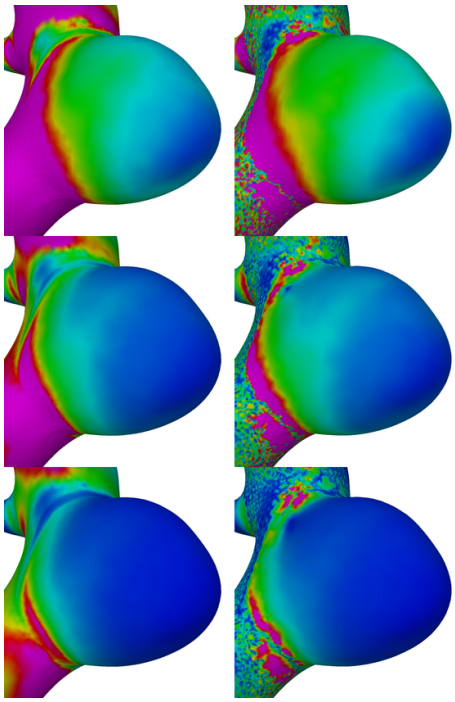

(d) Aneurysm 1, device C; (l) PMM, (r) IMM

Figure 31: WSS. Rows top to bottom: times 28, 57, 99

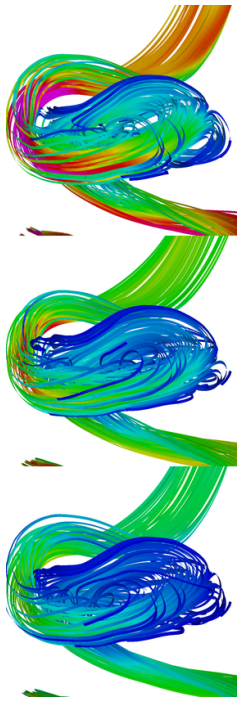

(a) Pre

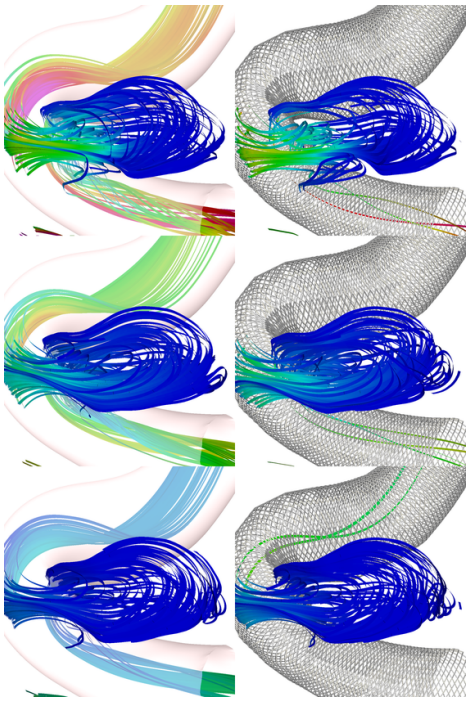

(b) Aneurysm 2, device A; (l) PMM, (r) IMM

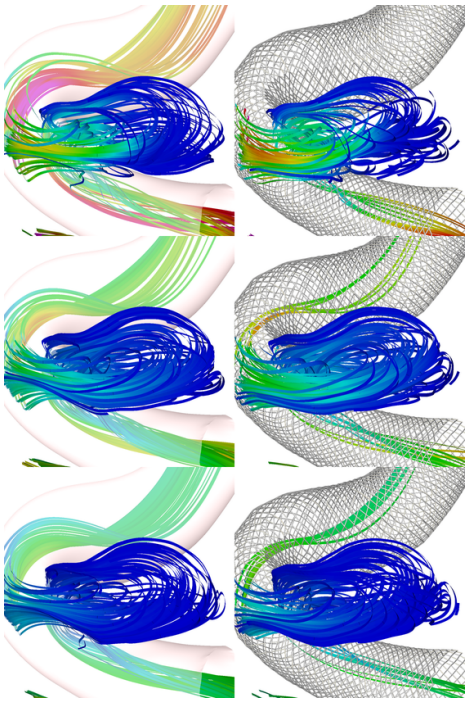

(c) Aneurysm 2, device B; (l) PMM, (r) IMM

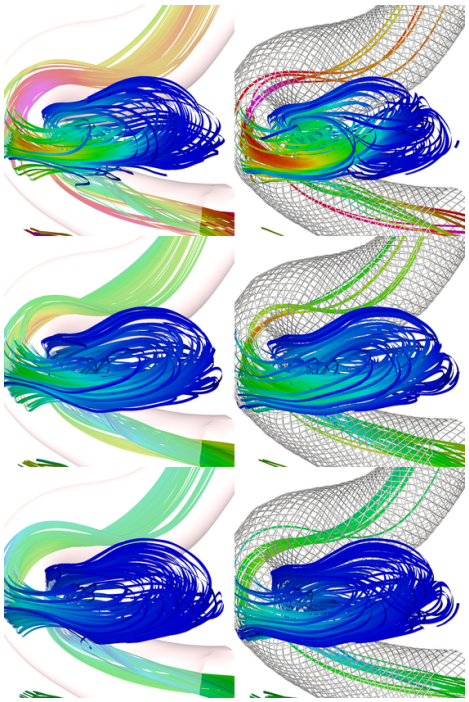

(d) Aneurysm 2, device C; (l) PMM, (r) IMM

Figure 32: Streamlines. Velocity: 0 cm/s to 100 cm/s. Rows top to bottom: times 28, 57, 99

(a) Pre

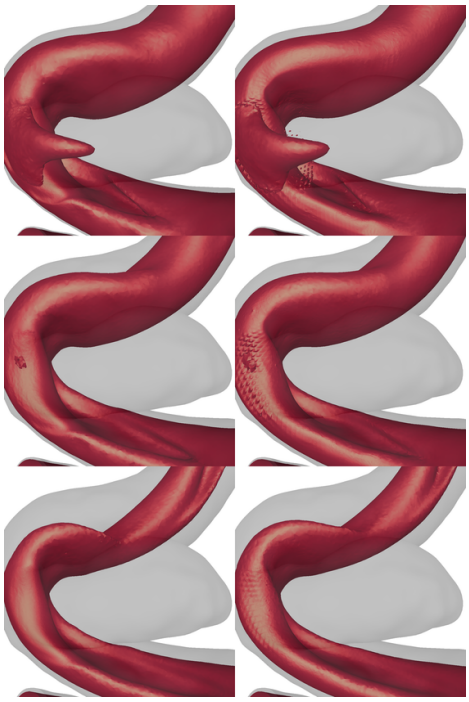

(b) Aneurysm 2, device A; (l) PMM, (r) IMM

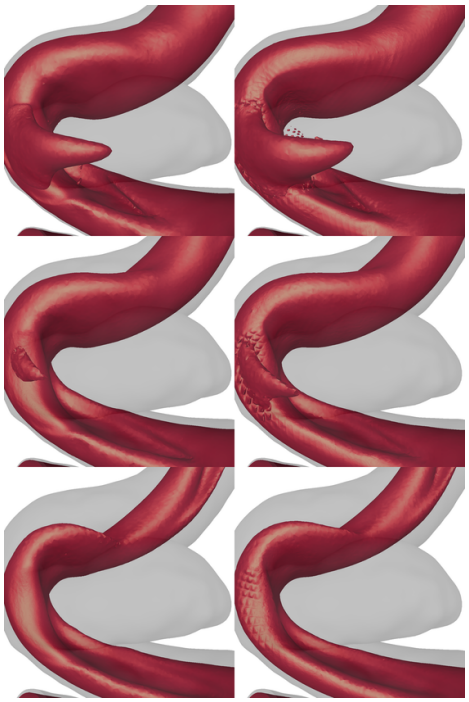

(c) Aneurysm 2, device B; (l) PMM, (r) IMM

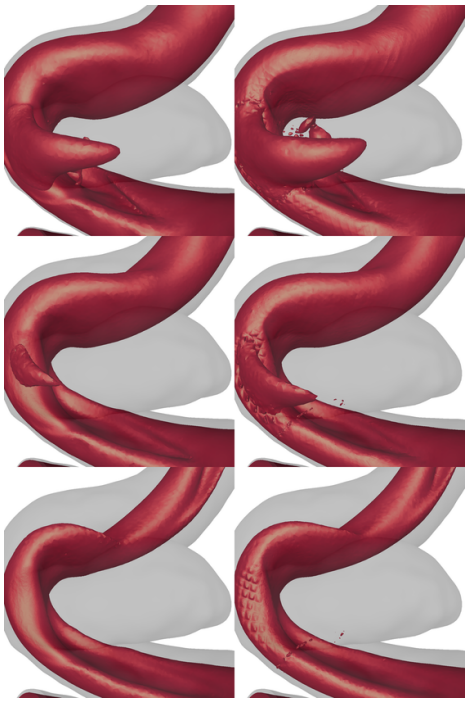

(d) Aneurysm 2, device C; (l) PMM, (r) IMM

Figure 33: Isosurface. Velocity: 20 cm/s. Rows top to bottom: times 28, 57, 99

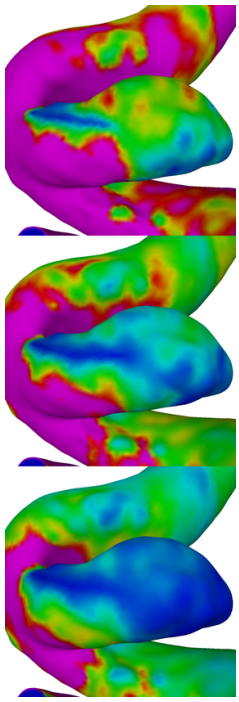

(a) Pre

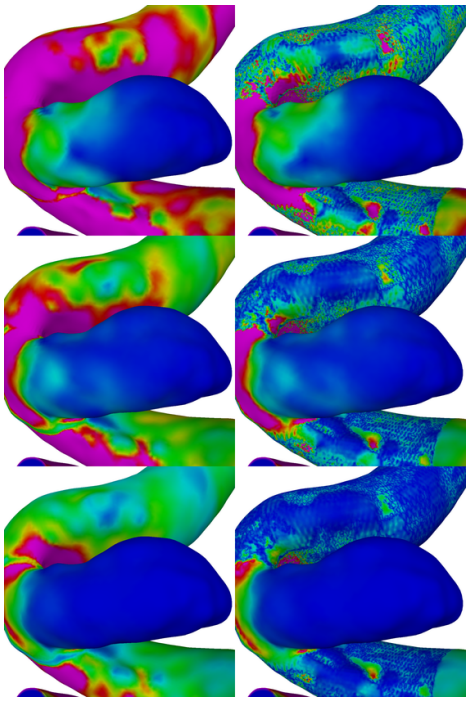

(b) Aneurysm 2, device A; (l) PMM, (r) IMM

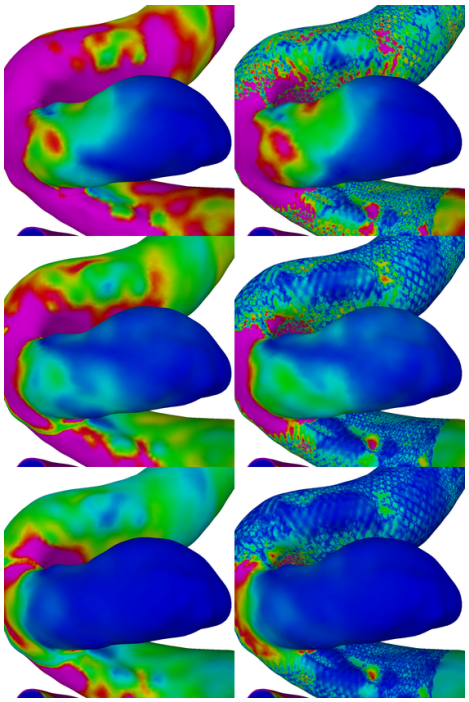

(c) Aneurysm 2, device B; (l) PMM, (r) IMM

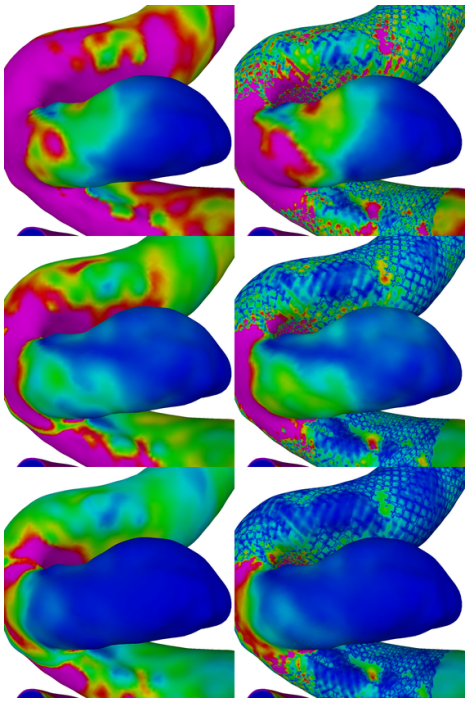

(d) Aneurysm 2, device C; (l) PMM, (r) IMM

Figure 34: WSS. Rows top to bottom: times 28, 57, 99

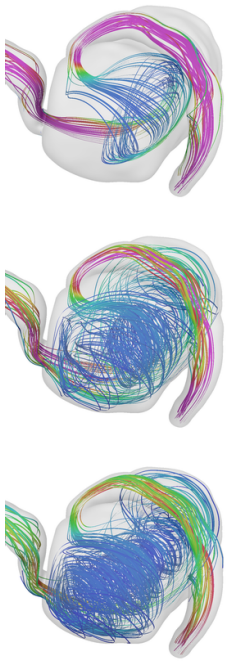

(a) Pre

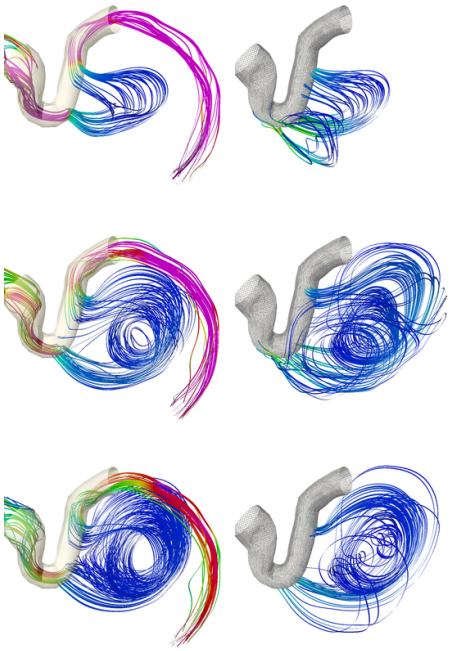

(b) Aneurysm 3, device A; (l) PMM, (r) IMM

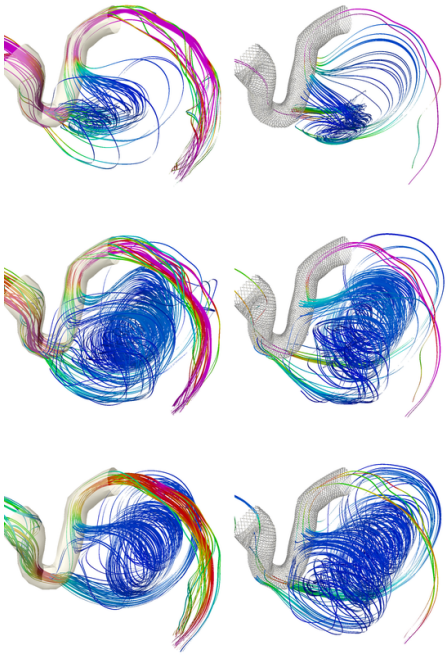

(c) Aneurysm 3, device B; (l) PMM, (r) IMM

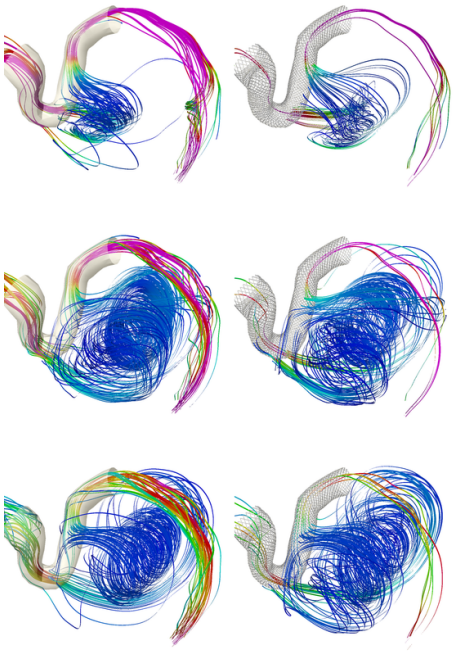

(d) Aneurysm 3, device C; (l) PMM, (r) IMM

Figure 35: Streamlines. Velocity: 0 cm/s to 60 cm/s. Rows top to bottom: times 28, 57, 99

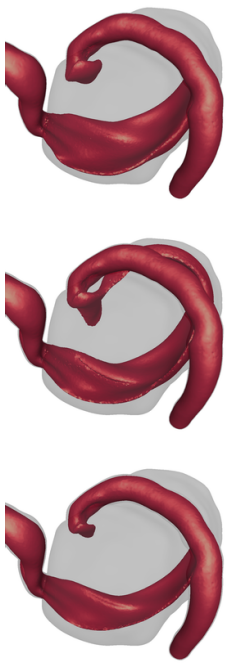

(a) Pre

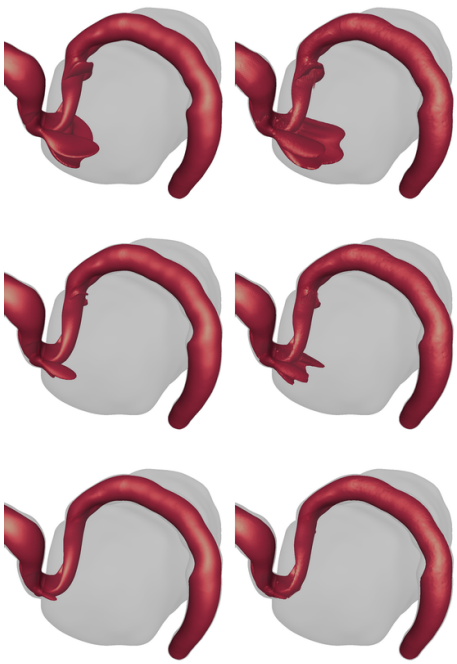

(b) Aneurysm 3, device A; (l) PMM, (r) IMM

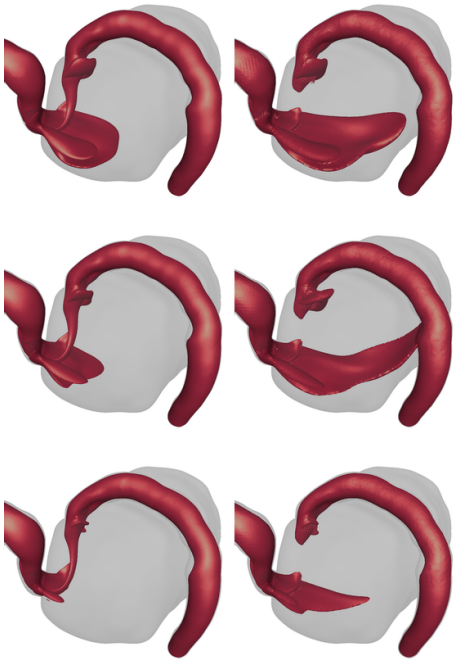

(c) Aneurysm 3, device B; (l) PMM, (r) IMM

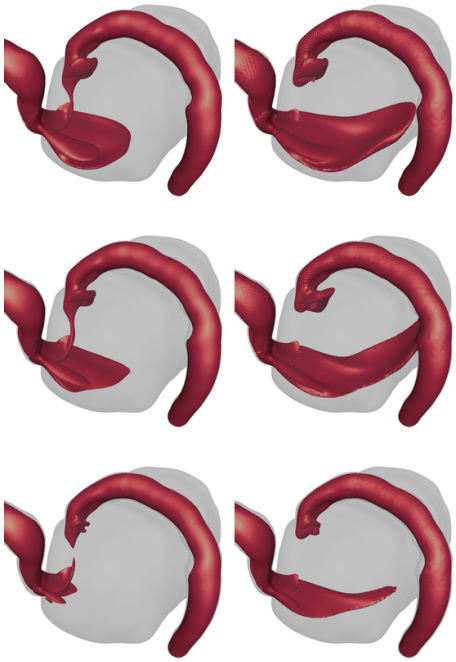

(d) Aneurysm 3, device C; (l) PMM, (r) IMM

Figure 36: Isosurface. Velocity: 15 cm/s. Rows top to bottom: times 28, 57, 99

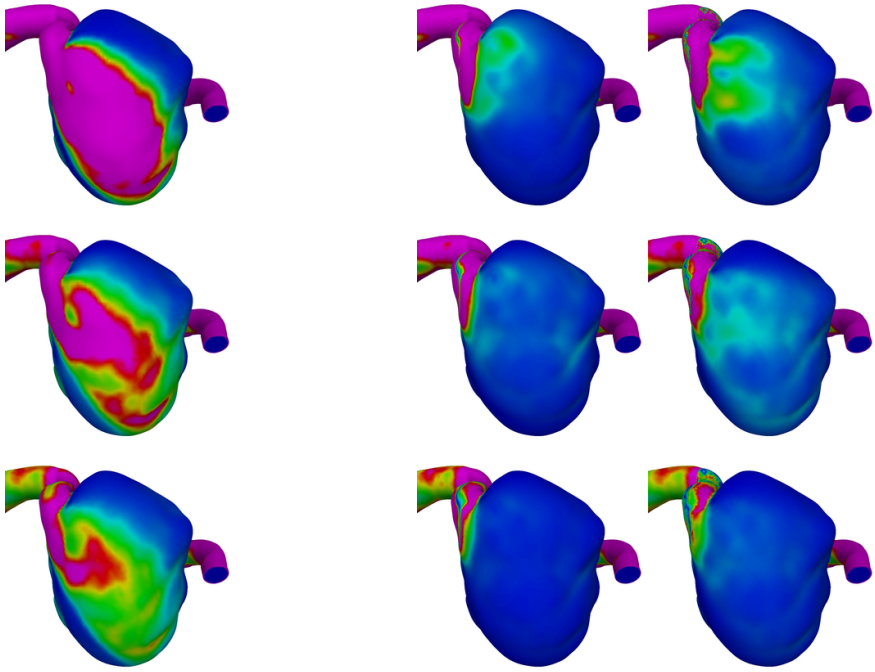

(a) Pre

(b) Aneurysm 3, device A; (l) PMM, (r) IMM

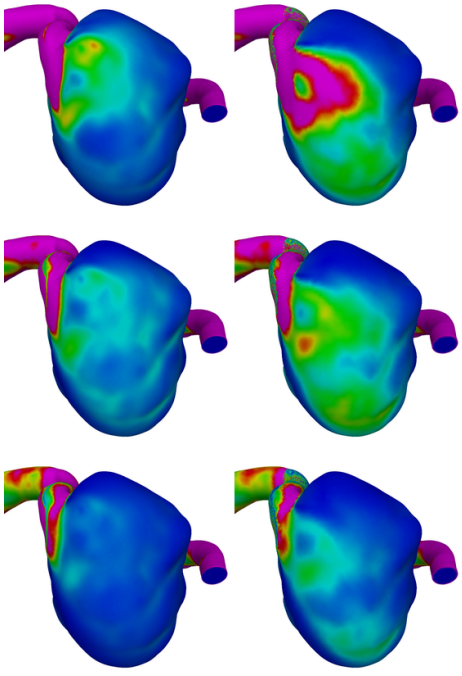

(c) Aneurysm 3, device B; (l) PMM, (r) IMM

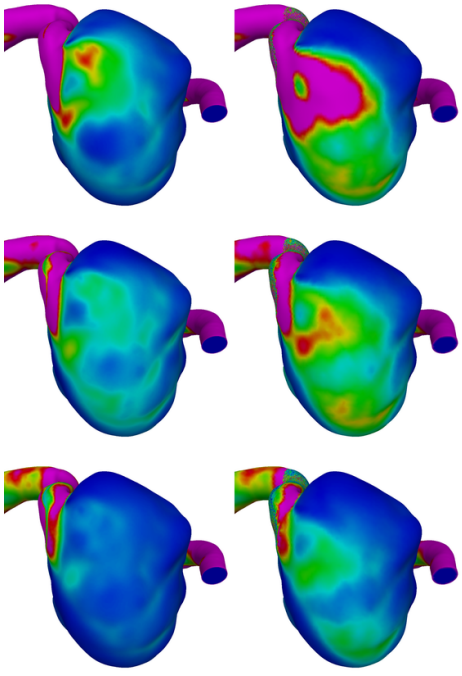

(d) Aneurysm 3, device C; (l) PMM, (r) IMM

Figure 37: WSS. : times 28, 57, 99

4.3.1 *Quantitative results*

For a quantitative analysis of the results we compare the hemodynamic variables used for the characterization of the flow pattern, averaged during the cycle and spatially in the sac of the aneurysm. The selected quantities shown in the comparison are:

1. Aneurysm inflow
2. Shear rate
3. Velocity
4. Vorticity
5. WSS

These metrics are useful to characterize the intra-aneurysmal hemodynamic environment, and their decrease in value is related to the development of an intrasaccular thrombus.

We study the reduction of each variable above (H_{1-5}) after the insertion of the FD (H_i/H_{PREi}), as this represent the physiological effect required for the device. Figure 38 compares how variables $H_1 - H_5$ decrease after the insertion of the FD when methods PMM and IMM are used (H_{PMMi}/H_{PREi} vs. H_{IMMi}/H_{PREi}).

Figure 38: Reduction of hemodynamic quantities after the insertion of the FD, obtained using IMM (gray bar) and PMM (blue bar). The case name is coded with the combination aneurysm-device used in each case, so case 1A corresponds to aneurysm 1 with the device A. In most of the cases, the reduction obtained by PMM is higher than by IMM; in the cases 1A and 2D, the reduction is slightly lower in some of the variable for the PMM case. This value is represented by the short black line.

When the differences in the reduction of the hemodynamic variables obtained by both methods are appreciable, the behavior of PMM seems to be consistent in predicting a higher reduction of the variables. The reduction of variables depends on the porosity of the FD, being less evident as the porosity increases. The difference in the reduction of the variable predicted by both methods in aneurysms 1 and 2 goes up to 10% with the higher porosity devices. For aneurysm 3, the differences in the reduction can go up to 25%. There is also consistency in the difference of the reduction for each variable among the cases of aneurysm 1 and 2, having the aneurysm inflow and the WSS the lowest difference, followed by the velocity, and the highest difference being for shear and vorticity.

We also compared the relative difference of the results by both methods $((H_{PMMi} - H_{IMMi})/H_{IMMi})$. Table 3 shows the relative difference of each of the variables for each case. As an estimation of the global difference of each case, we also added the root mean square value. We must note that the relative difference between results does not directly represent the physiological effect represented by the reduction of the variables. As an example, consider the case 1A, with a relative difference of -27% in the velocity, representing only 3% of difference in its reduction.

The relative differences between both methods also increases with porosity. The average difference between IMM and PMM increases from case 1A to 1C, and also from case 2D to 2F, which coincides with an increase in the porosity.

Aneurysm 3, however, exhibits a particular behavior different from aneurysm 1 and 2, which is due to an important curvature in the neck region, with a high variation of the local porosity. The increase of the porosity in the region of the outer curvature reduces the hydraulic resistance of the device and allows for more flow entering the aneurysm. This effect can not be reproduced with the PMM as a constant porosity with no local variation is assumed.

Table 3: Relative difference of the hemodynamic variables, and root mean square value of the case.

CASE	INFLOW	SHEAR	VEL	VORT	WSS	RMS
1A	−1 %	11 %	−27 %	3 %	−11 %	14 %
1B	16 %	21 %	16 %	21 %	9 %	17 %
1C	15 %	23 %	22 %	25 %	13 %	20 %
2D	−3 %	0 %	−4 %	−1 %	−9 %	5 %
2E	7 %	15 %	14 %	16 %	13 %	13 %
2F	10 %	19 %	18 %	21 %	20 %	18 %
3A	10 %	31 %	29 %	34 %	40 %	31 %
3B	12 %	27 %	20 %	30 %	40 %	28 %
3C	9 %	24 %	16 %	27 %	37 %	25 %

4.3.2 *Timing and size increase*

Table 4 shows the total number of elements of the models for each case considered.

The size of the model depends on the methodology used fo the simulation. In current IMM simulations, the mapping of the FD is applied to the whole cylindrical surface. In contrast, for the case of PMM, it is necessary to discard the regions of the cylinder that are in contact with the artery wall. The ratio of the resulting patches area to the whole cylinder area is between 5% for aneurysm 2, and up to 50% as in the case of aneurysm 3.

To estimate the increment of the model size with each of these approaches, we first subtracted from every case the number of elements of the corresponding pre-stenting model, to better approximate the new elements added by each method. Second, we normalized

Table 4: Total number of elements of the aneurysm models (10^6)

METHOD	DEVICE	ANEU 1	ANEU 2	ANEU 3
Pre	—	0.6	1.8	1.9
PMM	A–F	2.7	2.7	7.0
IMM	A/D	57.3	68.6	44.9
IMM	B/E	43.0	56.3	38.2
IMM	C/F	38.2	50.9	35.0

the number of elements of the IMM case with a factor = A_{patch}/A_{total}, where A_{patch} is the corresponding PMM patch area, and A_{total} is the total area of the cylinder, in order to have a meaningful comparison against the models of PMM (39).

The increase in the number of elements depends on the geometry of the artery, on the size of the neck, and on the porosity of device. The number of elements added by the PMM is smaller that the new elements added by IMM, varying from 17% to 24% for aneurysm 1, 23% to 32% for aneurysm 2, and 32% to 41% for aneurysm 3.

Figure 40 shows the time of completion of the first time step of the simulation, running on a single processor. The cases considered are 1A, 2D, and 3C, using methods IMM, PMM, and the pre-stenting case. The timing shown in the figure is not normalized by the number of elements of the model, instead it is a direct comparison of the time corresponding to the whole model.

The assessment on the time performance of PMM relative to IMM is not straightforward.

As the the run time of the simulation is exponentially related to the number elements of the model (by an order $\mathcal{O}(1.5)$, estimated from tests), the differences in size can be used to estimate the time differences.

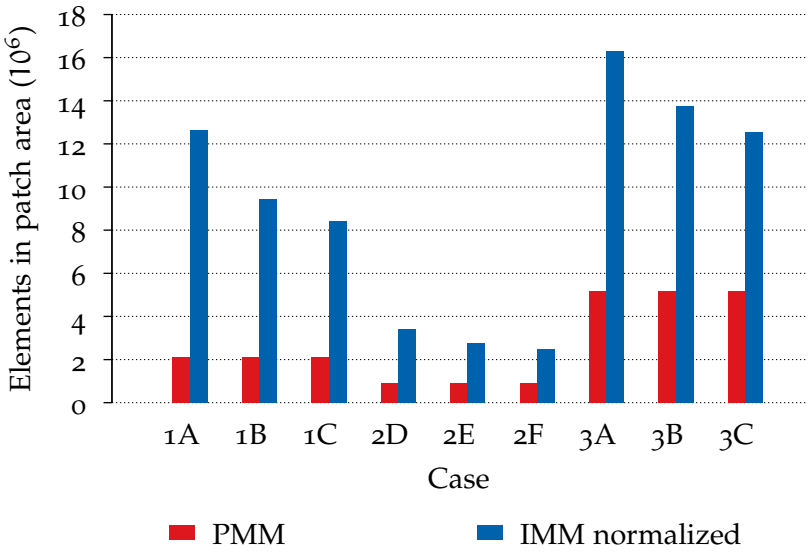

Figure 39: Number of elements of the model of each case, normalized to the corresponding patch area, after subtracting the number of elements of the pre-stenting model.

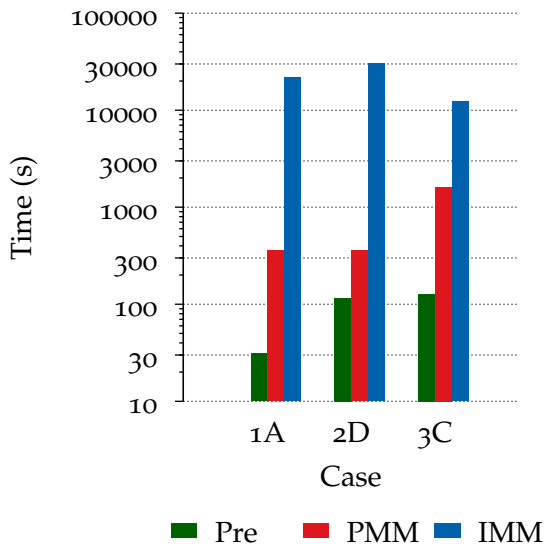

Figure 40: Time of completion of the first time step of the simulation of selected cases, comparing the model using PMM, IMM, and the pre-stenting (Pre) model.

For the same reason as in the comparison of sizes, the analysis of the simulation run time has to consider models normalized by the area of the FD.

In figure 41 we show how the differences in model size, previously reported in figure 39, are translated into time differences by adding the contribution of the non-refined elements and applying an exponential factor of 1.5.

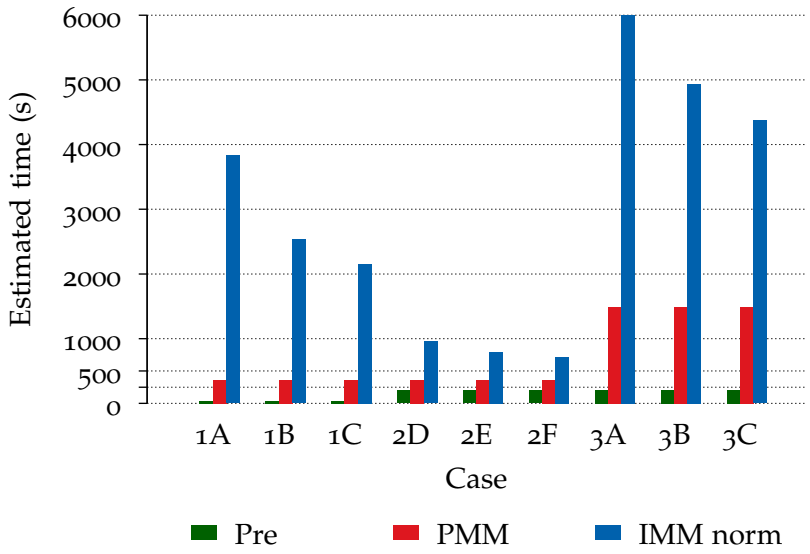

Figure 41: Estimated timing of PMM and IMM normalized with the patch area. The run time of cases Pre and PMM are measured, and in the case of the normalized IMM model, it is estimated from the size difference (39), adding non-refined elements, and considering and exponent 1.5.

The ration of the estimated time of the normalized IMM models to the time of the PMM models varies between cases from 2 to 10.

4.3.3 *Error vs computational cost*

In order estimate the variation of the accuracy of the solution with the number of elements of the mesh, we simulated the case 2D (aneurysm 2 with device D) modifying the size of the elements in the refined region. We compared the difference in the reduction of the aneurysm inflow obtained by PMM and IMM ($\text{Inflow}_{\text{PMM}}/\text{Inflow}_{\text{IMM}} - 1$), and the variation of the mesh size, for different sizes of the elements in the refined region (figure 42). We

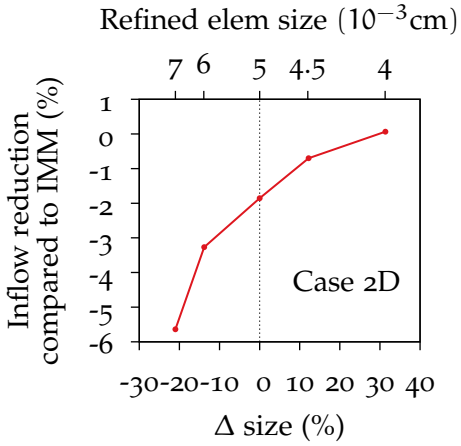

Figure 42: Difference in the reduction of the inflow obtained by PMM and IMM, and variation in the mesh size, for different sizes of the refined elements, case 2D.

found that modifying the size of the refined elements from 7×10^{-3} cm to 4×10^{-3} cm, the number of elements of the mesh varies from $-20\,\%$ to $30\,\%$, which implies increments in the running time from roughly $-30\,\%$ to $50\,\%$. The difference in the reduction of the inflow varies from $-6\,\%$ to $0\,\%$ in the same range of elements size.

4.4 DISCUSSION

The use of PMM as an alternative strategy to the IMM for the modeling of FD provides the possibility of simulating the alterations to the flow pattern before and after an actual endovascular intervention, with the advantage of an accurate yet, time efficient calculation. This type of study allows the clinician to plan the best treatment for a particular patient, since the results of this calculation can be delivered in a timeframe of hours as compared to the standard procedure that usually takes weeks of run time.

Our approach to the computational simulation of FDs is to utilize a PMM that recreates the pressure drop in an equivalent FD, considered as a flat wire screen. Our method relies on parameters from an empirical correlation for the pressure drop as a function of the Reynolds number, reported in the literature. This brings together three advantages. To begin with, the correlation is based on general geometric parameters such as porosity and hydraulic diameter, which can be applicable to any design of FD. Second, the empirical correlation is derived from experimental observations in wire screens. Thirdly, obtaining the porosity parameters does not require running additional CFD simulation. On the other hand, in this work we have validated the use of this parameters by agreement with parameters obtained from CFD simulations.

We implemented the PMM and simulated several cases with different P-S aneurysms, inserting FD of different porosity. To quantitatively compare the hemodynamic performance of the two methods, we selected the following metrics: 1) aneurysm inflow rate, 2) average shear rate of blood flow within the aneurysm, 3) average blood velocity within the aneurysm, 4) average blood vorticity within the aneurysm, and 5) average WSS. These metrics are useful to characterize the intra-aneurysmal hemodynamic environment and its relation to the development of an intrasaccular thrombus. Aneurysm inflow rate relates to blood flow speed and the creation of regions of slow flow recirculation and stagnation within the aneurysm sac. Low-flow velocity relates to regions prone to thrombus formation. Low shear rate relates to the non-Newtonian behavior of blood, which con-

nects blood viscosity, yield stress, and platelet aggregation. Wall shear stress measures the frictional force per unit area of blood flow on the aneurysm wall, which relates to the likelihood of platelet adhesion to the wall and thrombus formation near the wall.

The simulations using the PMM show that the reductions of the observed hemodynamic quantities and the intra-aneurysmal hemodynamic environment created are comparable with the simulations made using the IMM. In presence of the FD device, both methods yield an environment that is more favorable for thrombosis and aneurysm occlusion.

For aneurysm 1 and 2, PMM seems to predict well the reduction of these variables, with a difference in the reduction of the averaged hemodynamic quantities between 3% and 10% for all cases with these aneurysm Their corresponding flow structures also seems to be similar during the cardiac cycle.

However, aneurysm 3 presents higher differences in the flow reduction, in the relative difference and in the flow structure. There are limitations in the current implementation of the PMM that may generate important differences with the IMM, as in the case of aneurysm 3, given its particular geometry, i. e. high curvature of the neck. The PMM, as currently implemented, assumes a constant porosity of the FD in the area of the neck, with a value for the parameters for the porous model are based on the mean diameter and mean angle of the cells of the FD in the area of the neck. In contrast, the simulations in the IMM cases consider the local deformation of the cells of the FD due to foreshortening and curvature of the artery.

Foreshortening appears when the diameter of the artery is smaller than the diameter of the FD. In that case, the cells stretch in the direction of the vessel axis, changing the internal cell angles and resulting in effectively larger cells areas. Although not recommended by manufacturers, FD are often oversized to achieve adequate appositioning against the parent artery wall, selecting devices of diameter that exceed the parent artery diameter by 0.5 mm or more.

Elongation and contraction of the device cells can also occur due to the curvature of the vessels. It is observed that in the outer region of a curved vessel, the cells elongate whereas

in the inner region, the cells contract and can even be occluded. The deformation of the final cell shape due to this effect can be important, greatly modifying the average effective shape due to only foreshortening. The porosity of the FD, which is directly related to the shape of the cell, will also vary locally. This change in the local porosity is not represented in our current implementation.

Also, if the physician pushes and pull on the catheter during deployment, the FD cells can be compacted and extended. This effect is difficult to reproduce, and the exact geometry of the device after deployment are unknown a priori. If the devices could be imaged after deployment, these images could be used to map the porosity distribution.

The geometries of the aneurysms used in this work show different curvature in the surroundings of the neck. The effect of the curvature in the deformation of the cells is shown in figure 43, together with a map of their porosity.

The cells of the FD A are not significantly deformed when inserted in aneurysm 1 (figure 43a) and the porosity in the area of the neck remains constant. The parent artery of aneurysm 2 (figure 43b) presents a bend before the neck of the aneurysm, causing contraction of the cells in the inner curvature and an expansion of the cells in the region of the outer curvature. However, the region of the neck is in-between the inner and outer curvature regions, and most of the cell deformation affects only the region of the boundary of the neck. The third case (figure 43c), aneurysm 3, also has an important bending of its parent artery. Here, the curvature effect on the cells is more notable than in aneurysm 2, showing collapsed cells even in the region of the inner curvature; the region of the neck in this aneurysm includes most of the extreme deformation.

Moreover, when the porosity is low, porosity becomes sensitive to the changes in geometry. This effect becomes evident particularly in case 3A, as with its low mean porosity of 0.354 in the region of the neck, the variation due to the curvature goes from 0.000 (-100 %) to 0.591 (+67 %). As a comparison, we can consider case 3B with a mean porosity of 0.648 and a variation from 0.000 (-100 %) to 0.758 (+17 %), in the same curved geometry as case

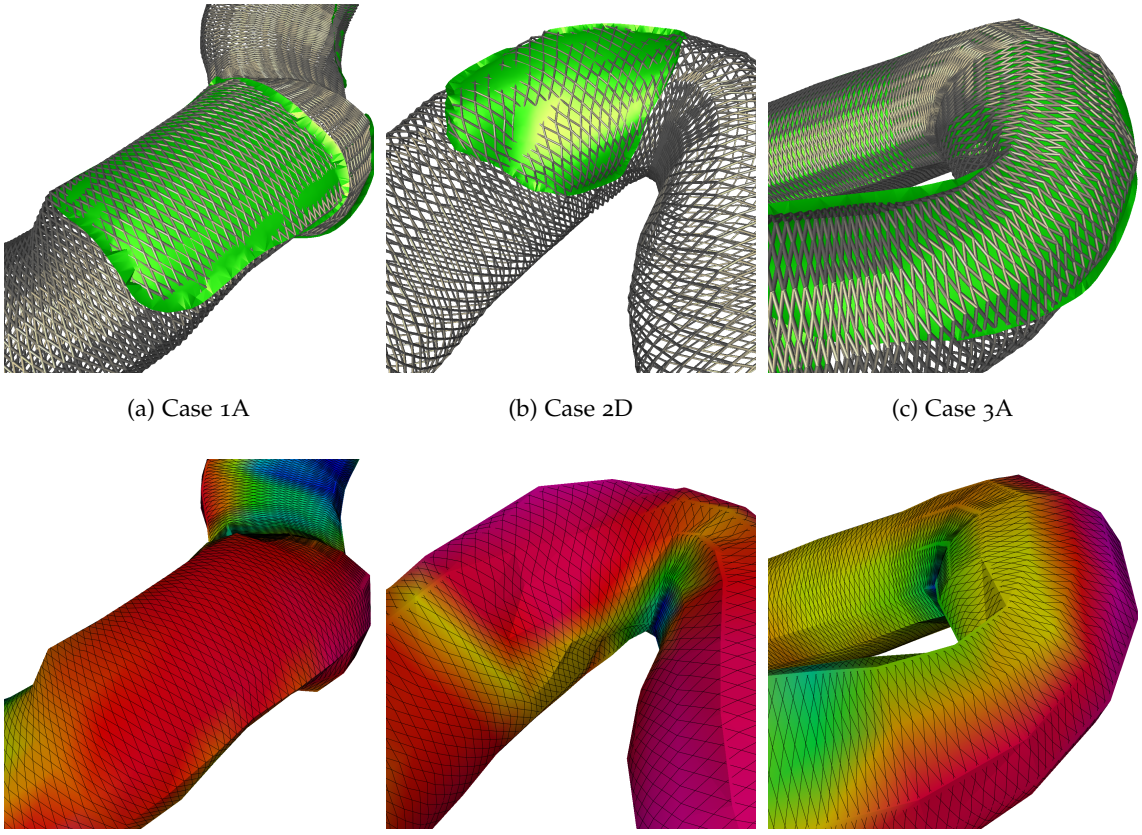

(a) Case 1A (b) Case 2D (c) Case 3A

(d) Case 1A (e) Case 2D (f) Case 3A

Figure 43: Deformation of the cells of FD due to the effect of the curvature. The three geometries show different curvatures in the area of the neck (indicated by the patch). Aneurysm 1 shows no major differences from the mean shapes. Aneurysm 2 shows differences in shape between the cells on the outer- and inner curvature. Aneurysm 3 shows the expanded cells on the outer curvature, and occluded cells on the inner curvature.

3A. These two cases show to what extent small changes in geometry can result in such acute changes in porosity.

Besides the variation in the local porosity of the neck, there are other possible sources of uncertainty. One possible source is the fact that all the patches in the model use the

same value of porosity computed for the neck, independently of their location in the aneurysm. Patches in, for instance, the perforation artery, are relevant for the regulation of the flow that feed the artery. The variation of the porosity will modify the flow through the perforating artery. Others patches are located in regions where the local porosity changes due to curvature effects. A constant value of porosity for these patches will affect the flow through the perforating artery. Even though this does not directly affect the flow inside the aneurysm, it modifies the flow pattern in the parent artery. Homogeneity in the value of porosity thus could contribute to the error in the simulation, being this error highly dependent on the geometry of the model. Further studies that take into account the local variation of the porosity are needed to fully assess this effect.

The second possible source of error, as discussed in section 3.4.6, is an overestimation in the computed pressure drop when using IB. Prior to the simulation, the overpressure needs to be estimated according to the mesh characteristics. The correction coefficients computed in this way are not constant, but have a variation of $\pm 3\%$ in the Re interval of interest.

The computational advantage of our approach comes from the fact that we need an element size equivalent to the size of 2 levels of refinement, given that the properties of the cell are represented in each element of the mesh. In contrast, IMM needs 4 levels of refinement to fully resolve the physical properties of the cell of the FD.

The duration of the simulation and the requirements on memory depend directly on the size of the geometric model with the requirements of memory being even higher for meshing the domain.

In comparisons using the same domain, the run time using IMM is between 2 and 10 times higher than the run times obtained with our strategy of simulation using PMM. In comparisons using the same domain, simulations using our method PMM are between 2 and 10 times faster than IMM.

Additionally, the current implementation of IMM considers the whole deployed cylinder in the model. The models simulated with PMM in this work have been a priori reduced,

excluding the surfaces that are in contact with the artery wall. This strategy reduces even further the number of elements depending on the particular model. The differences in time between the whole IMM model and the PMM model are up to 100 times higher.

CONCLUSIONS

When evaluating unruptured cerebral aneurysms, it is necessary to assess their risk of rupture and to compare them to the risks involved in their treatment. Simulations using the P-S geometry of the aneurysm may help in a better planning of the treatment and in a consequent reduction of the associated risks.

To have a better understanding of the rupture risks, we first review studies with the suggested hypotheses that connect the aneurysm risk factors and the mechanisms governing the aneurysm evolution. This literature review reveals a progressive wall degradation due to changing hemodynamic loading and biomechanic stress, affected by risk factors, that drives the geometrical evolution of the aneurysm until it stabilizes or ruptures. However, details of these interactions or their relative importance are still not clearly understood.

Second, to understand the influence of uncertainties involved in the P-S CFD simulations, we compare the blood flow field in a growing cerebral aneurysm obtained with experimental PIV and CFD techniques. Despite small differences observed, mainly associated to the inherent limitations of each technique, the information derived is consistent and can be used to study the role of hemodynamics in the natural history of intracranial aneurysms.

In this thesis, we also proposed a methodology to do faster, reliable and accurate simulations of aneurysms with FD, that overcome the time limitations of standard IMM simulations. Our approach to the computational simulation of FDs is to utilize a PMM that recreates the pressure drop in an equivalent FD, considered as a flat wire screen. With this strategy we carry on simulations between 2 and 10 times faster than using IMM, which allows for a run time of hours instead of days.

Our method relies on parameters from an empirical correlation for the pressure drop as a function of the Reynolds number, reported in the literature. This brings together three

advantages. To begin with, the correlation is based on general geometric parameters such as porosity and hydraulic diameter, which can be applicable to any design of FD. Second, the empirical correlation is derived from experimental observations in wire screens. Thirdly, obtaining the porosity parameters does not require running additional CFD simulation. On the other hand, in this work we have validated the use of this parameters by agreement with parameters obtained from CFD simulations.

We have applied the PMM method to three patient-specific aneurysm models with diverse geometric characteristics and curvature of the neck. We study the changes in the flow produced by 6 different FD which differ in porosity and several geometric characteristics. The simulations of the FDs in the aneurysm were compared to simulations of aneurysms in the absence of FD. The validation of our PMM strategy was carried out by comparing our results to those of the IMM method under identical conditions of aneurysms with and without FD. We qualitatively analyzed the flow structure at different instances of the cardiac cycle. In order to assess the validity of our method in terms of precision, we quantitatively evaluated and compared between methods the change in five hemodynamic observables: aneurysm inflow, shear rate, intra-aneurysm velocity and vorticity and wall shear stress.

Overall, both quantitative and qualitative results are consistent for both IMM and PMM methods for aneurysms 1 and 2 for all cardiac cycle instances, with relative errors between 5% and 20%, and differences in the reduction of the hemodynamic variables lower than 10%. We observe that, in general, the discrepancy between both methods increases with the porosity of FD for a given aneurysm. Possible sources of error include the variation in local porosity and the overestimation in pressure drop due to the definition of the region of porosity.

As it was observed in aneurysm 3, the high curvature of the neck produces an acute variation in local porosity resulting in discrepancies among methods of 40%.

Future work is in progress to overcome the sources of errors related to acute variations in local porosity. It is possible to calculate the porosity on each point of the FD,

and therefore local porosity values can be assigned to points on the mesh. Incorporating this functionality to the current implementation will majorly improve the simulation of geometries with high variation of the local porosity such as pronounced curvatures in the neck. Another avenue for future improvement involves the precision of the PMM. In contrast with IMM, the nature of our method allows the refinement of the mesh in the FD region to be customized to the requirements of the user in terms of precision, this would allow a dramatic gain in computational efficiency. It remains to be assessed to what extent changes in precision affect the accuracy of the results.

By introducing a methodology for modeling flow diversion as a porous medium, we incorporate a new application for a widely studied field such as porous media. Our PMM model significantly reduces the cost of FD simulations, thus bringing CFD technologies closer to the clinical application.

BIBLIOGRAPHY

[1] M. Aenis, AP Stancampiano, AK Wakhloo, and BB Lieber. Modeling of flow in a straight stented and nonstented side wall aneurysm model. *Journal of biomechanical engineering*, 119:206, 1997.

[2] S. Ahn, D. Shin, S. Tateshima, K. Tanishita, F. Vinuela, and S. Sinha. Fluid-induced wall shear stress in anthropomorphic brain aneurysm models: Mr phase-contrast study at 3 t. *J Magn Reson Imaging*, 25(6):1120–30, 2007. doi: 10.1002/jmri.20928.

[3] P. S. Amenta, S. Yadla, P. G. Campbell, M. G. Maltenfort, S. Dey, S. Ghosh, M. S. Ali, J. I. Jallo, S. I. Tjoumakaris, L. F. Gonzalez, A. S. Dumont, R. H. Rosenwasser, and P. M. Jabbour. Analysis of nonmodifiable risk factors for intracranial aneurysm rupture in a large, retrospective cohort. *Neurosurgery*, 70(3):693–9; discussion 699–701, 2012. doi: 10.1227/NEU.0b013e3182354d68.

[4] S Appanaboyina, M A Castro, R Löhner, and J R Cebral. Simulation of endovascular interventions of cerebral aneurysms: Techniques and evaluation. *SPIE Medical Imaging Conference, San Diego, CA*, 5746:769–779, 2005.

[5] S Appanaboyina, F Mut, R Löhner, C M Putman, and J R Cebral. Simulation of intracranial aneurysm stenting: techniques and challenges. *Computer Methods in Applied Mechanics and Engineering*, 198(45-46):3567–3582, 2009.

[6] G. Audibert, S. Bousquet, C. Charpentier, Y. Devaux, and P. M. Mertes. [subarachnoid haemorrhage: epidemiology, genomic, clinical presentation]. *Ann Fr Anesth Reanim*, 26(11):943–7, 2007. doi: 10.1016/j.annfar.2007.09.006.

[7] L. Augsburger, P. Reymond, DA Rufenacht, and N. Stergiopulos. Intracranial stents being modeled as a porous medium: Flow simulation in stented cerebral aneurysms. *Annals of biomedical engineering*, pages 1–14, 2011.

[8] J. Beck, S. Rohde, M. el Beltagy, M. Zimmermann, J. Berkefeld, V. Seifert, and A. Raabe. Difference in configuration of ruptured and unruptured intracranial aneurysms determined by biplanar digital subtraction angiography. *Acta Neurochir (Wien)*, 145(10):861–5; discussion 865, 2003. doi: 10.1007/s00701-003-0124-0.

[9] J. Beck, S. Rohde, J. Berkefeld, V. Seifert, and A. Raabe. Size and location of ruptured and unruptured intracranial aneurysms measured by 3-dimensional rotational an-

giography. *Surg Neurol*, 65(1):18–25; discussion 25–7, 2006. doi: 10.1016/j.surneu.2005.05.019.

[10] J. D. Boissonnat, R. Chaine, P. Frey, G. Malandain, S. Salmon, E. Saltel, and M. Thiriet. From arteriographies to computational flow in saccular aneurisms: the inria experience. *Med Image Anal*, 9(2):133–43, 2005. doi: 10.1016/j.media.2004.11.004.

[11] L. Boussel, V. Rayz, C. McCulloch, A. Martin, G. Acevedo-Bolton, M. Lawton, R. Higashida, W. S. Smith, W. L. Young, and D. Saloner. Aneurysm growth occurs at region of low wall shear stress: patient-specific correlation of hemodynamics and growth in a longitudinal study. *Stroke*, 39(11):2997–3002, 2008. doi: 10.1161/strokeaha.108.521617.

[12] A C Burleson, C M Strother, and V T Turitto. Computer modeling of intracranial saccular and lateral aneurysms for the study of their hemodynamics. *Neurosurgery*, 37:774–784, 1995.

[13] H. S. Byun and K. Rhee. Cfd modeling of blood flow following coil embolization of aneurysms. *Medical Engineering & Physics*, 26(9):755–61, 2004.

[14] B. S. Carter, S. Sheth, E. Chang, M. Sethl, and C. S. Ogilvy. Epidemiology of the size distribution of intracranial bifurcation aneurysms: smaller size of distal aneurysms and increasing size of unruptured aneurysms with age. *Neurosurgery*, 58(2):217–23; discussion 217–23, 2006. doi: 10.1227/01.neu.0000194639.37803.f8.

[15] M. Castro, C. Putman, A. Radaelli, A. Frangi, and J. Cebral. Hemodynamics and rupture of terminal cerebral aneurysms. *Acad Radiol*, 16(10):1201–7, 2009. doi: 10.1016/j.acra.2009.03.022.

[16] M. A. Castro, C. M. Putman, and J. R. Cebral. Patient-specific computational modeling of cerebral aneurysms with multiple avenues of flow from 3d rotational angiography images. *Acad Radiol*, 13(7):811–21, 2006. doi: 10.1016/j.acra.2006.03.011.

[17] M. A. Castro, C. M. Putman, and J. R. Cebral. Patient-specific computational fluid dynamics modeling of anterior communicating artery aneurysms: a study of the sensitivity of intra-aneurysmal flow patterns to flow conditions in the carotid arteries. *AJNR Am J Neuroradiol*, 27(10):2061–8, 2006.

[18] M. A. Castro, C. M. Putman, M. J. Sheridan, and J. R. Cebral. Hemodynamic patterns of anterior communicating artery aneurysms: a possible association with rupture. *AJNR Am J Neuroradiol*, 30(2):297–302, 2009. doi: 10.3174/ajnr.A1323.

[19] J. R. Cebral and H. Meng. Counterpoint: realizing the clinical utility of computational fluid dynamics–closing the gap. *AJNR Am J Neuroradiol*, 33(3):396–8, 2012. doi: 10.3174/ajnr.A2994.

[20] J. R. Cebral, M. A. Castro, J. E. Burgess, R. S. Pergolizzi, M. J. Sheridan, and C. M. Putman. Characterization of cerebral aneurysms for assessing risk of rupture by using patient-specific computational hemodynamics models. *AJNR Am J Neuroradiol*, 26(10):2550–9, 2005.

[21] J. R. Cebral, S. Hendrickson, and C. M. Putman. Hemodynamics in a lethal basilar artery aneurysm just before its rupture. *AJNR Am J Neuroradiol*, 30(1):95–8, 2009. doi: 10.3174/ajnr.A1312.

[22] J. R. Cebral, M. Sheridan, and C. M. Putman. Hemodynamics and bleb formation in intracranial aneurysms. *AJNR Am J Neuroradiol*, 31(2):304–10, 2010. doi: 10.3174/ajnr.A1819.

[23] J. R. Cebral, F. Mut, J. Weir, and C. Putman. Quantitative characterization of the hemodynamic environment in ruptured and unruptured brain aneurysms. *AJNR Am J Neuroradiol*, 32(1):145–51, 2011. doi: 10.3174/ajnr.A2419.

[24] J. R. Cebral, F. Mut, J. Weir, and C. M. Putman. Association of hemodynamic characteristics and cerebral aneurysm rupture. *AJNR Am J Neuroradiol*, 32(2):264–70, 2011. doi: 10.3174/ajnr.A2274.

[25] JR Cebral, R Löhner, S Appanaboyina, and CM Putman. Image-based computational hemodynamics methods and their application for the analysis of blood flow past endovascular devices. *Leondes CT. Biomechanical Systems: Techniques and Applications*, 1:29–85, 2007.

[26] Juan R Cebral and Rainald Loehner. Flow visualization on unstructured grids using geometrical cuts, vortex detection and shock surfaces. In *AIAA, Aerospace Sciences Meeting and Exhibit, 39 th, Reno, NV*, 2001.

[27] Juan R Cebral and R Lohner. Efficient simulation of blood flow past complex endovascular devices using an adaptive embedding technique. *Medical Imaging, IEEE Transactions on*, 24(4):468–476, 2005.

[28] Juan R Cebral and Marcelo Raschi. Suggested connections between risk factors of intracranial aneurysms: A review. *Annals of Biomedical Engineering*, 41(7):1366–1383, 2013. ISSN 0090-6964. URL `http://dx.doi.org/10.1007/s10439-012-0723-0`.

[29] Juan R Cebral, Marcelo A Castro, James E Burgess, and CM Putmari. Cerebral aneurysm hemodynamics modeling from 3d rotational angiography. In *Biomedical Imaging: Nano to Macro, 2004. IEEE International Symposium on*, pages 944–947. IEEE, 2004.

[30] A. Chien, S. Tateshima, J. Sayre, M. Castro, J. Cebral, and F. Vinuela. Patient-specific hemodynamic analysis of small internal carotid artery-ophthalmic artery aneurysms. *Surg Neurol*, 72(5):444–50; discussion 450, 2009. doi: 10.1016/j.surneu.2008.12.013.

[31] M. Chmayssani, J. G. Rebeiz, T. J. Rebeiz, H. H. Batjer, and B. R. Bendok. Relationship of growth to aneurysm rupture in asymptomatic aneurysms </= 7 mm: a systematic analysis of the literature. *Neurosurgery*, 68(5):1164–71; discussion 1171, 2011. doi: 10.1227/NEU.0b013e31820edbd3.

[32] I. S. Choi and C. David. Giant intracranial aneurysms: development, clinical presentation and treatment. *Eur J Radiol*, 46(3):178–94, 2003.

[33] G. Clarke, A. D. Mendelow, and P. Mitchell. Predicting the risk of rupture of intracranial aneurysms based on anatomical location. *Acta Neurochir (Wien)*, 147(3):259–63; discussion 263, 2005. doi: 10.1007/s00701-004-0473-3.

[34] Henry Darcy. *Les fontaines publiques de la ville de Dijon*. V. Dalmont, 1856.

[35] S De Putter, FN van de Vosse, FA Gerritsen, F Laffargue, and M Breeuwer. Computational mesh generation for vascular structures with deformable surfaces. *International Journal of Computer Assisted Radiology and Surgery*, 1(1):39–49, 2006.

[36] N. K. de Rooij, B. K. Velthuis, A. Algra, and G. J. Rinkel. Configuration of the circle of willis, direction of flow, and shape of the aneurysm as risk factors for rupture of intracranial aneurysms. *J Neurol*, 256(1):45–50, 2009. doi: 10.1007/s00415-009-0028-x.

[37] Sabri Ergun. Fluid flow through packed columns. *Chem. Eng. Prog.*, 48, 1952.

[38] Sh A Ershin and LG Khadieva. Hydrodynamic resistance and refracting effect of a fine-mesh screen. *Fluid Dynamics*, 23(2):249–254, 1988.

[39] Philipp Forchheimer. Wasserbewegung durch boden. *Z. Ver. Deutsch. Ing*, 45(1782):1788, 1901.

[40] M D Ford, H N Nikolov, J S Milner, S P Lownie, E M DeMont, W Kalata, F Loth, D W Holdsworth, and D A Steinman. Piv-measured versus cfd-predicted flow

dynamics in anatomically realistic cerebral aneurysm models. *J Biomech Engr*, 130 (2):021015–1/9, 2008.

[41] G. N. Foutrakis, H. Yonas, and R. J. Sclabassi. Saccular aneurysm formation in curved and bifurcating arteries. *AJNR Am J Neuroradiol*, 20(7):1309–17, 1999.

[42] J. Frosen, A. Piippo, A. Paetau, M. Kangasniemi, M. Niemela, J. Hernesniemi, and J. Jaaskelainen. Remodeling of saccular cerebral artery aneurysm wall is associated with rupture: histological analysis of 24 unruptured and 42 ruptured cases. *Stroke*, 35(10):2287–93, 2004. doi: 10.1161/01.STR.0000140636.30204.da. URL `http://www.ncbi.nlm.nih.gov/pubmed/15322297http://stroke.ahajournals.org/content/35/10/2287.full.pdf`.

[43] J. Frosen, R. Tulamo, A. Paetau, E. Laaksamo, M. Korja, A. Laakso, M. Niemela, and J. Hernesniemi. Saccular intracranial aneurysm: pathology and mechanisms. *Acta Neuropathol*, 123(6):773–86, 2012. doi: 10.1007/s00401-011-0939-3. URL `http://www.ncbi.nlm.nih.gov/pubmed/22249619http://www.springerlink.com/content/x56617x632142n47/fulltext.pdf`.

[44] C Groden, J Laudan, S Gatchell, and H Zeumer. Three-dimensional pulsatile flow simulation before and after endovascular coil embolization of a terminal cerebral aneurysm. *J Cereb Blood Flow Metab*, 21(12):1464–1471, 2001.

[45] J. Hamada, M. Morioka, S. Yano, T. Todaka, Y. Kai, and J. Kuratsu. Clinical features of aneurysms of the posterior cerebral artery: a 15-year experience with 21 cases. *Neurosurgery*, 56(4):662–70; discussion 662–70, 2005.

[46] Thomas Eilkær Hansen. *Flow in micro porous silicon carbide*. PhD thesis, M. Sc. thesis, Department of Micro-and Nanotechnology, Technical University of Denmark, 2007.

[47] N. Hashimoto, H. Handa, I. Nagata, and F. Hazama. Animal model of cerebral aneurysms: pathology and pathogenesis of induced cerebral aneurysms in rats. *Neurol Res*, 6(1-2):33–40, 1984.

[48] T. Hassan, E. V. Timofeev, T. Saito, H. Shimizu, M. Ezura, Y. Matsumoto, K. Takayama, T. Tominaga, and A. Takahashi. A proposed parent vessel geometry-based categorization of saccular intracranial aneurysms: computational flow dynamics analysis of the risk factors for lesion rupture. *J Neurosurg*, 103(4):662–80, 2005.

[49] T. Hassan, A. A. Hassan, and Y. M. Ahmed. Influence of parent vessel dominancy on fluid dynamics of anterior communicating artery aneurysms. *Acta Neurochir (Wien)*, 153(2):305–10, 2011. doi: 10.1007/s00701-010-0824-1.

[50] M Hennerici, W Rautenberg, G Sitzer, and A Schwartz. Transcranial doppler ultrasound for the assessment of intracranial arterial flow velocity-part 1. examination technique and normal values. *Surgical neurology*, 27(5):439–448, 1987.

[51] T. Higa, H. Ujiie, K. Kato, H. Kamiyama, and T. Hori. Basilar artery trunk saccular aneurysms: morphological characteristics and management. *Neurosurg Rev*, 32(2): 181–91; discussion 191, 2009. doi: 10.1007/s10143-008-0163-3.

[52] I. E. Idelchik. *Handbook of Hydraulic Resistance*. Crc Pr I Llc, 1994. ISBN 0849399084.

[53] S. G. Imbesi and C. W. Kerber. Analysis of slipstream flow in two ruptured intracranial cerebral aneurysms. *AJNR Am J Neuroradiol*, 20(9):1703–5, 1999.

[54] J. G. Isaksen, Y. Bazilevs, T. Kvamsdal, Y. Zhang, J. H. Kaspersen, K. Waterloo, B. Romner, and T. Ingebrigtsen. Determination of wall tension in cerebral artery aneurysms by numerical simulation. *Stroke*, 39(12):3172–8, 2008. doi: 10.1161/strokeaha.107.503698.

[55] L. D. Jou and M. E. Mawad. Timing and size of flow impingement in a giant intracranial aneurysm at the internal carotid artery. *Med Biol Eng Comput*, 49(8): 891–9, 2011. doi: 10.1007/s11517-010-0727-6.

[56] L. D. Jou, C. M. Quick, W. L. Young, M. T. Lawton, R. Higashida, A. Martin, and D. Saloner. Computational approach to quantifying hemodynamic forces in giant cerebral aneurysms. *Am J Neuroradiol*, 24(9):1804–10, 2003.

[57] L. D. Jou, G. Wong, B. Dispensa, M. T. Lawton, R. T. Higashida, W. L. Young, and D. Saloner. Correlation between lumenal geometry changes and hemodynamics in fusiform intracranial aneurysms. *AJNR Am J Neuroradiol*, 26(9):2357–63, 2005.

[58] L. D. Jou, D. H. Lee, H. Morsi, and M. E. Mawad. Wall shear stress on ruptured and unruptured intracranial aneurysms at the internal carotid artery. *AJNR Am J Neuroradiol*, 29(9):1761–7, 2008. doi: 10.3174/ajnr.A1180.

[59] S. Juvela, K. Poussa, and M. Porras. Factors affecting formation and growth of intracranial aneurysms: a long-term follow-up study. *Stroke*, 32(2):485–91, 2001.

[60] L. M. Kadasi, W. C. Dent, and A. M. Malek. Cerebral aneurysm wall thickness analysis using intraoperative microscopy: effect of size and gender on thin translucent regions. *J Neurointerv Surg*, 2012. doi: 10.1136/neurintsurg-2012-010285.

[61] D. F. Kallmes. Point: Cfd–computational fluid dynamics or confounding factor dissemination. *AJNR Am J Neuroradiol*, 33(3):395–6, 2012. doi: 10.3174/ajnr.A2993.

[62] David F Kallmes, Yong Hong Ding, Daying Dai, Ramanathan Kadirvel, Debra A Lewis, and Harry J Cloft. A new endoluminal, flow-disrupting device for treatment of saccular aneurysms. *Stroke*, 38(8):2346–2352, 2007.

[63] K. Kataoka, M. Taneda, T. Asai, A. Kinoshita, M. Ito, and R. Kuroda. Structural fragility and inflammatory response of ruptured cerebral aneurysms. a comparative study between ruptured and unruptured cerebral aneurysms. *Stroke*, 30(7):1396–401, 1999. URL `http://www.ncbi.nlm.nih.gov/pubmed/10390313http://stroke.ahajournals.org/content/30/7/1396.full.pdf`.

[64] Minsuok Kim, Dale B Taulbee, Markus Tremmel, and Hui Meng. Comparison of two stents in modifying cerebral aneurysm hemodynamics. *Annals of biomedical engineering*, 36(5):726–741, 2008.

[65] M. Korja, K. Silventoinen, P. McCarron, S. Zdravkovic, A. Skytthe, A. Haapanen, U. de Faire, N. L. Pedersen, K. Christensen, M. Koskenvuo, and J. Kaprio. Genetic epidemiology of spontaneous subarachnoid hemorrhage: Nordic twin study. *Stroke*, 41(11):2458–62, 2010. doi: 10.1161/STROKEAHA.110.586420. URL `http://www.ncbi.nlm.nih.gov/pubmed/20847318`.

[66] S. K. Kyriacou and J. D. Humphrey. Influence of size, shape and properties on the mechanics of axisymmetric saccular aneurysms. *J Biomech*, 29(8):1015–22, 1996.

[67] A. Lauric, E. L. Miller, M. I. Baharoglu, and A. M. Malek. Rupture status discrimination in intracranial aneurysms using the centroid-radii model. *IEEE Trans Biomed Eng*, 58(10):2895–903, 2011. doi: 10.1109/tbme.2011.2162410.

[68] Hongyu Li and I-Fan Shen. Similarity measure for vector field learning. In *Advances in Neural Networks-ISNN 2006*, pages 436–441. Springer, 2006.

[69] H. M. Lindekleiv, K. Valen-Sendstad, M. K. Morgan, K. A. Mardal, K. Faulder, J. H. Magnus, K. Waterloo, B. Romner, and T. Ingebrigtsen. Sex differences in intracranial arterial bifurcations. *Gend Med*, 7(2):149–55, 2010. doi: 10.1016/j.genm.2010.03.003.

[70] JF Liu, WT Wu, WC Chiu, and WH Hsieh. Measurement and correlation of friction characteristic of flow through foam matrixes. *Experimental thermal and fluid science*, 30(4):329–336, 2006.

[71] Rainald Löhner. Applied cfd techniques. *J. Wiley & Sons*, 2001.

[72] A. Mantha, C. Karmonik, G. Benndorf, C. Strother, and R. Metcalfe. Hemodynamics in a cerebral artery before and after the formation of an aneurysm. *AJNR Am J Neuroradiol*, 27(5):1113–8, 2006.

[73] H. Meng, Y. Feng, S. H. Woodward, B. R. Bendok, R. A. Hanel, L. R. Guterman, and L. N. Hopkins. Mathematical model of the rupture mechanism of intracranial saccular aneurysms through daughter aneurysm formation and growth. *Neurol Res*, 27(5):459–65, 2005. doi: 10.1179/016164105x25171.

[74] E. Metaxa, M. Tremmel, S. K. Natarajan, J. Xiang, R. A. Paluch, M. Mandelbaum, A. H. Siddiqui, J. Kolega, J. Mocco, and H. Meng. Characterization of critical hemodynamics contributing to aneurysmal remodeling at the basilar terminus in a rabbit model. *Stroke*, 41(8):1774–82, 2010. doi: 10.1161/strokeaha.110.585992.

[75] R. D. Millan, L. Dempere-Marco, J. M. Pozo, J. R. Cebral, and A. F. Frangi. Morphological characterization of intracranial aneurysms using 3-d moment invariants. *IEEE Trans Med Imaging*, 26(9):1270–82, 2007. doi: 10.1109/tmi.2007.901008.

[76] Taku Morino, Tetsuya Tanoue, Satoshi Tateshima, Fernando Vinuela, and Kazuo Tanishita. Intra-aneurysmal blood flow based on patient-specific ct angiogram. *Experiments in fluids*, 49(2):485–496, 2010.

[77] F Mut and JR Cebral. Effects of flow-diverting device oversizing on hemodynamics alteration in cerebral aneurysms. *American Journal of Neuroradiology*, 33(10):2010–2016, 2012.

[78] F Mut, S Appanaboyina, and JR Cebral. Simulation of stent deployment in patient-specific cerebral aneurysm models for their hemodynamics analysis. In *Proceedings of the Summer Bioengineering Conference of the American Society of Mechanical Engineers Marco Island, Florida*, 2008.

[79] F Mut, R Aubry, R Löhner, and JR Cebral. Fast numerical solutions in patient-specific simulations of arterial models. *Comm Num Meth Eng*, 200910, 2009.

[80] S. H. Nystrom. On factors related to growth and rupture of intracranial aneurysms. *Acta Neuropathol*, 16(1):64–72, 1970.

[81] Y. S. Oh, Y. M. Shon, B. S. Kim, and A. H. Cho. Long-term follow-up of incidental intracranial aneurysms in patients with acute ischemic stroke. *J Stroke Cerebrovasc Dis*, 2011. doi: 10.1016/j.jstrokecerebrovasdis.2011.09.011.

[82] T. Ohshima, S. Miyachi, K. Hattori, I. Takahashi, K. Ishii, T. Izumi, and J. Yoshida. Risk of aneurysmal rupture: the importance of neck orifice positioning-assessment using computational flow simulation. *Neurosurgery*, 62(4):767–73; discussion 773–5, 2008. doi: 10.1227/01.neu.0000318160.59848.46.

[83] D. H. Park, S. H. Kang, J. B. Lee, D. J. Lim, T. H. Kwon, Y. G. Chung, and H. K. Lee. Angiographic features, surgical management and outcomes of proximal middle cerebral artery aneurysms. *Clin Neurol Neurosurg*, 110(6):544–51, 2008. doi: 10.1016/j.clineuro.2008.02.014.

[84] Ronald Peikert and Martin Roth. The "parallel vectors" operator: a vector field visualization primitive. In *Proceedings of the conference on Visualization'99: celebrating ten years*, pages 263–270. IEEE Computer Society Press, 1999.

[85] J. P. Peluso, W. J. van Rooij, M. Sluzewski, G. N. Beute, and C. B. Majoie. Posterior inferior cerebellar artery aneurysms: incidence, clinical presentation, and outcome of endovascular treatment. *AJNR Am J Neuroradiol*, 29(1):86–90, 2008. doi: 10.3174/ajnr.A0758.

[86] D. L. Penn, R. J. Komotar, and E. Sander Connolly. Hemodynamic mechanisms underlying cerebral aneurysm pathogenesis. *J Clin Neurosci*, 18(11):1435–8, 2011. doi: 10.1016/j.jocn.2011.05.001.

[87] RA Pinker and MV Herbert. Pressure loss associated with compressible flow through square-mesh wire gauzes. *Journal of Mechanical Engineering Science*, 9(1): 11–23, 1967.

[88] C. J. Prestigiacomo, W. He, J. Catrambone, S. Chung, L. Kasper, L. Pasupuleti, and N. Mittal. Predicting aneurysm rupture probabilities through the application of a computed tomography angiography-derived binary logistic regression model. *J Neurosurg*, 110(1):1–6, 2009. doi: 10.3171/2008.5.17558.

[89] W. Qi, S. Wang, Y. L. Zhao, H. B. Yang, and J. Z. Zhao. Clinical characteristics and surgical treatment of patients with giant intracranial aneurysms. *Chin Med J (Engl)*, 121(12):1085–8, 2008.

[90] Y. Qian, H. Takao, M. Umezu, and Y. Murayama. Risk analysis of unruptured aneurysms using computational fluid dynamics technology: preliminary results. *AJNR Am J Neuroradiol*, 32(10):1948–55, 2011. doi: 10.3174/ajnr.A2655.

[91] A.G. Radaelli, L. Augsburger, J.R. Cebral, M. Ohta, D.A. Rüfenacht, R. Balossino, G. Benndorf, D.R. Hose, A. Marzo, R. Metcalfe, P. Mortier, F. Mut, P. G. Reymond, L. Socci, B. Verhegghe, and A.F. Frangi. Reproducibility of haemodynamical simulations in a subject-specific stented aneurysm model-a report on the virtual intracranial stenting challenge 2007. *Journal of Biomechanics*, 41(10):2069–2081, 2008.

[92] Markus Raffel, Christian E Willert, Steven T Wereley, and Jürgen Kompenhans. *Particle image velocimetry: a practical guide*. Springer, 2007.

[93] Marcelo Raschi, Fernando Mut, Greg Byrne, Christopher M Putman, Satoshi Tateshima, Fernando Viñuela, Tetsuya Tanoue, Kazuo Tanishita, and Juan R Cebral. Cfd and piv analysis of hemodynamics in a growing intracranial aneurysm. *International journal for numerical methods in biomedical engineering*, 28(2):214–228, 2012.

[94] G. J. Rinkel, M. Djibuti, A. Algra, and J. van Gijn. Prevalence and risk of rupture of intracranial aneurysms: a systematic review. *Stroke*, 29(1):251–6, 1998. URL `http://www.ncbi.nlm.nih.gov/pubmed/9445359http://stroke.ahajournals.org/content/29/1/251.full.pdf`.

[95] A. M. Robertson and P. N. Watton. Computational fluid dynamics in aneurysm research: critical reflections, future directions. *AJNR Am J Neuroradiol*, 33(6):992–5, 2012. doi: 10.3174/ajnr.A3192.

[96] Martin Roth and Ronald Peikert. A higher-order method for finding vortex core lines. In *Visualization'98. Proceedings*, pages 143–150. IEEE, 1998.

[97] C. W. Ryu, O. K. Kwon, J. S. Koh, and E. J. Kim. Analysis of aneurysm rupture in relation to the geometric indices: aspect ratio, volume, and volume-to-neck ratio. *Neuroradiology*, 53(11):883–9, 2011. doi: 10.1007/s00234-010-0804-4.

[98] K. Sato and Y. Yoshimoto. Risk profile of intracranial aneurysms: rupture rate is not constant after formation. *Stroke*, 42(12):3376–81, 2011. doi: 10.1161/strokeaha.111.625871.

[99] J Sawicki, W Szpakowski, K Weinerowska, E Woloszyn, and P Zima. Laboratory of fluid mechanics and hydraulics. *Gdansk University of Technology, Gdansk, Poland*, 2004.

[100] P. Seshaiyer and J. D. Humphrey. On the potentially protective role of contact constraints on saccular aneurysms. *J Biomech*, 34(5):607–12, 2001.

[101] D. M. Sforza, C. M. Putman, and J. R. Cebral. Hemodynamics of cerebral aneurysms. *Annu Rev Fluid Mech*, 41:91–107, 2009. doi: 10.1146/annurev.fluid.40.111406.102126. URL `http://www.ncbi.nlm.nih.gov/pubmed/19784385`.

[102] D. M. Sforza, C. M. Putman, E. Scrivano, P. Lylyk, and J. R. Cebral. Blood-flow characteristics in a terminal basilar tip aneurysm prior to its fatal rupture. *AJNR Am J Neuroradiol*, 31(6):1127–31, 2010. doi: 10.3174/ajnr.A2021.

[103] D. M. Sforza, C. Putman, and J. Cebral. Computational fluid dynamics (cfd) in brain aneurysms. *Int J Numer Meth Biomed Engng*, 28(6-7):801–808, 2012.

[104] D. M. Sforza, C. Putman, S. Tateshima, F. Vinuela, and J. Cebral. Hemodynamic characteristics of growing and stable aneurysms. In *Summer Bioengineering Conference (SBC2012)*, volume SBC2012-80178 of *Series Hemodynamic characteristics of growing and stable aneurysms*, Fajardo, Puerto Rico, 2012.

[105] D. M. Sforza, C. M. Putman, S. Tateshima, F. Vinuela, and J. R. Cebral. Effects of perianeurysmal environment during the growth of cerebral aneurysms: a case study. *AJNR Am J Neuroradiol*, 33(6):1115–20, 2012. doi: 10.3174/ajnr.A2908.

[106] Y. Shimogonya, T. Ishikawa, Y. Imai, N. Matsuki, and T. Yamaguchi. Can temporal fluctuation in spatial wall shear stress gradient initiate a cerebral aneurysm? a proposed novel hemodynamic index, the gradient oscillatory number (gon). *J Biomech*, 42(4):550–4, 2009. doi: 10.1016/j.jbiomech.2008.10.006.

[107] M. Shojima, M. Oshima, K. Takagi, R. Torii, M. Hayakawa, K. Katada, A. Morita, and T. Kirino. Magnitude and role of wall shear stress on cerebral aneurysm: computational fluid dynamic study of 20 middle cerebral artery aneurysms. *Stroke*, 35 (11):2500–5, 2004. doi: 10.1161/01.STR.0000144648.89172.0f.

[108] M. Shojima, M. Oshima, K. Takagi, R. Torii, M. Hayakawa, K. Katada, A. Morita, and T. Kirino. Magnitude and role of wall shear stress on cerebral aneurysm: computational fluid dynamic study of 20 middle cerebral artery aneurysms. *Stroke*, 35 (11):2500–2505, 2004.

[109] M. Shojima, S. Nemoto, A. Morita, M. Oshima, E. Watanabe, and N. Saito. Role of shear stress in the blister formation of cerebral aneurysms. *Neurosurgery*, 67(5): 1268–74; discussion 1274–5, 2010. doi: 10.1227/NEU.0b013e3181f2f442.

[110] Wojciech Sobieski and Anna Trykozko. Darcy and forchheimer laws in the experimental and simulation studies of flow through porous media. *Transport in Porous Media (submitted)*.

[111] D. Songsaeng, S. Geibprasert, R. Willinsky, M. Tymianski, K. G. TerBrugge, and T. Krings. Impact of anatomical variations of the circle of willis on the incidence of aneurysms and their recurrence rate following endovascular treatment. *Clin Radiol*, 65(11):895–901, 2010. doi: 10.1016/j.crad.2010.06.010.

[112] W. E. Stehbens. Etiology of intracranial berry aneurysms. *J Neurosurg*, 70(6):823–31, 1989. doi: 10.3171/jns.1989.70.6.0823.

[113] D. A. Steinman, J. S. Milner, C. J. Norley, S. P. Lownie, and D. W. Holdsworth. Image-based computational simulation of flow dynamics in a giant intracranial aneurysm. *Am J Neuroradiol*, 24(4):559–66, 2003. Comment on: AJNR Am J Neuroradiol. 2003

Apr;24(4):553-4; PMID: 12695178.

[114] F. Stern, R.V. Wilson, H.W. Coleman, and E.G. Paterson. Comprehensive approach to verification and validation of cfd simulations-part 1: Methodology and procedures. *Transactions-american society of mechanical engineers journal of fluids engineering*, 123(4):793–802, 2001.

[115] CM Strother and J Jiang. Intracranial aneurysms, cancer, x-rays, and computational fluid dynamics. *American Journal of Neuroradiology*, 33(6):991–992, 2012.

[116] G R Stuhne and D A Steinman. Finite element modeling of the hemodynamics of stented aneurysms. *Journal of Biomechanical Engineering*, 126:382–7, 2004.

[117] K. Sugiu, B. Jean, D. San Millan Ruiz, J. B. Martin, J. Delavelle, and D. A. Rufenacht. Influence of the perianeurysmal environment on rupture of cerebral aneurysms. preliminary observation. *Interv Neuroradiol*, 6 Suppl 1:65–70, 2000.

[118] S. I. Sugiyama, H. Meng, K. Funamoto, T. Inoue, M. Fujimura, T. Nakayama, S. Omodaka, H. Shimizu, A. Takahashi, and T. Tominaga. Hemodynamic analysis of growing intracranial aneurysms arising from a posterior inferior cerebellar artery. *World Neurosurg*, 2011. doi: 10.1016/j.wneu.2011.09.023.

[119] David Sujudi and Robert Haimes. Identification of swirling flow in 3d vector fields. Technical report, Citeseer, 1995.

[120] H. Takao, Y. Murayama, S. Otsuka, Y. Qian, A. Mohamed, S. Masuda, M. Yamamoto, and T. Abe. Hemodynamic differences between unruptured and ruptured intracranial aneurysms during observation. *Stroke*, 43(5):1436–9, 2012. doi: 10.1161/strokeaha.111.640995.

[121] S. Tateshima, Y. Murayama, J. P. Villablanca, T. Morino, K. Nomura, K. Tanishita, and F. Vinuela. In vitro measurement of fluid-induced wall shear stress in unruptured cerebral aneurysms harboring blebs. *Stroke*, 34(1):187–92, 2003.

[122] S Tateshima, K Tanishita, H Omura, JP Villablanca, and F Vinuela. Intra-aneurysmal hemodynamics during the growth of an unruptured aneurysm: in vitro study using longitudinal ct angiogram database. *American journal of neuroradiology*, 28(4):622–627, 2007.

[123] Satoshi Tateshima, Yuichi Murayama, J Pablo Villablanca, Taku Morino, Hikoichiro Takahashi, Takatsugu Yamauchi, Kazuo Tanishita, and Fernando Viñuela. Intraaneurysmal flow dynamics study featuring an acrylic aneurysm model manufactured using a computerized tomography angiogram as a mold. *Journal of neuro-*

surgery, 95(6):1020–1027, 2001.

[124] C A Taylor and M T Draney. Computational techniques in therapeutic decision-making. *Computer Assisted Surgery*, 4:231–247, 1999.

[125] Bernd Thomas and Deborah Pittman. Update on the evaluation of different correlations for the flow friction factor and heat transfer of stirling engine regenerators. In *Energy Conversion Engineering Conference and Exhibit, 2000.(IECEC) 35th Intersociety*, volume 1, pages 76–84. IEEE, 2000.

[126] H. Ujiie, D. W. Liepsch, M. Goetz, R. Yamaguchi, H. Yonetani, and K. Takakura. Hemodynamic study of the anterior communicating artery. *Stroke*, 27(11):2086–93; discussion 2094, 1996.

[127] K. Valen-Sendstad, K. A. Mardal, M. Mortensen, B. A. Reif, and H. P. Langtangen. Direct numerical simulation of transitional flow in a patient-specific intracranial aneurysm. *J Biomech*, 44(16):2826–32, 2011. doi: 10.1016/j.jbiomech.2011.08.015.

[128] A. Valencia, H. Morales, R. Rivera, E. Bravo, and M. Galvez. Blood flow dynamics in patient-specific cerebral aneurysm models: the relationship between wall shear stress and aneurysm area index. *Med Eng Phys*, 30(3):329–40, 2008. doi: 10.1016/j.medengphy.2007.04.011.

[129] A. Valencia, J. Munizaga, R. Rivera, and E. Bravo. Numerical investigation of the hemodynamics in anatomically realistic lateral cerebral aneurysms. *Conf Proc IEEE Eng Med Biol Soc*, 2010:2616–21, 2010. doi: 10.1109/iembs.2010.5626613.

[130] N. M. van der Kolk, A. Algra, and G. J. Rinkel. Risk of aneurysm rupture at intracranial arterial bifurcations. *Cerebrovasc Dis*, 30(1):29–35, 2010. doi: 10.1159/000313441.

[131] R Van Loon, PD Anderson, and FN Van de Vosse. A fluid–structure interaction method with solid-rigid contact for heart valve dynamics. *Journal of computational physics*, 217(2):806–823, 2006.

[132] C. Vega, J. V. Kwoon, and S. D. Lavine. Intracranial aneurysms: current evidence and clinical practice. *Am Fam Physician*, 66(4):601–8, 2002.

[133] Prem Venugopal, Holger Schmitt, Gary R Duckwiler, and Daniel J Valentino. Effects of segmentation on patient-specific numerical simulation of cerebral aneurysm hemodynamics. In *Medical Imaging*, pages 61430F–61430F. International Society for Optics and Photonics, 2006.

[134] Ray Scott Wakeland and Robert M Keolian. Measurements of resistance of individual square-mesh screens to oscillating flow at low and intermediate reynolds numbers. *Journal of fluids engineering*, 125(5):851–862, 2003.

[135] B. Weir and R L MacDonald. *Intracranial aneurysms and subarachnoid hemorrhage: an overview*. Neurosurgery. McGraw Hill, New York, NY, 1996.

[136] B. Weir, L. Disney, and T. Karrison. Sizes of ruptured and unruptured aneurysms in relation to their sites and the ages of patients. *J Neurosurg*, 96(1):64–70, 2002. doi: 10.3171/jns.2002.96.1.0064.

[137] D. O. Wiebers, J. C. Torner, and I. Meissner. Impact of unruptured intracranial aneurysms on public health in the united states. *Stroke*, 23(10):1416–9, 1992.

[138] D. O. Wiebers, J. P. Whisnant, 3rd Huston, J., I. Meissner, Jr. Brown, R. D., D. G. Piepgras, G. S. Forbes, K. Thielen, D. Nichols, W. M. O'Fallon, J. Peacock, L. Jaeger, N. F. Kassell, G. L. Kongable-Beckman, and J. C. Torner. Unruptured intracranial aneurysms: natural history, clinical outcome, and risks of surgical and endovascular treatment. *Lancet*, 362(9378):103–10, 2003.

[139] G. K. Wong and W. S. Poon. Current status of computational fluid dynamics for cerebral aneurysms: the clinician's perspective. *J Clin Neurosci*, 18(10):1285–8, 2011. doi: 10.1016/j.jocn.2011.02.014.

[140] WT Wu, JF Liu, WJ Li, and WH Hsieh. Measurement and correlation of hydraulic resistance of flow through woven metal screens. *International journal of heat and mass transfer*, 48(14):3008–3017, 2005.

[141] J. Xiang, S. K. Natarajan, M. Tremmel, D. Ma, J. Mocco, L. N. Hopkins, A. H. Siddiqui, E. I. Levy, and H. Meng. Hemodynamic-morphologic discriminants for intracranial aneurysm rupture. *Stroke*, 42(1):144–52, 2011. doi: 10.1161/strokeaha.110.592923.

[142] Y. Xu, Y. Tian, H. J. Wei, J. Chen, J. F. Dong, A. Zacharek, and J. N. Zhang. Erythropoietin increases circulating endothelial progenitor cells and reduces the formation and progression of cerebral aneurysm in rats. *Neuroscience*, 181:292–9, 2011. doi: 10.1016/j.neuroscience.2011.02.051.

[143] R. Yamaguchi, H. Ujiie, S. Haida, N. Nakazawa, and T. Hori. Velocity profile and wall shear stress of saccular aneurysms at the anterior communicating artery. *Heart Vessels*, 23(1):60–6, 2008. doi: 10.1007/s00380-007-0996-7.

CURRICULUM VITAE

Marcelo A. Raschi received his Bachelor of Science in Nuclear Engineering from the Instituto Balseiro in 2000. After working four years in the industry, he moved on to the academy as Research Assistant in 2005. He went on to receive his Master of Science in Biomedical Engineering at Universidad Favaloro in 2008, and he finished his Doctor of Philosophy in Computational Sciences and Informatics at George Mason University in 2013.